Structure-property Correlation of Front Side Metallization Contacts for High-efficiency, Single-crystalline Si Solar Cells

Dissertation

der Mathematisch-Naturwissenschaftlichen Fakultät

der Eberhard Karls Universität Tübingen

zur Erlangung des Grades eines

Doktors der Naturwissenschaften

(Dr. rer. nat.)

vorgelegt von

Praveen Kumar

aus Baghpat, Indien

Tübingen

2017

Gedruckt mit Genehmigung der Mathematisch-Naturwissenschaftlichen Fakultät der Eberhard Karls Universität Tübingen.

Tag der mündlichen Qualifikation:	06.03.2018
Dekan:	Prof. Dr. Wolfgang Rosenstiel
1. Berichterstatter:	Prof. Dr. Oliver Eibl
2. Berichterstatter:	Prof. Dr. Frank Schreiber

"The power of God is with you at all times; through the activities of mind, senses, breathing and emotions; and is constantly doing all the work using you as a mere instrument"

<div align="right">The Bhagavad Gita!!!</div>

Summary

Mono-crystalline Si solar cell based on screen-printed front side metallization is the most widely used technology for industrial solar cells. It is well known that the efficiency of Si solar cells is limited by electrical losses associated with the screen-printed front side paste as well as the high-temperature firing process. The series resistance of a cell is one of the essential quantities for the electrical properties and is in the range of $< 1 \ \Omega \ cm^2$ for high-efficiency cells. A second important quantity is the lifetime of the relevant charge carriers which is not directly a part of this investigation, but passivated contacts have emerged as a key research topic. Detailed microstructural and chemical analysis allow the understanding of losses related to the series resistance of the front side contacts and to overcome the limitations and increase the cell efficiency.

Front side screen-printed contacts yields a complex silicon metallization interface which consists of a Si emitter embedded with Ag nanocrystals, a glass layer typically <1 μm thick that contains nano-Ag colloids and on top of it a bulk metallization finger.

In this thesis, results are presented of advanced solar cell characterization applied to high-efficiency p- and n- type Si solar cells. Planar as well as textured p-type cells were processed at Fraunhofer ISE within the *MikroSol* project. High-quality n- PERT (Passivated emitter and rear totally diffused) type cells yielding efficiencies up to 20 % were processed at ISC Konstanz.

A completely new methodology has been set up to investigate the front side metallization of solar cells. Key features are:

- Investigate both high-efficiency p- and n-type cells. Carefully select samples for microstructural analysis according to their electrical properties.
- Apply precision plan view grinding for analyzing the metallization.
- Apply cross-sectional preparation techniques together with plan-view prepared samples to gain maximum quantitative insight into the microstructure at the Si metallization interface.
- For understanding the chemical composition of the metallization we apply quantitative chemical analysis by EDX spectroscopy together with standard imaging methods both in the SEM and TEM.
- Use temperature dependent series resistance measurements and correlate them with microstructural analysis.
- Correlative Nano-SIMS and SEM-EDX analysis for analyzing the effects of front side metallization contacts and firing conditions on the dopant distribution near the p/n junction.

High-efficiency p- (18.0 %) and n-type (20 %) textured cells yielded similar microstructure (a glass matrix embedded with a high density of Ag colloids covering the emitter and the Ag bulk), similar temperature dependent series resistance, and contact resistance of $<5 \ m\Omega \ cm^2$. These unique measurement methods yielded key results, not previously known in the literature:

- Different to p-type cells pyramidal Ag nanocrystals were not observed at the B doped emitter surface for n-type cells.
- Pyramidal Ag nanocrystals are not necessary for obtaining a low contact resistance.
- High-efficiency p- and n-type cells yield similar microstructure of the glass layer and electrical properties of the front side metallization indicating that a common transport mechanism might

exist.

- A high density of Ag colloids typically less than 200 nm in size was observed in the glass layer of high efficiency p- and n-type cells yielding a low specific contact resistance. Cells with a low density of Ag colloids revealed a high contact resistance.

- The quantitative chemical composition of the glass layer of p- and n-type cells was investigated by Energy Dispersive X-ray (EDX) microanalysis in SEM and TEM. It consists of $(SiO_X)Pb$, as main constituent and Zn, Ti, Al, Ag, P and B as minor constituents with mole fractions above the detection limit of EDX. The glass layer is, therefore, considered a dirty semiconductor rather than a perfect insulator.

- The presence of a semiconducting rather than an insulating glass layer containing metallic Ag colloids and impurities indicates that the glass layer is a part of the relevant current path between the emitter and Ag bulk metallization. This is in contrast to existing models in which the glass layer is considered to be an insulator which would not yield a current for its bulk. By considering the microstructural analysis of the glass layer and the presence of Ag colloids and other metallic precipitates, a percolation model has been introduced in which metallic Ag colloids generate current filaments across the glass layer. This model is best suited to describe the charge transport in a dirty semiconductor containing metallic precipitates.

A new methodology has been implemented for this thesis and the results have contributed substantial new knowledge for the metallization of Si solar cells. This will be outlined in more detail in the following chapters. The introduced percolation model for the glass layer is based on the microstructural analysis and yields a quantitative (contact) resistance depending on the volume fraction of Ag colloids. The development of the percolation model for the glass layer is not central part of this thesis but will be described elsewhere. Rather the methodology implemented here for solar cells was successfully applied by the author to other materials systems, thermoelectric materials and materials used as IR detectors. Results have been published but were not included in this thesis.

Zusammenfassung

Die Methode der siebgedruckte Vorderseitenmetallisierung ist die am weitesten verbreitete Technologie für Monokristalline Si-Solarzellen. Es ist bekannt, dass die Effizienz von Si-Solarzellen durch elektrische Verluste begrenzt ist, die mit der siebgedruckte Vorderseitenmetallierung verknüpft sind. Der Serienwiderstand einer Zelle ist eine der wichtigsten Größe der elektrischen Eigenschaften und liegt für hocheffiziente Zellen im Bereich von $< 1 \, \Omega \, cm^2$. Eine zweite wichtige Größe ist die Lebensdauer der relevanten Ladungsträger, die nicht direkt Teil dieser Untersuchung ist, Passivierte Kontakte haben sich zu einem zentralen Forschungsthema entwickelt. Detaillierte mikrostrukturelle und chemische Analysen erlauben es, Verluste im Zusammenhang mit dem Serienwiderstand der Vorderseitenkontakte zu verstehen um die Grenzen zu überwinden und die Effizienz der Zelle zu erhöhen. Frontseitige Siebdruckkontakte ergeben eine komplexe Silizium-Metallisierungs Grenz-fläche, die aus einem mit Ag-Nanokristallen durchsetzten Si-Emitter besteht, einer typischerweise $<1 \, \mu$m dicken Glasschicht, die Nano-Ag-Kolloide enthält und darüber den Metallisierungsfinger.

In dieser Arbeit werden die Ergebnisse einer weiterentwickelten Solarzellencharakterisieru-ng für hocheffiziente p- und n-Typ Si-Solarzellen vorgestellt. Sowohl planare als auch strukturierte p-Zellen wurden am Fraunhofer ISE im Rahmen des Projekts *MikroSol* herge-stellt. Hochwertige n-PERT-Zellen (passivierter Emitter mit diffundierten Kontakten an der Rückseite) mit ein-em Wirkungsgrad von bis zu 20% wurden am ISC Konstanz hergestellt. Eine völlig neue Methodik wurde entwickelt um die Vorderseitenmetallisierung von Solarzellen zu untersuchen. Hauptmerkmale sind:

- Untersuchung sowohl hocheffizienter n- als auch p-Typ-Zellen. Sorgfältige Probenauswahl für die mikrostrukturelle Analyse nach ihren elektrischen Eigenschaften.
- Präzises Planschleifen der Proben für die Analyse der Metallisierung.
- Präparation von Querschnitts- als auch Draufsichtproben erlauben einen optimalen quantitativen Einblick in die Mikrostruktur an der Si/Metallisierungs Grenzfläche.
- Um die chemische Zusammensetzung der Metallisierung zu verstehen, muss eine quantitative chemische Analyse mittels EDX-Spektroskopie zusammen mit Standard-Bildgebungsverfahren sowohl im SEM als auch im TEM durchgeführt werden.
- Temperaturabhängige Messungen des Serienwiderstands werden mit der Mikrostrukturanalyse korreliert.
- Korrelative Nano-SIMS- und SEM-EDX-Analyse zur Analyse des Effekts des Front-Screen-Drucks auf die Dotierstoffverteilung in der Nähe des p / n-Übergangs.

Hocheffiziente p- (18,0%) und n-Typ (20%) texturierte Zellen zeigen eine ähnliche Mikro-struktur (eine Glasmatrix eingebettet mit einer hohen Dichte von Ag-Kolloiden, die den Emitter und die Ag-Finger bedecken), ähnlichen temperaturabhängigen Serienwiderstand und Kontaktwiderstand von $<5 \, m\Omega \, cm^2$. Diese einzigartigen Messmethoden lieferten wichtige Ergebnisse, die bisher in der Literatur nicht bekannt waren:

- Anders als bei p-Typ-Zellen wurden bei n-Typ-Zellen keine pyramidenförmige Ag-Nanokristalle an der B-dotierten Emitteroberfläche beobachtet.
- Pyramidenförmige Ag-Nanokristalle sind nicht notwendig, um einen niedrigen Kontaktwiderstand zu erzielen.

- Hocheffiziente p- und n-Typ-Zellen ergeben eine ähnliche Mikrostruktur der Glasschicht und elektrische Eigenschaften der Vorderseitenmetallisierung, was darauf hindeutet, dass ein ähnlicher Strompfad durch die Zellen bestehen sollte.

- Eine hohe Dichte von Ag-Kolloiden mit einer Größe von typischerweise weniger als 200 nm wurde in der Glasschicht von hocheffizienten p- sowohl als auch n-Typ-Zellen beobachtet, was einen geringen spezifischen Kontaktwiderstand ergab. Zellen mit einer geringen Dichte von Ag-Kolloiden zeigten einen hohen Kontaktwiderstand.

- Die quantitative chemische Zusammensetzung der Glasschicht von p- und n-Typ-Zellen wurde durch Energiedispersive Röntgen (EDX) -Mikroanalyse im SEM und TEM untersucht. Die Schicht besteht in der Hauptsache aus Pb haltigem SiO_X, d.h. einem bleihaltigen Glas und enthält Zn, Ti, Al, Ag, P und B als Beimengungen mit Stoffanteilen anteilen oberhalb der Nachweisgrenze von EDX. Die Glasschicht sollte daher als schmutziger Halbleiter und nicht als perfekter Isolator betrachtet werden.

- Das Vorhandensein einer halbleitenden im Gegensatz zu einer isolierenden Glasschicht, die metallische Ag-Kolloide und Verunreinigungen enthält, deutet an, dass die Glasschicht Teil des relevanten Strompfades zwischen dem Emitter und der Ag Metallisierung ist. Dies steht im Gegensatz zu existierenden Modellen, bei denen die Glasschicht als ein Isolator betrachtet wird, der für sich im Volumen keinen Strom leiten würde. Unter Berücksichtigung der Mikrostrukturanalyse der Glasschicht und der Anwesenheit von Ag-Kolloiden und anderen metallischen Ausscheidungen wurde ein Perkolationsmodell eingeführt, bei dem metallische Ag-Kolloide Stromfilamente über die Glasschicht hinweg erzeugen. Dieses Modell ist am besten geeignet, um den Ladungstransport in einem schmutzigen Halbleiter zu beschreiben, der metallische Ausscheidungen enthält.

Eine neue Methodik wurde für diese Arbeit implementiert und die Ergebnisse haben wesen-tliche, neue Erkenntnisse für die Metallisierung von Si-Solarzellen geliefert. Dies wird in den folgenden Kapiteln näher erläutert. Das eingeführte Perkolationsmodell für die Glasschicht basiert auf der Mikrostrukturanalyse und liefert eine quantitative Abhängigkeit des elektrischen Serienwiderstands vom Volumenanteil der Ag-Kolloide. Die Entwicklung des Perkolationsmodells für die Glasschicht ist kein zentraler Teil dieser Arbeit, wird aber an anderer Stelle beschrieben. Vielmehr wurde die hier angewandte Methodik für Solarzellen vom Autor erfolgreich auf andere Materialsysteme, thermoelektrische Materialien und Materialien angewendet, die als IR-Detektoren verwendet werden. Die Ergebnisse wurden veröffentlicht, wurden aber nicht in diese Arbeit aufgenommen.

Thesis Structure

This thesis is divided into three parts and consists of six chapters in total:

Part I: Introduction and basics of Si solar cells

Chapter 1 introduces the current status, theoretical background and understanding of the electrical losses and charge transport mechanisms of screen printed Si solar cells. In addition, metal-semiconductor interfaces and review of the existing models for current paths at the Si/metallization interface are discussed.

Part II: Electron microscopy and specimen preparation for solar cells

Chapter 2 presents a detailed overview of the methodology and strategy applied for the sample preparation, microstructural and chemical analysis of Si solar cells. Details of the advanced electron microscopy and spectroscopy methods such as SEM and TEM and their working principle are demonstrated. A brief description of the temperature-dependent electrical measurements setup and how structure-property correlation works for Si solar cells is given in this chapter.

Part III: Structure-property correlation of high-efficiency, single-crystalline, p- and n-type Si solar cells

This section contains four chapters. A literature background has been established at the beginning of the each chapter.

Chapter 3 focuses on the microstructural, quantitative chemical and electrical properties of p-type planar and textured cells. The effects of paste composition and Si surface orientation on the electrical losses such as contact and series resistance are discussed. Based on the microstructural analysis, a percolation charge transport model has been introduced.

Chapter 4 is dedicated to high-efficiency n-type cells; microstructure, quantitative chemical analysis and electrical characterization. The structure-property correlation of high-efficiency n-type cells is established. The glass layer embedded with Ag colloids and precipitates is found to be relevant for a low contact resistance and hence the current path.

Chapter 5 of this part is devoted to the microstructure and quantitative chemical analysis of the glass layers of p- and n-type solar cells. Various electron microscopy methods have been applied i.e., EF-TEM, DF, BF, Diffraction patterns and quantitative chemical analysis by SEM-EDX and TEM-EDX spectroscopy. The relevance of the glass layer on a sub-micron scale is discussed.

Chapter 6 is dedicated to the NanoSIMS investigations of the dopant distributions across the Si/metallization interface and its influence on the contact and series resistance of the solar cell.

Contents

Part I

Introduction and basics of Si solar cells

Chapter 1

Introduction to Si solar cells

1.1 Motivation

Climate change is a big threat to the future of human's life on Earth. The concentration of green house gases such as CO_2, CH_4 and N_2O is increasing day by day in the atmosphere. Among them, CO_2 which shares approximately 72% of the total emission of the greenhouse gases is a primary cause of the global warming that emitted through human activities. The burning of fossil fuels (i.e., coal, oil and natural gases) combustion and deforestation are constantly adding an unprecedented amount of CO_2 to the atmosphere. This in turn traps the sun light and heat the Earth's surface. Consequently, the risks of global warming have increased significantly in the past years. Recently, according to the report by National Aeronautics and Space Administration (NASA), 16 out of the 17 warmest years have been recorded since 2001 [1]. The level of CO_2 has been recorded at 406.17 ppm in April 2017 which is 30% higher than the highest CO_2 value recorded in 1950. This causes severe changes by increasing the global temperature [2], resulting in more extreme and unpredictable weather; for example increase in sea level caused by the melting of glaciers [3], due to rise in the Earth's surface temperature. Therefore, it is necessary to reduce the consumption of fossil fuels to a large extent and deploy low-carbon energy technologies at massive scale.

There are many renewable sources of energy such as solar energy, wind energy, biomass, geothermal and hydrothermal power. So far, in the current scenario, solar energy has been considered as one of the fascinating and demanding fields among various renewable energy sources. It has several unique advantages: (i) the largest energy resource available on the Earth, (ii) it can be directly converted into electricity through the use of photovoltaic (PV) solar cells and, (iii) PV energy is clean, environment-friendly and non-toxic. While others need an indirect conversion process such as in case of wind energy (wind to kinetic energy) and biomass (biomass to biofuel).

At present, the PV solar market (>85%) is still dominated by wafer based crystalline silicon solar cell technology. The annual PV production has increased up to 75 GW in 2016 with an annual growth of >20 % as compared to 2015. This makes PV one of the fastest growing industries worldwide at present. Figure 1.1 shows the annual production data in GW from 2005 to 2016 [4]. In the last decade, a strong growth in the production volume has been observed wherein China and Taiwan showing the fastest annual production.

Figure 1.2 presents the cumulative PV installations from 2005 to 2016. The cumulated PV production exceeded beyond 300 GWp in 2016. In 2015, China overtook Germany and a large share of PV installation in 2015 and 2016 was observed in China and Japan [4]. In addition, the market share of rest of the world has been increased in the last 5 years.
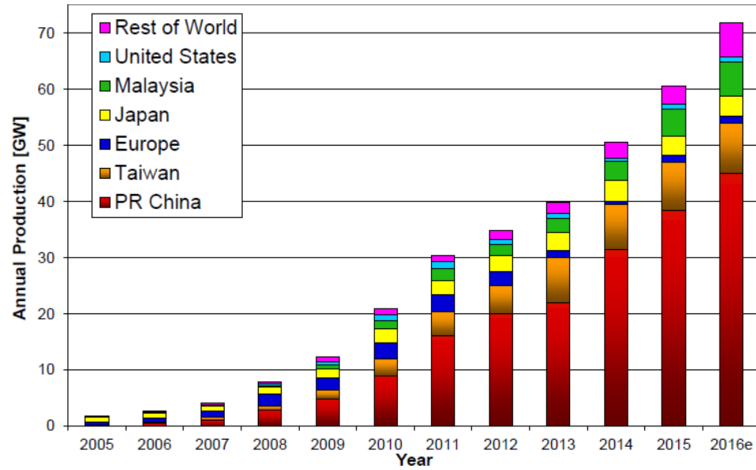
Figure 1.1: World photovoltaic production from 2005 to 2016 (e represents expected data) [4].
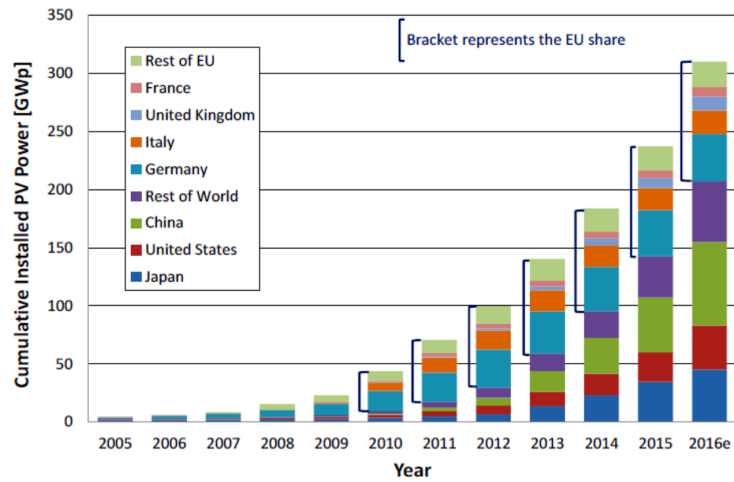
Figure 1.2: Annual cumulative photovoltaic installations from 2005 to 2016 [4].

Another big challenge is to reduce the cost of the PV crystalline Si module. The learning curve of the crystalline Si solar cell is shown in Figure 1.3. As indicated in Figure 1.3 (blue line) a significant decline in the c-Si module sales price was observed during the period of 2006 to 2016. With increasing cumulative PV module shipment, the average selling price decreased by 39% since 2006. As of now, the selling price of a c-Si module is $ 0.37/Wp compared to $ 0.59/Wp in 2015 [5]. The reasons for this huge reduction in price could be due to: (i) a large production in the last years, (ii) reduction in the wafer thickness and, (iii) finally increasing efficiency through optimization of the solar cell technology.

The most effective way of further reducing the cell cost is to increase the cell efficiency by understanding and improving the electrical losses associated with the front side metallization or introducing new cell concepts. The front side metallization contact is usually screen-printed with Ag paste and fired at high temperatures. Focusing on the cell technology, screen-printed front side metallization with Ag paste dominates > 85 % of the PV market and will remain the main stream technology because of its high throughput, simplicity and cost effectiveness. The contact quality of the screen printed front side metallization strongly depends on the contact microstructure as well as the chemical composition of the paste and the firing conditions.
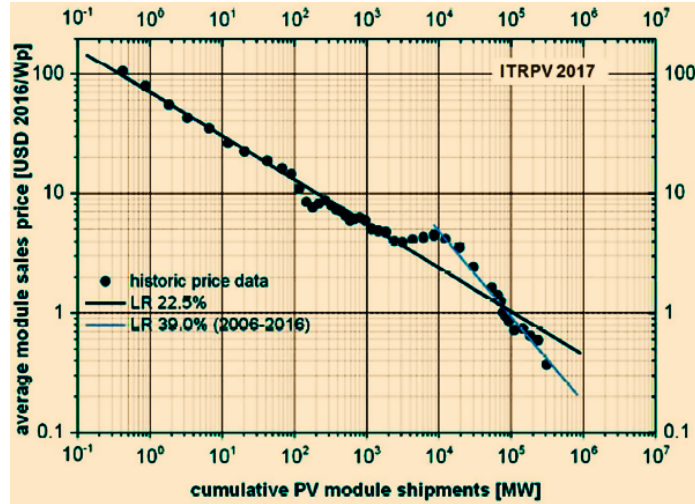
Figure 1.3: Annual cumulative photovoltaic installations from 2005 to 2016 [5].

It is, however, well known that the efficiency of screen printed with Ag metallization contacts is limited by electrical losses across the Si/metallization interface i.e., the contact resistance between the Si emitter and the Ag metallization. The contact resistance at the Si/metallization interface contributes to the series resistance of the cell and, therefore, understanding and minimizing of such losses will further improve the efficiency of the solar cell.

The goal of this thesis is to better understand the contact formation and ohmic losses across the Si/Ag metallization interface. For this detailed investigations have been carried out on standard p- and n-type cells and presented in this thesis in a systematic manner. Electrical characterization of the cells at room temperatures and as well as low temperatures together with detailed microstructural analysis provide new insight for an improved understanding of the metallization induced phenomena in the space charge region, the emitter and the contact area and hence the current transport across the Si/metallization interface. These investigations yield a sound structure-property-correlation for p- and n- type Si solar cells which is essential for the further improvement of the metallization technology.

1.2   Basic principles of a solar cell

A solar cell converts solar energy into an electrical current by the photovoltaic effect. Figure 1.4 shows a typical cross-section structure of a standard p-type Si solar cell with n^{++} emitter. In simple words, a solar cell is a large area diode with a thin 300 nm heavily doped n^{++} emitter and a relatively thick base (p-type, typically 180 μm). On the top surface, a SiN_X antireflection coating and Ag contacts are deposited using screen-printing technolgy, while on the back side fully covered Al rear contacts are formed [6].

According to the internal photoelectric effect when the incident light interacts with a semiconducting material, at the same time photons are absorbed and yield moving electron-hole pairs. The electron-hole pairs are separated at the p-n junction of the cell yielding an electrical photocurrent, this effect is known as the photovoltaic effect. Electrons are collected on the n^{++} side while holes on the p-side. The photovoltaic effect produces an electric voltage at the contact areas, which drives an electric

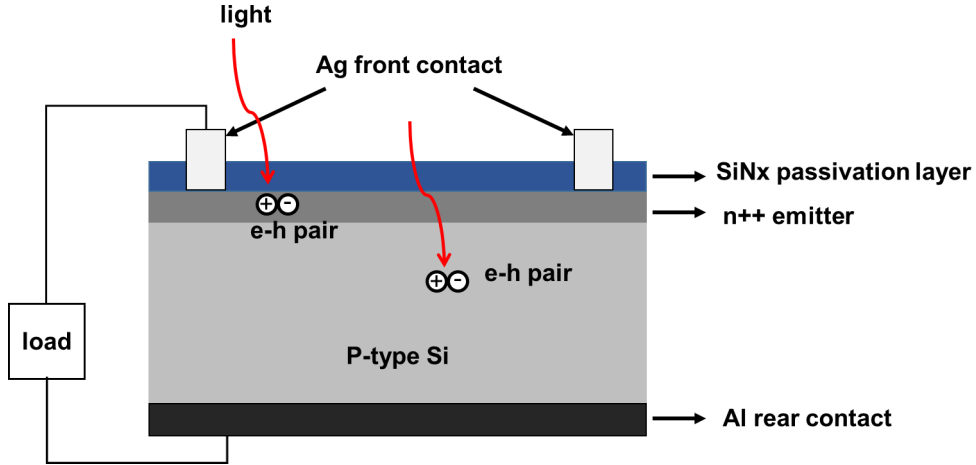current through a load resistance if attached to the cell [7].

Figure 1.4: Sketch of a standard p-type crystalline Si solar cell with front side Ag contacts.

In summary, the basic operational steps of a solar cell are as follows: (i) firstly, the generation of light-generated charge carriers i.e., electron and holes, (ii) secondly, the collection of these lights generated carriers to get more current and voltage across the solar cell and (iii) finally, the dissipation of power in the load and in parasitic resistances.

1.3   I–V characteristics and parameters of a solar cell: the two-diode model

The conversion efficiency (η) is the figure of merit for solar cells which depends solely on the performance of the *I-V* curve under illumination, while the diode relevant properties can be measured in the dark condition. In general, a solar cell can be understood as a current source, a large area diode operated in forward direction, and resistances such as R_S and R_P are connected in series and parallel. The behavior of a solar cell can be described by an ideal diode equation [7]

$$I = I_O \left(\exp(qV/kT) - 1\right) - I_{ph} \qquad (1.1).$$

where, I_O is the saturation current of the emitter and base area, I_{ph} the light generated current, q being the elementary charge, T the temperature and k the Boltzmann constant. However, for a solar cell recombination (in the space charge region) and resistive losses (series and parallel resistance) has to be taken into consideration. Therefore, instead of a simple one diode model, a two diode model is more suitable (see Figure 1.5) for solar cells. The second diode represents the saturation current in the space charge region [7].

The two diode equation by considering all losses can be described as:

$$I = I_{O1} \left(\exp(q(V - IR_S)/n_1 k T) - 1\right) + I_{O2} \left(\exp(q(V - IR_S)/n_2 k T - 1) + \frac{V - IR_S}{R_P} - I_{ph} \right. (1.2).$$

Where I_{O2} is the recombination current in the space charge region and n_1, n_2 are the ideality factor of the first and second diode. For ideal case, the values of n_1=1 and n_2=2 can be used.

Figure 1.6 shows the *I-V* curve of a solar cell measured in dark and under standard illumination condition (illumination with 1000 W/m^2 with air mass 1.5G (AM) spectrum at a cell temperature of 25°C. One can see that the photo-generated current is shifted in the fourth quadrant where the power can be extracted from the diode. The negative current indicates the direction of the photo-generated current which is opposite to the diode current measured in the dark condition.
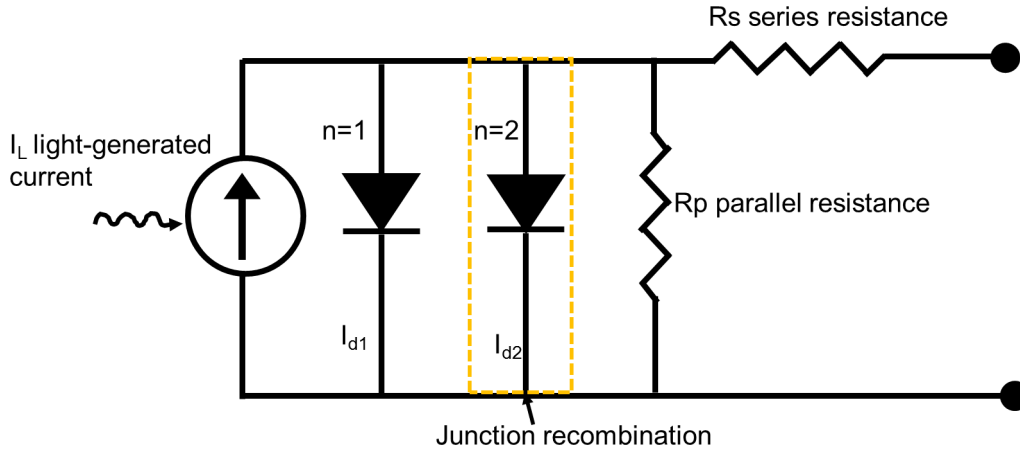
Figure 1.5: Equivalent circuit diagram of a real solar cell using a two diode model [7].

Several parameters such as short-circuit current (I_{SC}), the open-circuit voltage (V_{OC}), series (R_S) and shunt (R_P) resistance, the efficiency (η) and the fill factor (*FF*) are determined from the *I-V* curve.
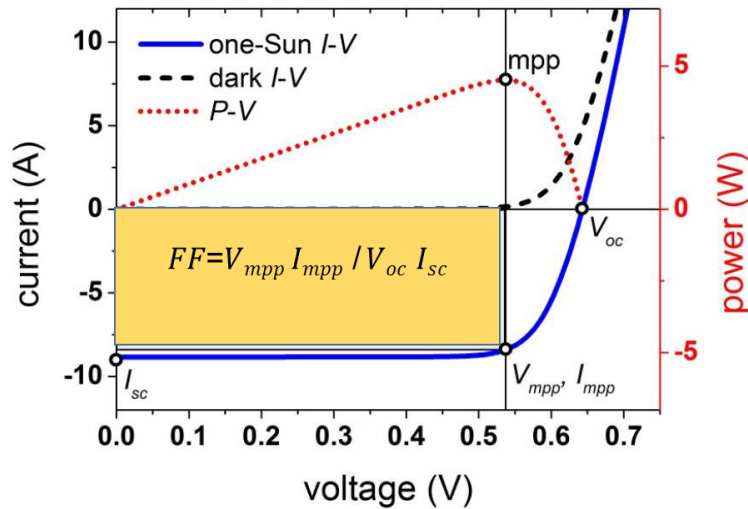
Figure 1.6: Dark *I-V*, one-Sun *I-V* and *P-V* curves of a typical screen-printed mono-Si solar cell (area: 239 cm^2) [data taken from [8] and partly redrawn].

The efficiency of a solar cell (η) can be defined as the ratio of the maximum power point to the incident power of the light.

$$\eta = P_{mpp} / P_{inc} = \frac{J_{SC*}V_{OC*}FF}{P_{inc}} \qquad (1.3).$$

FF is the parameter which describes the maximum power of the solar cell and defined as the ratio of the maximum power point to the V_{OC} and I_{SC} of the cell [see Figure 1.6]. For achieving higher efficiency, FF should be as high as possible.

The influence of the R_S and R_P on the shape of the I-V curve and hence on the fill factor is illustrated in Figure 1.7. It is important to note that in both cases the maximum power point is shifted which affects the FF and hence reduces the efficiency of the cell [7]. Typical values of screen printed Si solar cells are in the range of 76-85%.

Figure 1.8 shows the dark I-V curve plotted in a logarithmic fashion and fitted with a two diode model. The dark I-V measurements are directly related to the diode quality and various cell param-

eters can be extracted such as J_{O1}, J_{O2}, R_S and R_P.
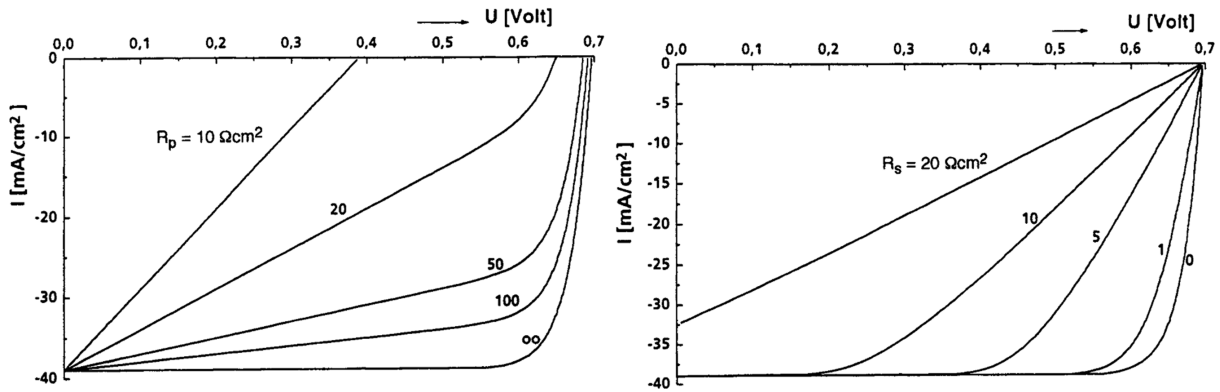
Figure 1.7: Influence of the series and shunt resistance on the I-V curve and cell properties [7].

In the low voltage regime, the I-V curve is dominated by the shunt resistance. In the middle range, it is related to the recombination in the space charge region. At higher voltages, the series resistance impacts the I-V curve of the solar cell.
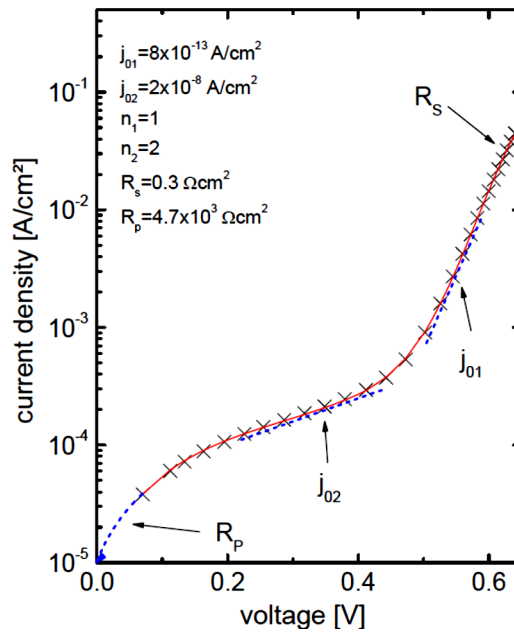
Figure 1.8: Dark I-V curve plotted in a logarithmic fashion [9].

For series resistance evaluation several methods have been explained by Pysch et. al [10] for example; fitting of the I-V curve with the two diode equation or a comparison of an illuminated and the dark I-V curve also known as the shifted I-V method [10].

1.4 Loss mechanisms in a solar cell

The basis for achieving high-efficiency is the reduction of the total amount of losses across the solar cell. These losses can be divided principally into two main areas: (i) optical losses and (ii) electrical losses. A schematic sketch of the electrical and optical losses in a solar cell is shown in Figure 1.9.

1.4.1   Optical losses

The Si surface reflects 35 to 50% of the light incident on the solar cell [7]. Therefore, in order to avoid reflection and increase absorption of the light, a thin anti-reflection coating usually 70 nm SiN_X layer deposited by plasma enhanced chemical vapor deposition (PECVD) method and texturing of the Si surface is implemented.

The metal contacts on the front side are required to collect the photo-generated current from the cell. However, depending on the grid design the front side metallization contact consisting of the fingers and busbars and cover $3-5\%$ of the Si surface. This reduces the photo generated current by shadowing of the light due to the metal contacts. Thus, a solar cell is designed in such a way that it covers only minimum area but at the same time yields a reasonable series resistance [7]. Since minimizing the fingers and busbars result in a high series resistance. Therefore, a good compromise between the grid design and the series resistance losses should be taken into consideration.

Silicon is an indirect semiconductor and it has a low absorption especially in the long wavelength sunlight range, i.e., near to the band edge. Therefore, the sunlight is absorbed on the rear side of the cell without any photoelectric effect. This can be minimized by putting a full surface Al back contact which acts as a reflection layer. When the sun light reaches the rear side of a solar cell, it can be reflected from the Al back surface field (BSF) and can be used for the generation of the charge carriers. Details are given in Ref. [7].

Figure 1.9: An overview of optical and electrical losses associated with a solar cell [7].
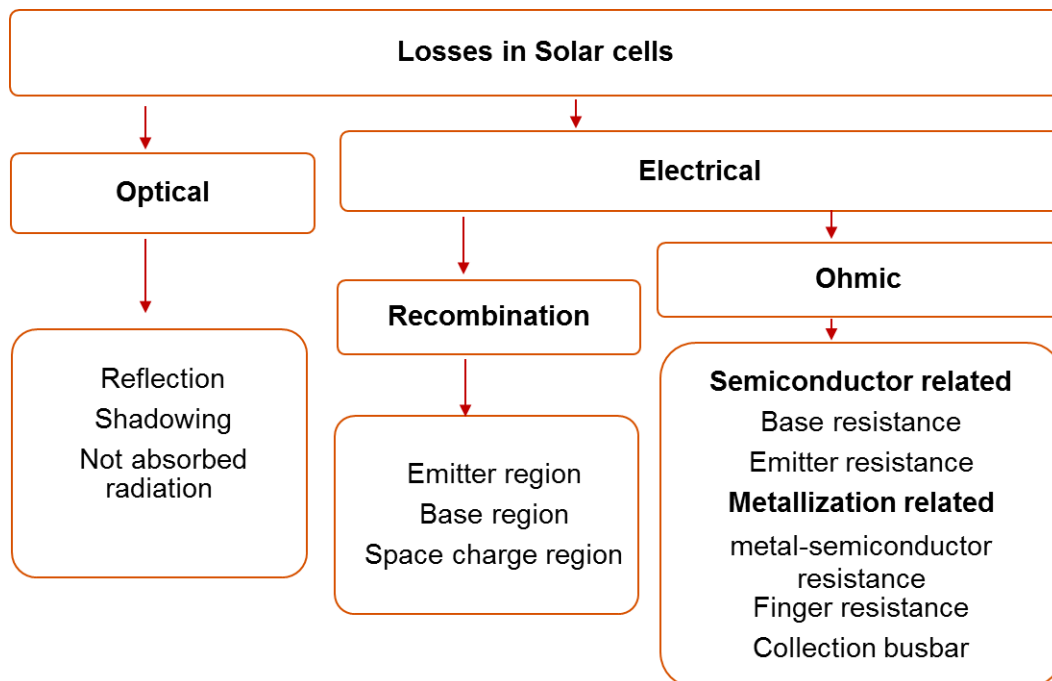
1.4.2   Electrical losses

Electrical losses associated with solar cells are divided into two main categories: (i) ohmic losses i.e., series and shunt resistance, and (ii) recombination losses. Both have a detrimental effect on the cell efficiency.

1.4.2.1 Series resistance losses

The series resistance of a solar cell (R_S) limits the efficiency through the fill factor. For achieving a high-efficiency, minimization of the series resistance is absolutely necessary. This reduces the fill factor and hence the efficiency of the solar cell. The acceptable value of R_S for a screen printed Si solar cell is in the range of 0.5 to <1 Ω cm^2. For a standard solar cell, series resistance consists of a number of resistances as shown in Figure 1.10.
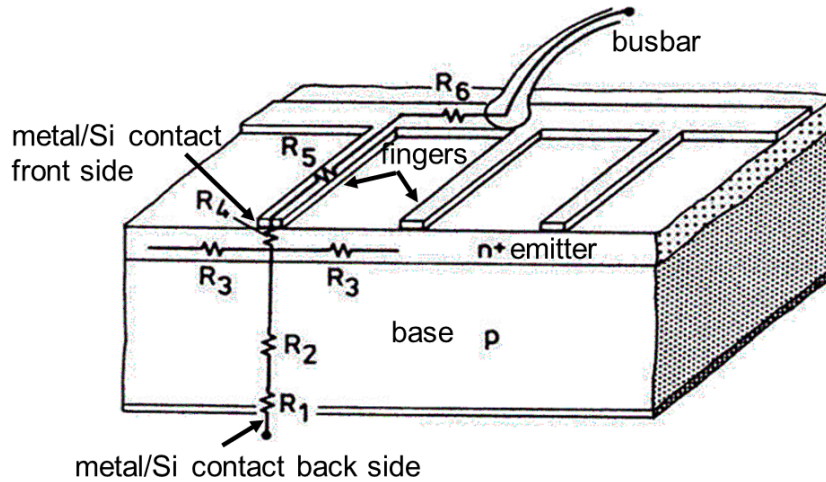
Figure 1.10: Series resistance losses of a solar cell [7].

The series resistance of a cell depends on a number of resistance components in the series and expressed as $R_S = R_1+R_2+R_3+R_4+R_5+R_6$, where R_1 is the resistance of metal/Si contact resistance on the back side, R_2 is the base resistance, R_3 is the emitter resistance, R_4 is the metal/Si contact resistance on front side, R_5 is the finger resistance and finally, R_6 is the busbar resistance [7].

In order to reduce resistive losses associated with the front side metallization, the contact resistance R_4 has to be minimized and will be analyzed in this thesis. The contact resistance is determined by the microstructure features appear at the Si/metallization interface.

1.4.2.2 Shunt resistance losses

In general, the diode quality of a semiconductor device is decided by the shunt resistance (R_P). For Si solar cells, the shunt resistance value of >10 kΩ. cm^2 is required, to avoid short circuit or leakage along the edges of the solar cell. There are several reasons for R_P losses in a solar cell such as; leakage current through the edges of the cell, impurities, crystal defects (micro cracks and grain boundaries) and penetration of the front metal contact at the emitter and the space charge region [7]. These effects are considered by a shunt resistance and degrade the cell performance by providing an alternate current path for the light-generated charge carriers and hence reduce the current and voltage of the solar cell.

1.4.3 Recombination losses

Solar cell under illumination generates electron and hole pairs, the concentration of charge carriers i.e., electrons and holes tend to relax back toward their thermal equilibrium stage via a process

known as recombination. In this process, an electron falls from the conduction band to the valence band and eliminate a valence band hole [11, 12, 13]. The average time between the generation and recombination of an electron-hole pair is known as the carrier lifetime (τ). The light generated minority charge carriers on both p- and the n- side of the cell must reach the p-n junction by a thermal diffusion process and contribute to the current generation.

For screen-printed Si solar cells, a high carrier lifetime and long diffusion length are the key requirements for collecting more charge carriers before they recombine with each other. However, in a real solar cell, a typical emitter surface doping concentration of about $N_D > 1 \times 10^{20} \text{cm}^{-3}$ is usually implemented resulting in high recombination losses. These losses can be divided into: (i) band to band radiative recombination, (ii) recombination through defect levels and surface states also known as SRH recombination and (iii) auger recombination and are shown in Figure 1.11.
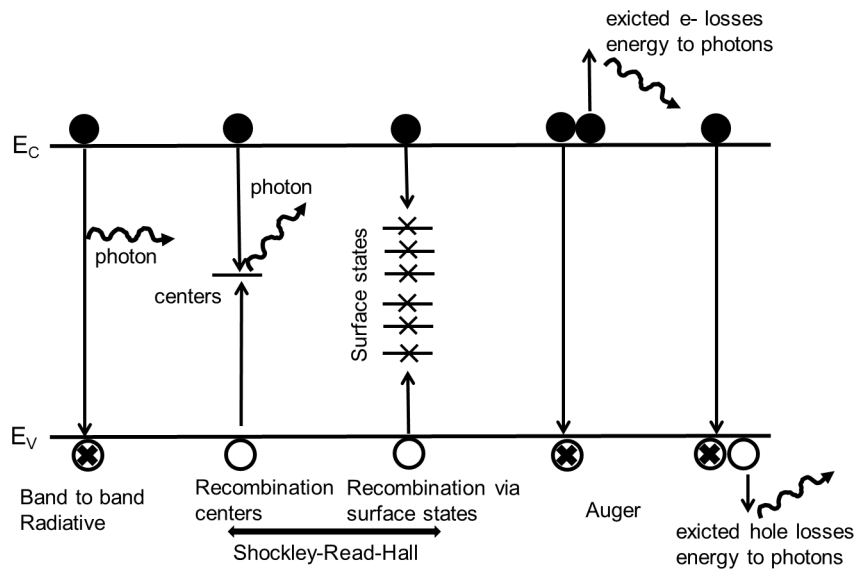
Figure 1.11: Recombination process in a solar cell (i) band to band recombination, (ii) recombination via defects centers or via surface states and (iii) auger recombination [11].

(i) Radiative recombination is the inverse process of the optical absorption. The electron in the conduction band recombines with a hole in the valence band and the excess energy of the electron is released by the emission of a photon. It plays a negligible role for indirect semiconductors such as Si.

(ii) For a standard solar cell, auger and SRH recombination are the main mechanisms that affect the efficiency of the solar cell. Recombination via defect levels introduced by impurities and crystal imperfection plays a major role for doping levels of $< 10^{17} \text{ cm}^{-3}$. Impurities might yield energy levels deeper in the forbidden band, which act as traps or recombination centers for charge carriers. Recombination takes place in the bulk part of the material, at the p-n junction and surfaces of the semiconducting material.

Electrons fall from the conduction band onto these traps/surface states and then to the valence band. These surface states act as effective recombination centers and were first described by Shockley, Read and Hall and also known as SRH recombination [7, 11, 12]. The impurity density at the surface of the semiconductors can be decreased by passivating the surface with a thin passivation layer.

Recombination losses at the interface between the p-type base and the metallic contact at the back side can be reduced by the creation of a highly doped back surface field. This junction (high-low

junction) is also known as a "back surface field" (BSF) and acts as an electrical mirror for the charge carriers [7].

(iii) Auger recombination is the dominant recombination process which requires at least three particle interactions and it's valid for a doping concentration of $> 10^{18}$ cm^{-3}. An electron transfers its energy to a second electron in the conduction or valence band. This excited electron loses its excess energy in a series of collision with the crystal lattice. In heavily doped Si solar cells, Auger recombination process limits the life time of the charge carriers and thus the efficiency of the solar cell [7].

1.5   Metallization and metal-semiconductor interface

Metal-semiconductor devices were identified as useful because of their properties such as rectifying ac signals in the second half of the 19th century. A metal pin was pressed against a mineral with that a metal-semiconductor interface was established [12, 13]. In the first half of the 20th century, Walter Schottky and others did pioneering work to explore the rectifying effect in devices. These were the first steps of semiconductor physics and this was the necessary ground work for inventing the transistor in 1948 [14]. Despite the great experimental evidence and usefulness of such device, the theoretical explanation of the rectifying contacts took long to realized the properties of metal-semiconductor contacts. The understanding of Schottky barriers at metal-semiconductor interfaces took decades and the role of the atomic structure at the interface determining the Schottky barrier height (SBH) was realized by Tung [15].

It turned out that the orientation of the Si substrate plays a key role for the SBH of epitaxially deposited silicide films (see Figure 1.12). It was not before 1993 that a paper of Tung appeared, "Schottky barrier height – do we really understand what we measure?".
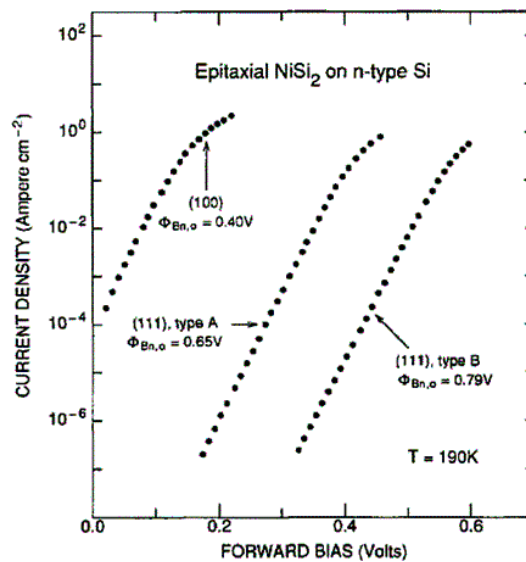
Figure 1.12: Schottky barrier heights on differently oriented Si surfaces [15].

For monocrystalline Si solar cells with front side metallization, the metal-semiconductor contacts play a vital role in understanding and minimizing the resistive losses. Fundamental basics of the metal semiconductor contact relevant for solar cells are given in Refs. [16, 17, 18]. It is, however, well known that the contact resistance at the interface substantially reduces the device performance.

10

Therefore, in order to attain optimum device performance, minimization of the contact resistance is absolutely necessary. For achieving maximum efficiency, the metal-semiconductor contact should be as small as possible and should not degrade the performance of the cell. A review of the contact theory on the Si solar cells has been discussed by Schoder et. al and Meire et. al [16].

1.5.1 Theory of Schottky barriers

The metal-semiconductor contact interface has attracted scientific interest over decades, starting before Bardeen´s paper was published in 1947 and ending today with still many unsolved questions around [14, 17, 19]. Since, metal-semiconductor contacts are the backbone of the microelectronic and optoelectronic devices and strongly influence the device performance, functionality, and their reliability. Metal contacts can be made on n-type or p-type semiconductors. There are two different types of metal-semiconductor contacts which are referred to as Schottky contact or rectifying and an ohmic contact or non-rectifying. For rectifying contacts current can flow easily in one direction, but not in the other and the *I-V* characteristic shows a non-linear behavior. In latter case, the current can flow in both directions and the *I-V* characteristics show a linear variation [12, 19].

According to Schottky, if a metal and a semiconductor are brought together then their fermi level starts to align until the thermal equilibrium is reached. Figure 1.13a–c shows the energy band diagram of a metal and n-type semiconductor before and after the contact. The parameters φ_M and φ_S are the metal and semiconductor work functions, χ_S is known as the electron affinity (see Figure 1.13). In order to align the fermi level, electrons transfer from a low work function material (semiconductor) φ_S to a high work function material (metal) φ_M, in case of depletion or rectifying contacts (Figure 1.13c). The transfer of electrons leave behind positively charged donor atoms in the semiconductor side and eventually led to the formation of the space charge region near to the semiconductor surface [12, 13, 19].

In this process, a potential barrier is developed between the metal and semiconductor which restrict the flow of electrons from metal to semiconductor. This barrier is known as Schottky barrier φ_B. The band bending occurs only in the semiconductor side to align the fermi level on the both side [12, 13].

$$\varphi_B = \varphi_M - \chi_S \qquad (1.4).$$

where φ_B is the Schottky barrier of the metal-n type semiconductor, φ_M is the metal work function and χ_S is the electron affinity of the n-type semiconductor.

Theoretically, the Schottky barrier height depends on the work functions of the semiconductor and the metal and based on this, three cases are possible for the metal-semiconductor contacts as shown in Figure 1.13a–c.

(i) Accumulation type when $\varphi_M < \varphi_S$, in this case, for fermi level alignment electrons flow from the metal and accumulated onto the semiconductor surface. Because of the band bending, the majority charge carriers i.e., electrons can flow freely from semiconductor to metal and vice versa.

(ii) Neutral when $\varphi_M = \varphi_S$, no band bending occurs at the junction and electrons can flow easily from the semiconductor to metal while they face a small barrier when flowing from the metal to the semiconductor side.

(iii) Depletion type contact is obtained when $\varphi_M > \varphi_S$ and is shown in Figure 1.13c. In this case, a potential barrier (SBH) is formed at the metal-semiconductor interface.
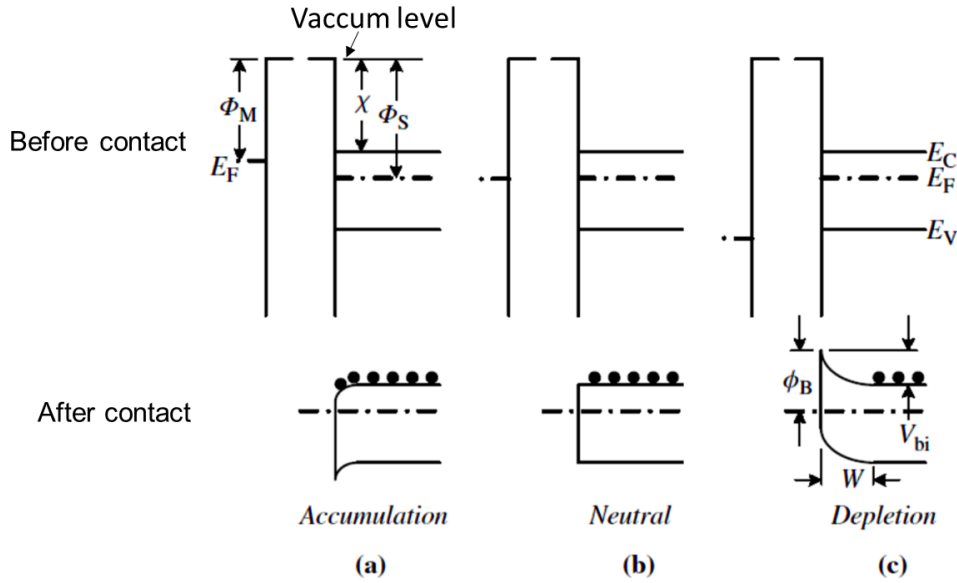
Figure 1.13: Energy band diagram of a metal and n-type semiconductors (a-c) before and after the contact. Three types of contacts are formed (a) accumulation or ohmic type, (b) neutral type, and (c) depletion or rectifying type [image taken from Schroder et al. [19].

Aforementioned, if the metal work function is smaller than the semiconductor then the contacts are of ohmic/accumulated type since the majority charge carriers can flow easily across the junction. However, there is no experimental evidence of the accumulated contacts between Si and the metal, rather depletion contacts are observed [16].

For a real metal-semiconductor contact the direct proportionality (see Figure 1.14) between the metal work function and the barrier height has never been experimentally verified. This is due to the effect of surface states at the metal-semiconductor interface, as well as the image force lowering the barrier height [12]. In fact, these interface states are caused by surface defects/ impurities present in the semiconductor and acting as donors/acceptors. The concept of interface states was first proposed by Bardeen et. al [14] and plays a key role in understanding the contact formation.
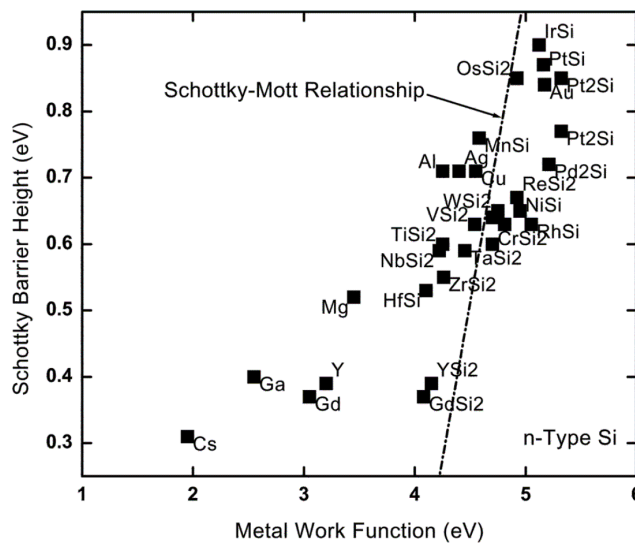

Figure 1.14: Experimentally measured barrier heights in relation to the metal work function for n-type Si. The straight line marks the prediction of the Schottky-Mott rule. A barrier height of > 0.7 eV was observed for n-Si/Ag contacts [image taken from Tung et al. [20].

Fig. 1.14 shows the experimentally measured barrier heights of different metal silicides for n-type silicon. A good disscusion of understanding the metal-silicides contacts is given by Tung et. al [20]. In his review article Tung et. al suggested that the SBH depends critically on the atomic structure of the metal-semiconductor (MS) interface. It turned out that the role of atomic structure at the metal-semiconductor interface determines the SBH as realized for epitaxially deposited silicide films.

1.5.2 Current transport mechanism

Details of the current transport across a metal-semiconductor junction are given in Refs. [12, 13, 19, 21]. There are three different mechanisms for current transport in a metal semiconductor interface which depends significantly on the temperature and doping concentrations (N_D) of the semiconductor side [21]. These mechanisms can be described on the basis of doping concentrations in the semiconductor side and are shown in Figure 1.15:
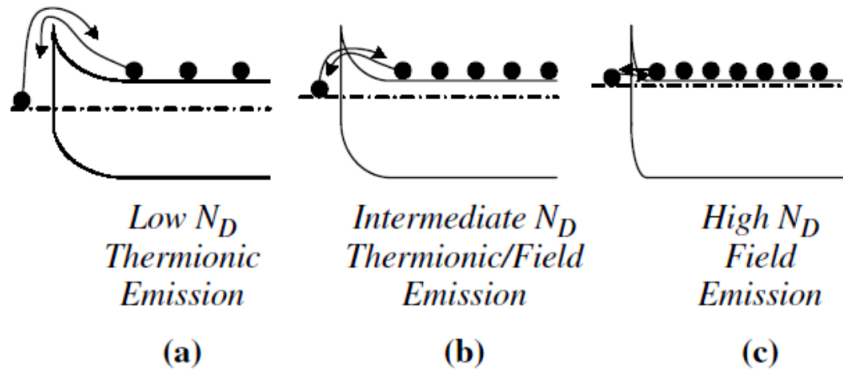

Figure 1.15: Current transport mechanism in a metal-semiconductor contact (a) thermionic emission (TE), (b) combination of thermionic and field emission (TFE) and (c) field emission (FE), respectively [image taken from Schroder et al. [19].

(i) the thermionic emission (TE), is valid for $N_D < 1 \times 10^{17}$ cm^{-3}, where the current transported only by thermal activated charge carriers over the potential barrier, (ii) the field emission (FE), which describes the tunneling of charge carriers through the potential barrier and is valid for a doping concentrations higher than $N_D > 1 \times 10^{19}$ cm^{-3} and, finally (iii) a combination of type (i) and (ii) known as the thermionic field emission which is valid for a doping concentrations between the thermionic and the field emission [19] .

1.5.3 Specific contact resistance

A figure of merit of ohmic contacts between a metal and a semiconductor is decided by the specific contact resistance. This can be expressed as the derivative of current density with the voltage at zero bias.

$$\rho_C = [\partial J / \partial V]^{-1} \, |_{V=0} \, \Omega \, cm^2 \qquad (1.5).$$

For a screen printed Si solar cells with front side metallization, a typical emitter surface doping concentration of about $N_D > 1 \times 10^{20}$ cm^{-3} is usually implemented for achieving a low contact resistivity between the Si emitter and Ag metallization. In this range, FE is the dominant current transport mechanism where tunneling through the potential barrier is relevant.

However, for a standard screen printed contacts, a high-temperature firing process is required which results in an excess etching of the Si emitter or incorporation of impurities from the Ag paste to Si emitter. Moreover, none of these models have been experimentally verified the contact resistivity values for screen printed solar cells which are always higher than the theoretical values [7, 12]. There are several reasons for this: (i) the contact microstructure of the screen printed Ag pastes is not homogeneous, (ii) an interfacial glass layer has been identified at the Si/metallization interface, (iii) conductivity of the glass layer and (iv) pyramidal Ag nanocrystals are penetrating deep into the Si surface. This has detrimental effects both on the contact resistivity and hence on the efficiency of the cell. Since the contact resistance is the one term which contributes to the series resistance of the cell.

The contact resistivity for TE, FE, and TFE depends on the doping concentrations and can be expressed by following equations. For low levels of doping (TE): $\rho c \propto \exp{(\varphi_{Bn}/\kappa_B T)}$, whereas for moderate doping concentrations (TFE) the functional dependence of [21] $\rho_C \propto \exp{(\varphi_{Bn}/\sqrt{N_D}}.\coth(E_{00}/\kappa_B T)$ was observed and finally for a high doping (FE), $\rho c \propto \exp{(\varphi_{Bn}/\sqrt{N_D}})$ where φ_{Bn} is the barrier height between the metal and n-type silicon, N_D is the doping concentration, T is the temperature κ_B is the Boltzmann constant and E_{00} is the energy term which is related to the tunneling probability. The theoretical dependence of the contact resistivity on the doping concentration is shown in Figure 1.16.
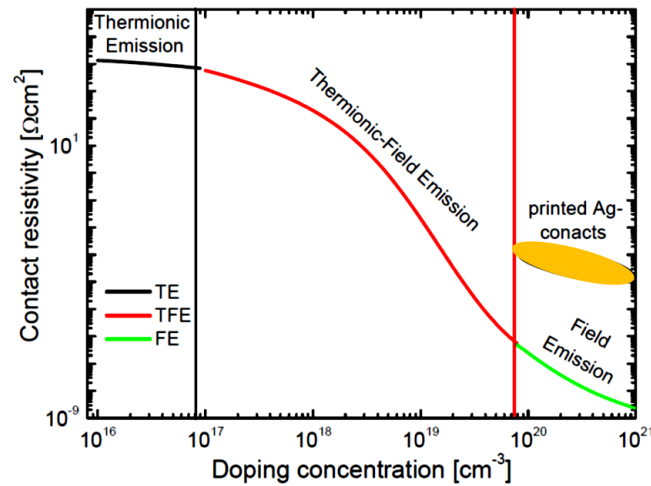
Figure 1.16: Shows the theoretical contact resistivity plot as a function of doping concentrations. The marked areas are related to different current transport mechanisms depending on the doping level. The screen printed Ag contact resistivity is also shown in the image [22].

It is interesting to note that for low doping (TE), contact resistivity is almost independent of the doping concentration. As N_D increases a strong reduction of the contact resistivity is seen. This strong drop is attributed to the reduction of the barrier width for high doping concentrations and thus increasing the tunneling probability across the thin potential barrier [7, 12, 19].

1.6   Review of the existing models for contact formation

Understanding the role of screen printed front side contacts is one of the main challenges for improving the contacting of mono-crystalline p-type silicon solar cells with n-type emitters. With respect to the current paths, different hypotheses exist in the literature, which are still under debate and were

reviewed by Schubert et al [23]. The basic understanding of the Si/metallization contacts is; screen printed front side contacts yield a complex Si/metallization interface. At this contact, Ag nanocrystals are formed at the Si surface and are covered by a glass layer containing metallic Ag colloids.

In the literature, two main hypotheses for current transport mechanisms exist, whereas the dominating current path is still under discussion [23, 24, 25]: (i) current is transported via silver crystallites that penetrate the silicon surface and electrically contact the emitter (see Figure 1.17 a) [24]. They are either in direct contact to the silver bulk of the contact finger or covered by a thin (up to a few nanometers) glass layer, (ii) current is transported via a (thin) glass layer between the silicon surface and the contact silver bulk (see Figure 1.17 b) [25]. This model suggest that a tunneling mechanism (likely assisted by nano-Ag colloids) is responsible for current extraction.
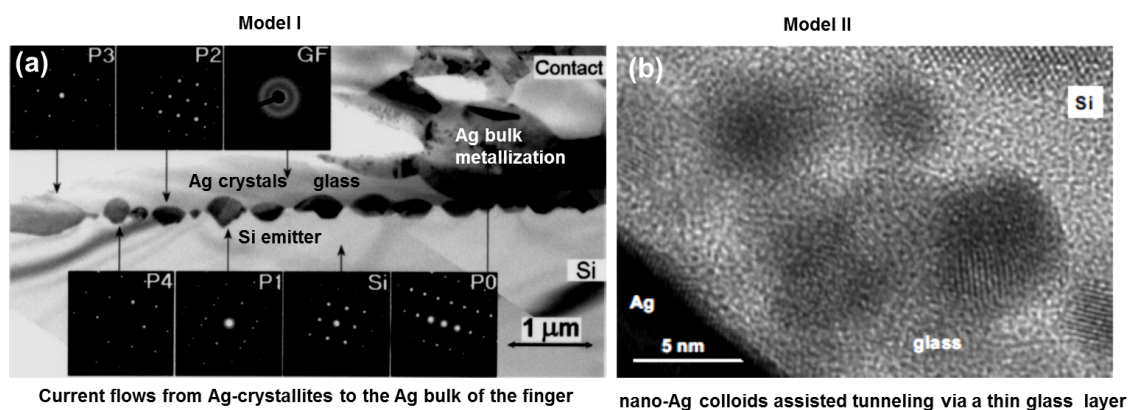

Figure 1.17: Overview of the different models for current paths across the Si/metallization interface: (a) current flow from the emitter into the Ag crystallites that are directly connected to the Ag bulk of the contact and (b) nano Ag colloids assited tunneling through the glass layer [24, 25].

However, up to now, the relevance of these models is still unclear for screen-printed metallization contacts. Unlike the well-defined interface properties of metal semiconductor contacts as applied in microelectronics, screen printed front side silver contacts of crystalline silicon solar cells exhibit a complex interfacial region. At this contact interface, a glass layer of up to several hundreds of nanometers exists which might contain metallic nanoparticles and other precipitates.

Recently, we have highlighted the significance of the glass layer by measuring the chemical composition and analyzing the microstructural features at the Si/metallization interface. The essential results are: (i) for high-efficiency p-or n-type cells we observed a high density of Ag colloids in the glass layer, (ii) chemical analysis of the glass layer was measured indicating that metallic particles such as Ag, Pb, and Zn are dissolved in the glass layer. By considering above arguments, instead of tunneling [25], a percolation model was proposed [26, 27] wherein Ag colloids generate current filaments with reduced resistivity in the glass layer. The role of Ag colloids in the glass layer will be pointed out in the next chapters.

Part II

Electron microscopy and specimen preparation

Chapter 2

Advanced Electron Microscopy and Specimen Preparation

2.1 Introduction

In this thesis, electron microscopy methods such as scanning electron microscope (SEM) and transmission electron microscope (TEM) have been extensively applied to single crystalline p- and n- type Si solar cells. The structure-property correlation has been established for high-efficiency p- and n-type cells. For solar cells, a special care was taken during the sample preparation and microstructural features were investigated in detail. Microstructural features will be identified as, e.g. wetting behavior of the metallization paste, Ag nanocrystals/colloids formation, the chemical composition of the glass phase, effect of the Si surface orientation and the role of the passivation layer (SiN_X) etc. and linked to the measured series and contact resistances.

Microstructural analysis covering a large length scale from 100 μm down to 1 nm by electron microscopy techniques as shown in Figure 2.1.
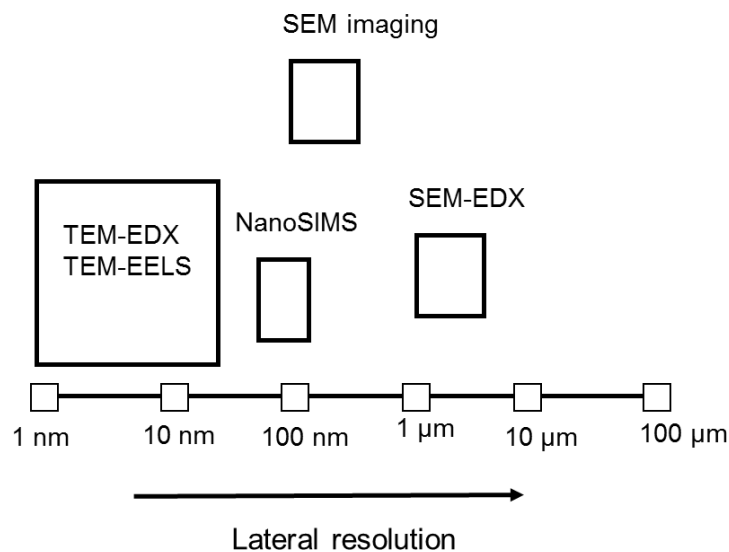
Figure 2.1: Lateral resolution and accuracy of various electron microscopy methods applied to investigate the microstructure of the solar cell.

The physical properties i.e., the contact resistance between the Si emitter and the Ag metallization interface strongly depends on the microstructural features as well as the orientation of the Si surface. Understanding the effects of metallization on the physical properties of the solar cell will pave a new way for minimizing the electrical losses and hence increasing the efficiency. Furthermore, the characterization of the Si/metallization interface is challenging because of several reasons: the width of the metallization finger and thickness was 80 μm and 30 μm respectively and therefore, a careful, artifact free sample preparation is required in order to investigate the microstructural and chemical

analysis of the contacts and establish its correlation to the physical properties.

The following methods were applied covering a length scale down to nm; SEM was used in both modes: (BSE) backscattered and secondary electron (SE) to investigate the surface morphology, compositional information and chemical analysis of the Si/metallization contacts. BSE images are particularly useful in the phase identification and contain compositional information because they are directly related to the atomic number and the density of the elements. Conventional bright-field (BF) and dark-field (DF) imaging, EF-TEM imaging, selected area electron diffraction patterns (SAED), energy dispersive X-ray (EDX), and electron energy loss spectroscopy (EELS). TEM is useful for structural and chemical information down to nm scale. Basic principles of the electron microscopes and sample preparation strategy are described in this chapter. NanoSIMS in the SEM has been applied to imaged dopant elements i.e., P and B with a high lateral resolution of 80 nm.

2.2 Scanning Electron Microscopy (SEM)

Details of the basic operational mechanisms of SEM are given in Refs. [28, 29, 30]. SEM is a quite simple, robust and fast technique which requires only minimum sample preparation. In SEM, a focused electron beam is scanned (raster scan) on the sample surface and generates a variety of signals, for example SE, BSE and X-rays (as shown in Fig 2.2). These signals can be measured by a detector (SE, BSE and EDX detector) to produce SE images, BSE images or EDX- elemental mapping and contain information about the surface topography, composition, chemical information and orientation of the specimen. SE images are commonly used to measure the surface topography (5 nm) while BSE images can provide information about the distribution of elements in the specimen. The intensity of BSE signals depends significantly on the atomic number of the specimen. The depth distribution of the different signals is shown in Figure 2.2.

In addition, characteristic X-rays are generated by an inelastic interaction of the electrons with the atoms of the specimen. When an electron beam removes an inner shell electron from the specimen, at the same time a high energy electron fills the vacancy and release energy in the form of X-rays [28, 29]. These characteristic X-rays are used to identify the elemental composition of the specimen. However, X-rays are generated deeper in the excitation volume and can be absorbed within the specimen. The excitation volume depends on number of parameters i.e., accelerating voltage, density and atomic number of the specimen [28, 29, 30].
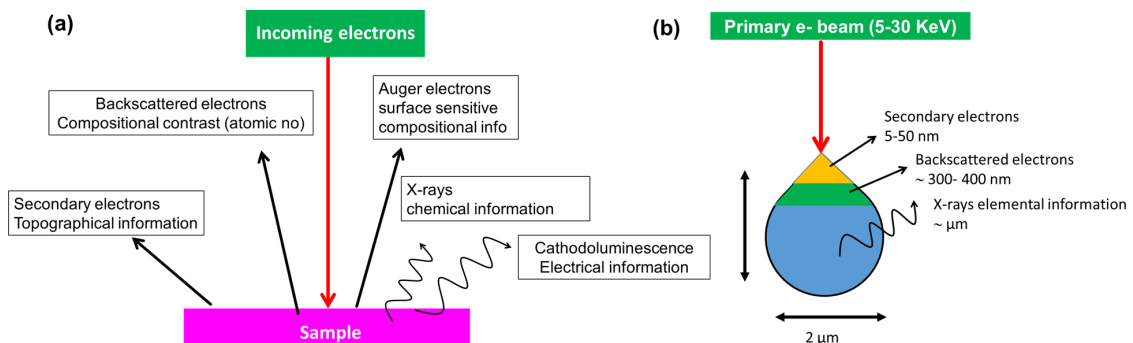

Figure 2.2: (a) shows the variety of signals generated when an electron beam interacts with the specimen and their use in the micro-structural and chemical analysis. (b) represents an excitation volume from where different signals are produced as a function of depth.

For quantitative chemical analysis by SEM, usually, a ZAF correction is required where Z, A and F are the atomic number, absorption, and fluorescence correction factors [28, 29]. These corrections are important for precisely measuring the chemical analysis of the lighter elements. For details of the chemical analysis of light elements such as boron (B) in MgB_2 please have a look at chapter 2 in the thesis of B. Birajdar [30].

2.3 Transmission Electron Microscopy (TEM)

2.3.1 Transmission electron microscope used

2.3.1.1 Zeiss 912 omega

A photograph of Zeiss 912 Ω TEM is shown in Figure 2.3. Zeiss 912 Ω is equipped with a LaB_6 filament operated at 120 kV and yielding a point resolution of 0.37 nm. A detailed description of the instrument can be found in Refs. [30, 31, 32, 33].
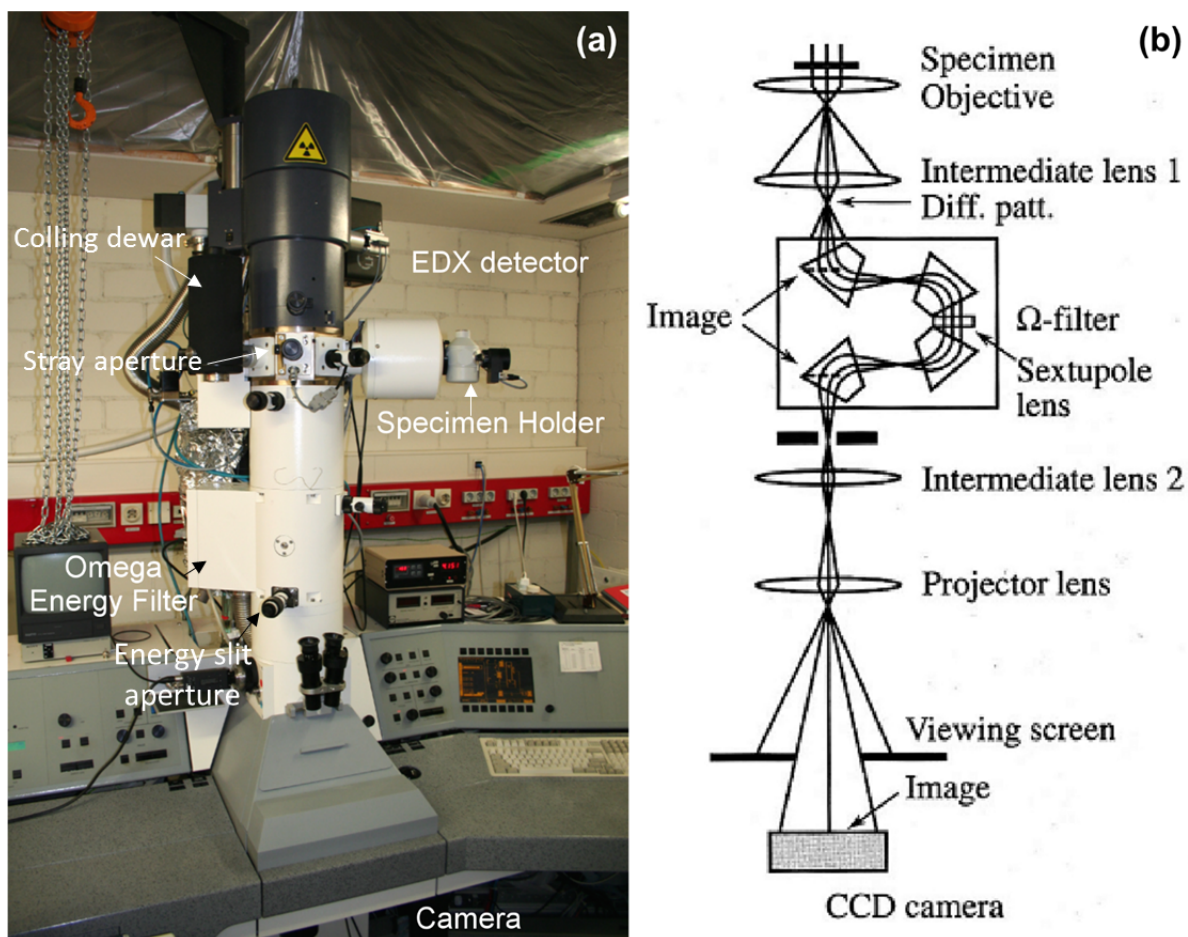
Figure 2.3: (a) Photograph of the Zeiss 912 Omega TEM and (b) the electron-beam path and the Omega in-column energy-filter [33].

The microscope has following features: (i) a Köhler illumination system [34], (ii) an Omega energy filter [35], (iii) an EDX detector with an energy resolution of better than 132 eV at the $Mn-K_\alpha$ line, (iv) a low background double-tilt (tilting range of $60°$ for the X-axis and $60°$ for the Y-axis) holder with an

option of liquid nitrogen cooling and (v) a CCD camera (14 bit, 2048×2048 pixel) [33]. Further details of the Omega energy filter and stray aperture are given in the thesis of N. Peranio and B. Birajdar [30, 31].

Interesting features of this instrument are: (i) in column Omega energy filter and (ii) stray aperture for chemical analysis. The energy filter generates in its exit image plane an achromatic 1:1 image of its entrance image plane. Electrons of same energies are focused at the same point in the energy-dispersive plane of the spectrometer, which is located below the exit image plane, thus forming an electron energy loss spectrum [30, 35]. A slit aperture of variable width is centered around the optical axis in the energy dispersive plane. Electrons which have lost a definite amount of energy in the sample are selected by this aperture and used for further imaging.

A schematic of the stray aperture used in the TEM is shown in Figure 2.4. By introducing stray aperture in the TEM the hole-count artifact could be drastically reduced [31, 36]. These artifacts come from: (i) uncollimated electrons might hit the specimen at thick outer parts of the sample and, thereby, produce spurious X-rays, (ii) stray radiation from the grid and, (iii) from the various apertures used in the microscope. With the stray aperture inserted a high-accuracy EDX analysis in the TEM combined with a sub-micrometer lateral resolution is achieved with an accuracy of <1 at.%. This method has been succesfully developed and implemented by N. Peranio in [36] for precisely measuring the chemical composition of the heavy elements i.e., Bi.

All Images and EELS spectra were acquired using a CCD camera (14 bit, 2048×2048 pixel) and processed by the iTEM software package [37]. A Si (Li) EDX detector (with an ultra thin window) was used to acquire the EDX spectra which are further processed by the INCA software package [38].
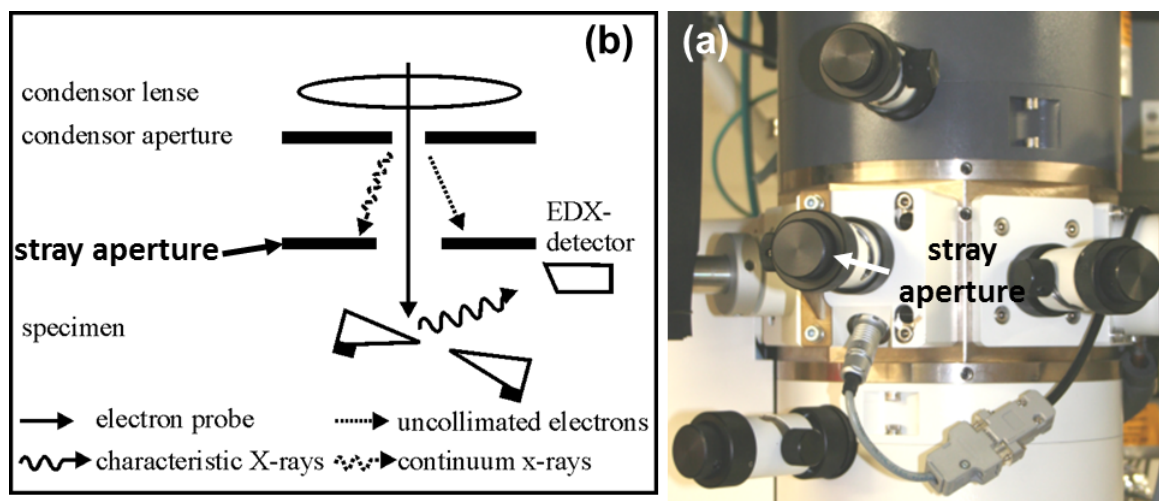

Figure 2.4: (a) shows the magnified view of the apertures used in the TEM and (b) a schematic ray diagram showing the stray aperture [33].

2.3.2 Techniques and acquisition conditions used

In this thesis, the following techniques were applied to characterize high-efficiency Si solar cells using Zeiss 912Ω TEM. (i) Energy-filtered bright-field (EF-BF) and dark-field (EF-DF) diffraction contrast imaging, (ii) Energy-filtered selected area electron diffraction (SAED), (iii) Low-loss electron energy-loss spectroscopy (EELS), (iv) RGB maps by energy-filtered transmission electron microscopy (EFTEM) and (v) Energy-dispersive X-ray (EDX) spectroscopy.

Table 2.1 to 2.3 summarize the acquisition conditions used for characterizing the solar cells by conventional BF, DF, Diffraction patterns, EF-TEM imaging and EELS spectroscopy.

	Imaging	Diffraction Pattern
Condenser aperture	3	3
Objective aperture	3 (3.5 mrad)	none
SAED aperture	none	3 (700 nm)
Width of the energy slit aperture	10 eV	10 eV
Magnifications (kx)	10, 16, 25 31, 50, 63, 80	-
Camera length (mm)	-	290, 720
Acquisition time (s)	2-5	2-5

Table 2.1: Acquisition conditions and parameters used for imaging and diffraction pattern for Si solar cells.

	Solar cells
Width of the energy slit aperture	10 eV
Objective aperture (mrad)	3.5
1st window position (eV)	16 (Si plasmon peak)
2nd window position (eV)	24 (SiO_2, Ag and $Pb - O_{IV,V}$ edge)
3rd window position (eV)	32 (2nd Si plasmon peak)
Magnifications (kx)	10,16 ,31
Acquisition time (s)	5-10

Table 2.2: Acquisition conditions and parameters used for acquiring RGB images for Si solar cells.

Spectra	Emission current (μA)	Spot size (nm)	Obj. Aper. (mrad)	Spectral mag. (x)	Acquisition time (ms)	Times integ.
Low-loss	< 1	10	3.5	63	50-200	20
Core-loss	3-5	50	8.1	63	1-5	10

Table 2.3: Acquisition conditions and parameters used for obtaining low-loss EELS spectra for Si solar cells.

However, different techniques have some advantages and disadvantages depending on the acquisition condition for more details see Refs. [39, 40, 41].

2.4   Conventional Transmission Electron Microscopy

The commonly used techniques in a conventional TEM microscope are bright-field, dark-field imaging, high-resolution imaging and selected area electron diffraction (SAED) patterns [42]. In the TEM, only very thin specimens (5-100 nm) are examined and yields diffraction contrast. As we know that electrons interact strongly with atoms of the specimen via two processes (i) elastic (negligible or no energy loss) and (ii) inelastic scattering (measurable energy loss). The mechanism of elastic scattering process is fundamental for imaging in the TEM. The priniciple of conventional TEM are described in Refs. [30, 32].

In order to enhance the image contrast and make the interpretation of the image simpler, the sample is oriented in such a way that only the transmitted beam and one Bragg diffracted beam g_{hkl} are strongly excited in the diffraction pattern. This condition is known as two-beam condition. Under such condition, the image contrast improves because only one set of lattice planes contributes to the image [42, 43]. Bright/dark-field images under different two beam conditions together with their corresponding g_{hkl} diffraction vectors enable to characterize the defects in the crystal.

In this thesis both images and diffraction patterns were acquired with an energy slit aperture of 10 eV in combination with an in-column Omega energy filter to remove the in-elastically scattered electrons from the final image. Since inelastic scattering increases the background intensity thereby reducing the diffraction contrast in the image.

2.5   Electron diffraction pattern

Electron diffraction contains information about the crystal structure and orientation of the specimen. By SAED diffraction one can get knowledge about the crystalline quality, orientation relationship and texture of the specimen [42]. Therefore, a combination of electron diffraction together with the bright-field and dark-field imaging is crucial for establishing a correlation between real (micro-structural features) and the reciprocal space (diffraction patterns). In this thesis, SAED patterns were acquired on the glass layers of n- and p- type cells. Details are given in chapter 5.

2.6   Analytical Electron Microscopy

The analytical electron microscopy (AEM) offers unique possibilities that can use a variety of signals generated during inelastic interaction between the primary electron beam and the specimen [42]. These signals can be used to identify and quantify the chemical analysis, specimen thickness and elemental mapping with a spatial resolution of 1-100 nm. The most common signals used in the AEM are: (i) X-rays for quantitative chemical analysis, (ii) EELS for specimen thickness, electronic structure of the specimen and phase identification which depends on the position of the plasmon peak. In the next sections, the basics of EELS and EDX spectroscopy in TEM are explained.

2.6.1   Electron Energy-Loss Spectroscopy (EELS)

When electrons pass through a thin specimen, they are scattered by the coulomb interaction with the atoms of the specimen (nucleus and atomic electrons). In this process electrons may lose its energy and undergo an inelastic collision. As a result, an energy-loss spectrum can be recorded by a magnetic prism spectrometer and the final image can be shown in Figure 2.5. The main function of the magnetic prism spectrometer is to separate the electrons according to their energy losses after having passed through the specimen. Further details of the principles of EELS are described in Refs. [30, 32, 42, 44].

A typical energy loss spectrum can be divided into three main regions [41]. The most prominent peak in the spectrum is the zero loss peak, in this region, only those electrons contribute which have lost a negligible energy and those which have excited phonon modes (energy-loss of about 10^{-2}eV).

However, phonon mode can not be resolved by the instrument because the energy resolution of EELS is typically less than 1 eV.

In the low loss region, those electrons contribute which have lost energy losses between a few eV to 50 eV. The includes plasmon (collective oscillations of weakly bound valence electrons) excitations and interband transitions. While in the core-loss region, energy losses higher than 126 eV can be considered which arises from inner shell ionization processes and can be used for elemental analysis.
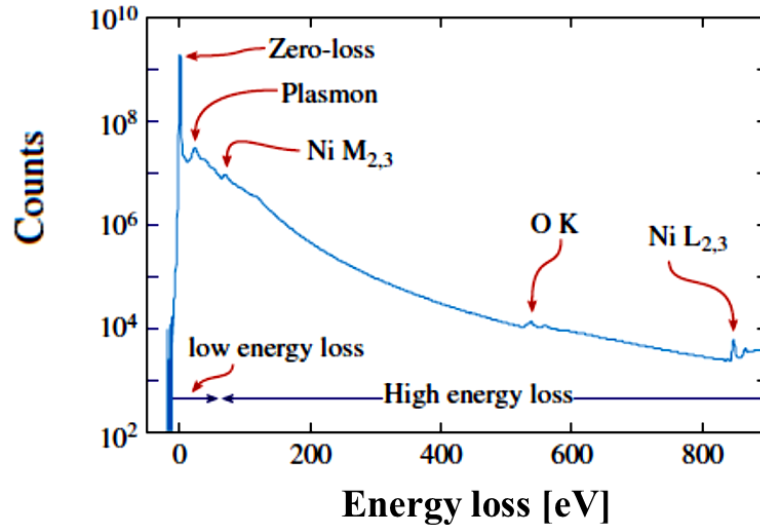

Figure 2.5: An EELS spectrum displayed in a logarithmic intensity on y axis and energy loss on x-axis. Different regions (zero loss, low loss, and high energy loss) are marked in the spectrum.

Electron energy loss spectroscopy in the TEM requires special care particularly important is the thickness of the specimen and the contamination. Therefore, thin and clean specimens are suitable for EELS investigations. In general, the thickness of the specimen should be less than the mean free path of the electrons, in order to avoid multiple scattering. In case of Si, the mean free path is about 60 nm for 120 kV electrons [42, 45].

For the quantification of a specific element of interest the following has to be taken into account: (i) ionization cross-section, σ_K, (ii) number of atoms per unit area, N, (iii) collection angle, β, (iv) energy slit width, $\triangle$ and (v) the edge of interest K. Details are given in Refs. [30, 32, 41, 44]

The relevant ionization edges for elements analyzed in this thesis are given in Table 2.4.

Element	Z	Edges (eV)												
		K	L_I	L_{II}	L_{III}	M_I	M_{II}	M_{III}	M_{IV}	M_V	N_I	$N_{II,III}$	$N_{IV,V}$	N_{VI}
O	8	532	-	-	-	-	-	-	-	-	-	-	-	-
Si	14	-	149	100	99	-	-	-	-	-	-	-	-	-
N	7	401	-	-	-	-	-	-	-	-	-	62	-	-
Ag	47	-	-	-	-	717	602	571	373	367	95	62	-	55
Zn	30	-	-	-	-	135	86	86	8	8	-	-	-	-
Pb	82	-	-	-	-	-	-	-	-	-	893	763	435	142

Table 2.4: Ionization edges of various elements used for the EELS investigations.

Furthermore, these ionization edges can be used to make phase contrast images for Si solar cells. A similar investigation was carried by Z. Aabdin and B. Birajdar for other material systems [30, 32]. These analysis are of great importance and particularly well suited to analyze the complex Si/metallization interface.

2.6.2 Aberration corrected STEM

In 1960 Crewe et. al introduced an alternative imaging method known as STEM [46]. The electron beam is focused to a fine spot typically below 1 Å and scanned over the sample in a scanning field. This can be achieved by putting scanning coils in front of the sample. The illumination system is designed in a way that at each point on the sample illuminated with the beam parallel to the optical axis. High Angle Annular Dark Field (HAADF) detector signal in STEM makes it possible to produce images with strong Z contrast, independent of the sample thickness and that is very useful for the image interpretation [46]. The image in HAADF is formed by incoherent elastically scattered electrons at large angles. Besides imaging STEM offers atomic resolution both in electron energy loss spectroscopy [47] and energy dispersive X-ray [48]. A detailed description of aberration correction imaging in STEM is given by Rolf Erni [46].

The state of art new instrumentation with aberration corrected STEM are available yielding an improved resolution both in the imaging as well as in the spectroscopy. Recent developments in controlling the lens aberration through multipole based aberration correction have enabled to reach sub Å beam sizes and chemical composition imaging at atomic resolution [46]. The mechanism for aberration correction started back in 1936 [49] when Scherzer realized that the electron lenses suffer large aberrations i.e., spherical and chromatic aberrations that limit the resolution of the microscope. In 1947 he proposed various methods to overcome aberrations. Later on some pioneering attempts were applied by Crewe, Rose, Haider and Krivanek et. al and successful implemented of the aberration corrections was demonstrated by Haider et al as late as in 1990s [49].

These new possibilities due to instrumentation provides atomic resolution information about atomic species, local electronic structure and atomic bonding environment on a sub-nm scale [47]. Imaging of Au islands and single Au atom on amorphous carbon at sub A resolution was demonstrated by Batson et. al [50]. STEM imaging and electron energy-loss spectroscopy was applied by Batson et. al to resolve the bonding states of Si atoms across a $Si - SiO_2$ interface [51]. The oxidation state of the individual column of unit cells can be resolved. Furthermore, annular dark-field STEM has been used to image Sb dopants in n-type Si [52]. For high-transition-temperature superconductors chemically sensitive structural information [48] with high Z contrast [53] was reported by Pennycook et. al [54].

2.6.3 EDX microanalysis

An historical prospective of the development of electron probe microanalysis and early approaches for quantitative analysis of bulk samples is described by Scott and Love et. al [55]. The main focus was to obtain characteristics X-ray spectra and introduce methods to deduce the chemical composition of the specimen to an accuracy of 1 at.%. A good discussion of the fundamental basics of characteristics X-rays generation and development of the different methods wavelength dispersive

X-ray (WDX) and energy dispersive X-ray (EDX) is given in [55]. The difference between these methods is: in EDX characteristic X-rays are measured using a solid state detector which works on the principle of electron-hole pair generation while in WDX dispersion is achieved by an analyzing crystals, via Bragg diffraction from its crystal planes. WDX has a better minimum mole fraction detection limit (about several 10 ppm) as compared to EDX (usually about 1 at.%) but require standards [55]. However, X-ray generated within few micron of the surface and therefore X-ray absorption effects (A), fluorescence (F) and atomic number (Z) for the standard (pure) material and the specimen would be different [55]. These corrections are now applied routinely to quantify the chemical analysis and also known as ZAF correction factor [55, 56]. Among them the dominating factor is the absorption correction and any discrepancy in correcting absorption effect would yield significant deviation in the quantitative analysis. A number of methods were applied for thin films and bulk samples and summarized in [55]. However with the difficulties in the accuracy of such methods the development of new standardless methods was first proposed by Cliff and Lorimer in 1975. Because of its simplicity, this method is currently applied as the standard method for calibration and quantification of the chemical analysis by EDX in the TEM.

2.6.4 TEM-EDX quantitative chemical analysis by Zeiss 912

The Zeiss 912 instrument was developed in the 1980s. Interesting features of the Zeiss 912 instrument are column omega energy filter and a stray aperture for chemical analysis. By introducing a stray aperture in the TEM the hole-count artifact could be drastically reduced. Since no STEM unit was available in the instrument, therefore, a combination of EDX and EF-TEM imaging was applied to get phase mapping as well as EDX point spectra. We have investigated both bulk samples as well as thin films.

For solar cells, the emitter region is covered by a 500 nm thick glass layer containing Ag colloids and other precipitates on a 10 nm scale. Therefore, instead of STEM, a combination of the EDX and EF-TEM imaging was applied. EF-TEM imaging is particularly suitable to effectively examine the essential features of the microstructure by generating phase maps. The goal was to investigate the phase formation and chemical analysis of the glass layer and precipitates, not the atomic structure of the Si/metallization interface.

The quantification of characteristics X-ray peaks in TEM-EDX is fundamental to Cliff-Lorimer equation [42, 55]. TEM-EDX has several unique advantages: (i) simple equation, and (ii) standard less method as compared to WDX. The limit of 1 at.% accuracy in the EDX depends on the counts in the spectra, peak to background ratio and the calibration of the Cliff-Lorimer K factors [30].

$$\frac{C_A}{C_B} = k_{AB} \frac{I_A}{I_B} \tag{2.1}$$

where C_A and C_B are the weight percent of element A and B in the specimen, I_A and I_B are the net counts of characteristic X-ray lines, which we measured experimentally. The term k_{AB} is known as the *Cliff-Lorimer factor*. Nonstandard k-factors are close to unity for a large range of elements, this makes EDX a powerful method for chemical analysis [55].

Previous investigations of the light elements by B. Birajdar on superconducting material like MgB_2 and heavy elements such as Bi_2Te_3 by N. Peranio have proven the relevance of this approach [30, 31].

TEM-EDX microanalysis, as was applied in this thesis, is well suited to study the Si/metallization interface, and also applied to other systems such as thermoelectric materials [57] and PbSe infrared detectors [58].

Figure 2.6 represents the EDX spectra of the glass layer of high-efficiency p-type cell [26] that can be described as X-ray counts on the y axis as a function of the energy of characteristics lines on the x-axis. The peak intensity represents the characteristics of the elements in the specimen [42]. Optimum acquisition conditions were applied to identify and quantify the elements with small mole fractions, seen as small peaks in the Figure 2.6.

All spectra were acquired in the TEM and quantitatively analyzed by applying the Cliff-Lorimer k-factor method [36]. EDX spectra were acquired with a spot size of 32 nm, a detector take-off angle of $20°$, a specimen tilt angle of $15°$ and an acquisition time of 300 s with a stray aperture to avoid stray radiation coming from apertures to improve the detection limit [30, 31]. The Zeiss 912 omega microscope equipped with a Si(Li) EDX detector from Oxford instrument and a low-background specimen holder for chemical analysis with an energy resolution of 136 eV at the $Mn - K_\alpha$ line.
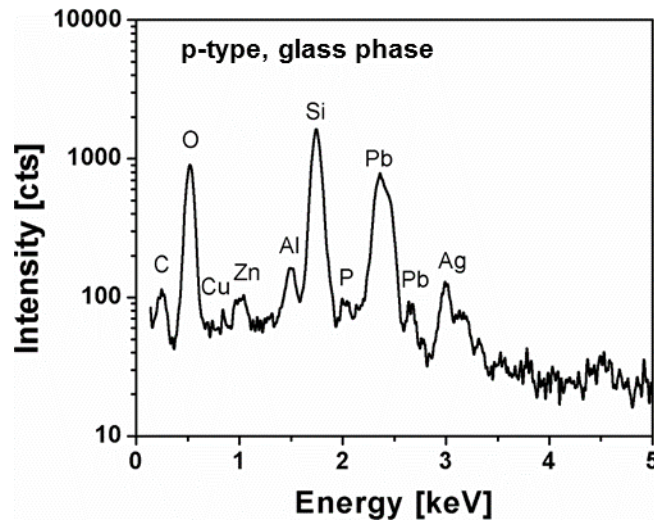
Figure 2.6: TEM-EDX spectra of the glass layer of the p-type solar cell.

The calibrated k-factors used in this thesis for the quantification of the EDX data of different elements are given in Table 2.5.

Element	Z	X-ray line	k-factor	Line energy [keV]
O	8	$K_{\alpha 1}$	2.25	0.524
Si	14	$K_{\alpha 1}$	1	1.73
Ag	47	$L_{\alpha 1}$	1.76	2.98
Zn	30	$K_{\alpha 1}$	1.54	8.63
Al	13	$K_{\alpha 1}$	1.03	1.48
Ti	22	$K_{\alpha 1}$	1.09	4.51
P	15	$K_{\alpha 1}$	0.99	2.01
Pb	82	$L_{\alpha 1}$	3.04	10.55

Table 2.5: Cliff-Lorimer k-factors for 120 keV primary energy and relevant X-ray lines of elements used for the quantitative analysis.

2.6.5 EFTEM (ESI) imaging technique

In EF-TEM [39, 42] imaging electrons of definite energy losses are used to form images. This technique is particularly important for the identification of the phases on a sub-micron scale. A similar method was implemented by B. Birajdar for identification of B rich secondary phases [30] and phase mapping of light elements. Details of the acquisition and interpretation can be found in chapter 5. An example of EF-TEM imaging is shown in Figure 2.7.

To investigate the different phases presented at the Si/metallization contact interface, we used superimposed energy-filtered TEM (EF-TEM) imaging techniques (referred to as RGB imaging) by making a colorful phase map of the area under investigation.
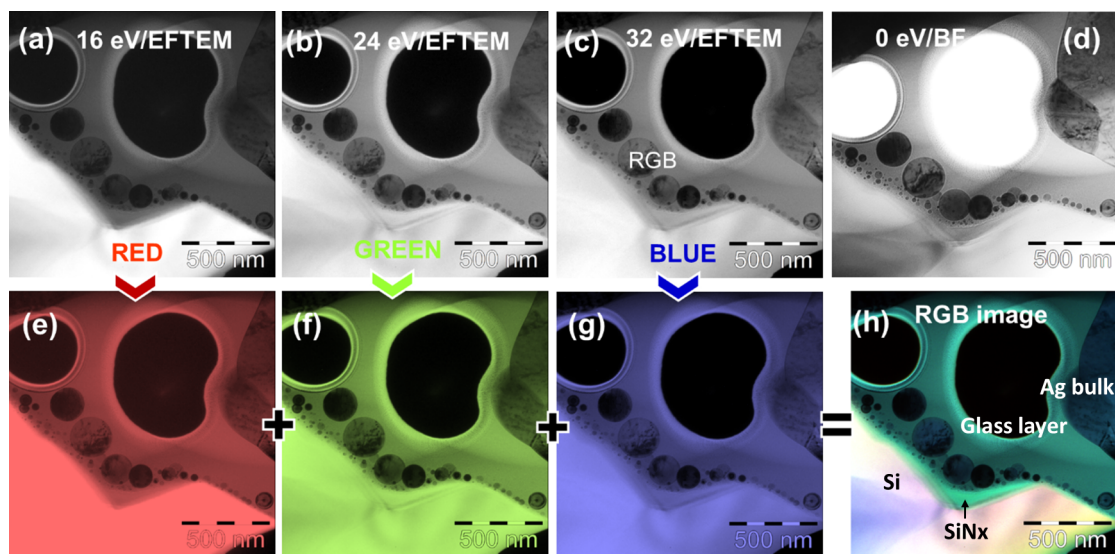
Figure 2.7: Low-magnification EF-TEM images of the glass layer of high-efficiency n-type cell. (a) 16 eV, Si plasmon peak, (b) 24 eV (SiO_2 plasmon peak, Ag plasmon peak, $Pb - O_{45}$ edge), and (c) 32 eV (Si second plasmon peak). (d-f) show the corresponding color according to their energy losses.

RGB imaging was performed by acquiring three EF-TEM images at energy losses of 16 eV (Si plasmon peak), 24 eV (SiO_2 plasmon peak, Ag plasmon peak, $Pb-O_{45}$ edge) and 32 eV (2nd Si plasmon peak), with an energy slit aperture of 5 eV width. Then, the three EF-TEM images were superimposed by assigning a false color to each of the EF-TEM images as 16 eV (Red), 24eV (Green), and 32 eV (Blue) to yield a superimposed EF-TEM or RGB image [59]. Different phases such as Si emitter, glass layer, SiN_X layer and Ag colloids/precipitates are identified at the Si/metallization interface. However, there are some disadvantages of the EF-TEM technique: (i) specimen drift, (ii) multiple scattering in the thick samples, (ii) poor lateral resolution at high magnifications and (iv) low signal to background ratio for high energy losses [30, 39].

2.7 Sample preparation and microstructural characterization by SEM/TEM

2.7.1 Strategy and experimental implementation

The various electron microscopy methods were applied in order to investigate the solar cells and will be given in this section. The specimen preparation techniques for SEM and TEM will be described

in the next sections. Figure 2.8 is a schematic diagram describing the strategy used for the micro and nano-structural analysis of solar cells.
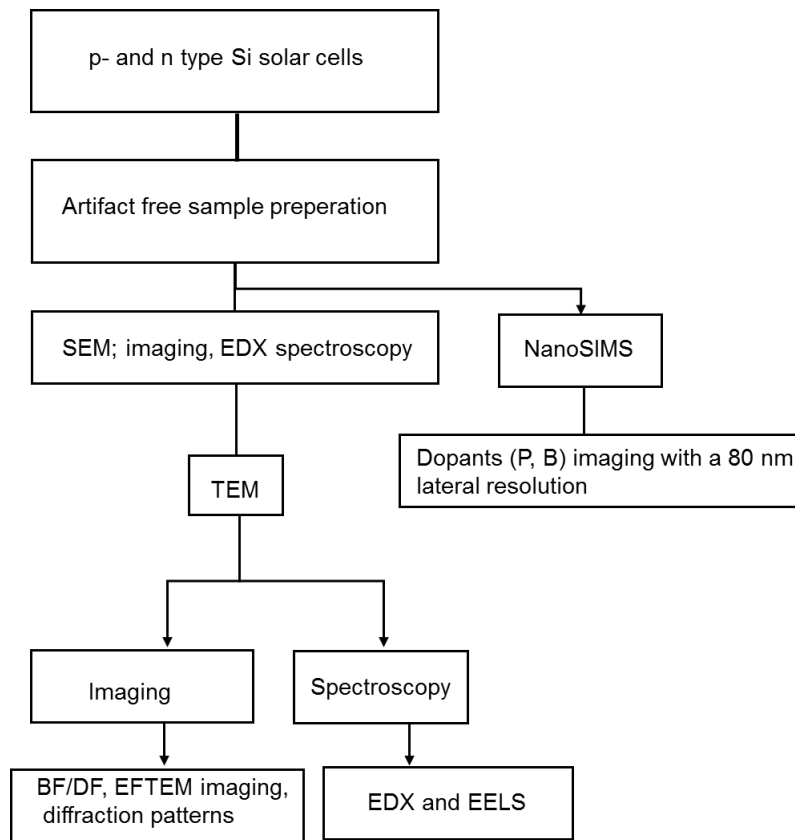

Figure 2.8: Schematic diagram showing the strategy used for the microstructure analysis of solar cells.

SEM-EDX plays a major role in the identification of microstructral features at micro-meter scale whereas TEM- EDX spectroscopy together with EELS are best suited for investigating the samples down to nm scale level. Furthermore, NanoSIMS was applied to image the dopant distributions at the Si/metallization interface with a 80 nm resolution.

2.7.2 SEM sample preparation for solar cells

Solar cells with two different geometries, i.e. p-type, planar and textured cells and n-type textured cells were analyzed at the University of Tubingen (see Figure 2.9). For microstructural characterization by SEM, samples were prepared in two different ways: plan view, and in cross-section to get a three dimensional microstructural and chemical distribution of the Si/metallization contact interface. Sample preparation particularly for textured cells is more challenging because of several reasons: the width of the metallization finger was 80 μm and thickness was 30 μm respectively and therefore, a careful, artifact free sample preparation is required in order to investigate the microstructural and chemical analysis of the metallization contacts. For fully covered planar cells samples were prepared in cross-sections only, for details see Figure 2.9.

The following steps were applied during the sample preparation: (i) first a 3 mm x 3 mm piece of a solar cell was cut using diamond wire saw and embedded in the epoxy resin, (ii) the sample is then mounted on a tri-pod holder and its surface was mechanically polished using diamond foils with

grain size from 3–1 μm, (iii) followed by ultrasonic cleaning in ethanol bath for 5 minutes and (iv) finally, samples were ion etched to get clean surfaces for microstructural and chemical analysis with 1 kV Ar^+ ions in an ion milling machine, at an angle of $10°$ for 10 minutes.
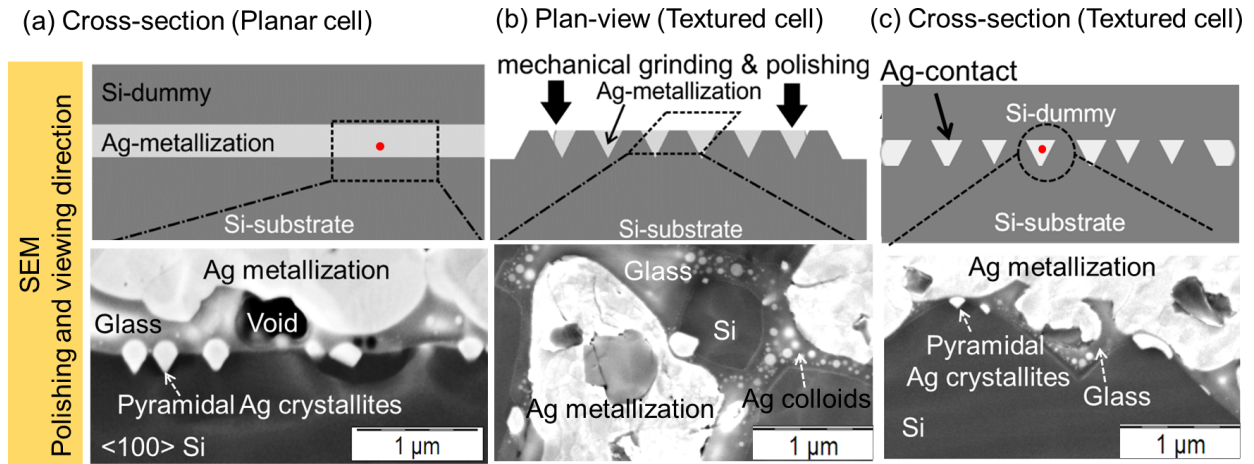

Figure 2.9: Planar as well as textured cells preparation methodology is shown here. Note that planar cells were prepared in cross-sections whereas textured cells were prepared both in plan-view and cross-sections.

Note: Plan-view samples were prepared, first by polishing the front side metallization contacts until the surface fraction covered by the polished Si pyramids and metallization yielded 50%. For monitoring the fractions of Si/Ag we used the light microscope [60]. Cross-section samples were prepared either by just breaking the sample to avoid artifacts and contamination coming from preparation technique or by polishing (Figure 2.10). For polished cross-sections, another polished Si piece as a dummy was glued on top of the polished Ag contact to protect the surface and the interface from contamination and mechanical damage during the polishing (Figure 2.10). To investigate the Si/metallization interface, in particular, the glass layer which is formed between the Si emitter and the Ag bulk of the metallization, the following steps were implemented: (i) mechanical grinding and polishing, (ii) ion-beam etching of the surface and (iii) scanning electron microscopy (SEM) analysis atleast 40k magnifications [60].
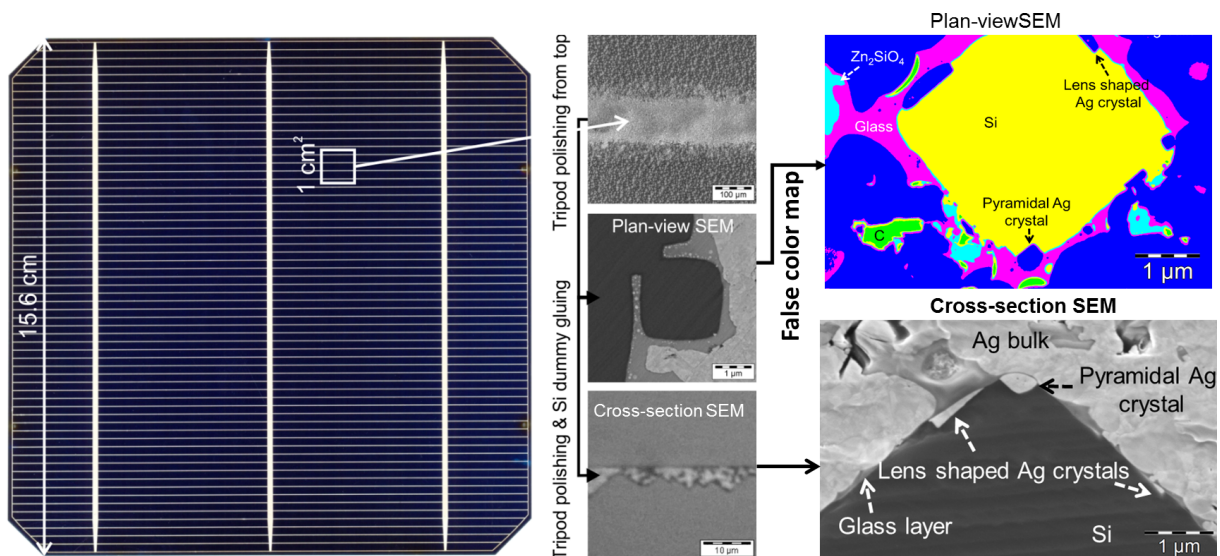
Figure 2.10: Sample preparation methodology for SEM in plan-view and cross-sections.

All samples were analyzed using a Jeol 6500F SEM (Figure 2.11) equipped with an Oxford Pentafet energy-dispersive X-ray (EDX) detector. An electron energy of 5 keV was chosen to keep the lateral resolution in both backscattered electron images (BSEI) and EDX spectra as small as possible.

Additionally, all X-ray lines being present could still be excited. Color-coded BSE images were prepared by image processing. In BSE images the gray values of each phase depend on its mean atomic number, i.e., it was possible to assign to each phase a different color [26, 60]. High-resolution secondary electron images (HR-SEI) were used to image nano-particles at the Si-metallization interface (see Figure 2.9b).

For quantitative chemical analysis of solar cells especially for the lighter and dopant elements we used 5 keV accelerating voltage to keep the lateral resolution and the relevant characteristic lines as shown in Table 2.6.

Figure 2.11: Micrograph of the SEM used in this thesis.

Element	X-ray line	Line energy [keV]
O	$K_{\alpha 1}$	0.524
Si	$K_{\alpha 1}$	1.73
Ag	$L_{\alpha 1}$	2.98
Zn	$L_{\alpha 1}$	1.01
Al	$K_{\alpha 1}$	1.48
P	$K_{\alpha 1}$	2.01
B	$K_{\alpha 1}$	0.183
N	$K_{\alpha 1}$	0.393
Pb	$M_{\alpha 1}$	2.34

Table 2.6: Characteristic X-ray lines used for SEM-EDX quantification and point EDX measurements.

2.7.3   TEM sample preparation

For solar cell TEM samples similar method was applied as used in the above section for the SEM . The only difference is, for TEM we need thin samples thinner than <50 nm to make it transparent to the electron beam. For plan-view solar cell samples, we first mechanically thinned the sample to about 20 μm thickness from the substrate side using diamond foils of different grain size between 30 μm to 1 μm. Further thinning of the sample down to less than 100 nm thicknesses is achieved by ion etching machine. Details description of sample preperation are given in Figure 2.12 and 2.13.

Note: The front side metallization was grinded with a tripod holder on diamond lapping films. This procedure allows adjusting the grinding plane to the surface of the solar cell. After this grinding plan-view samples were grinded and polished from the back side (substrate side) to about 15 μm mounted on an Al ring and then ion etched to electron transparency. The Ar^+ ions had an energy of 3 keV and an angle of 12° and a source current of 3 mA. The plan view prepared sample contained one finger at which a hole was generated after ion milling process. The electron transparent areas extended over the width of the finger, which were about 70–100 μm.
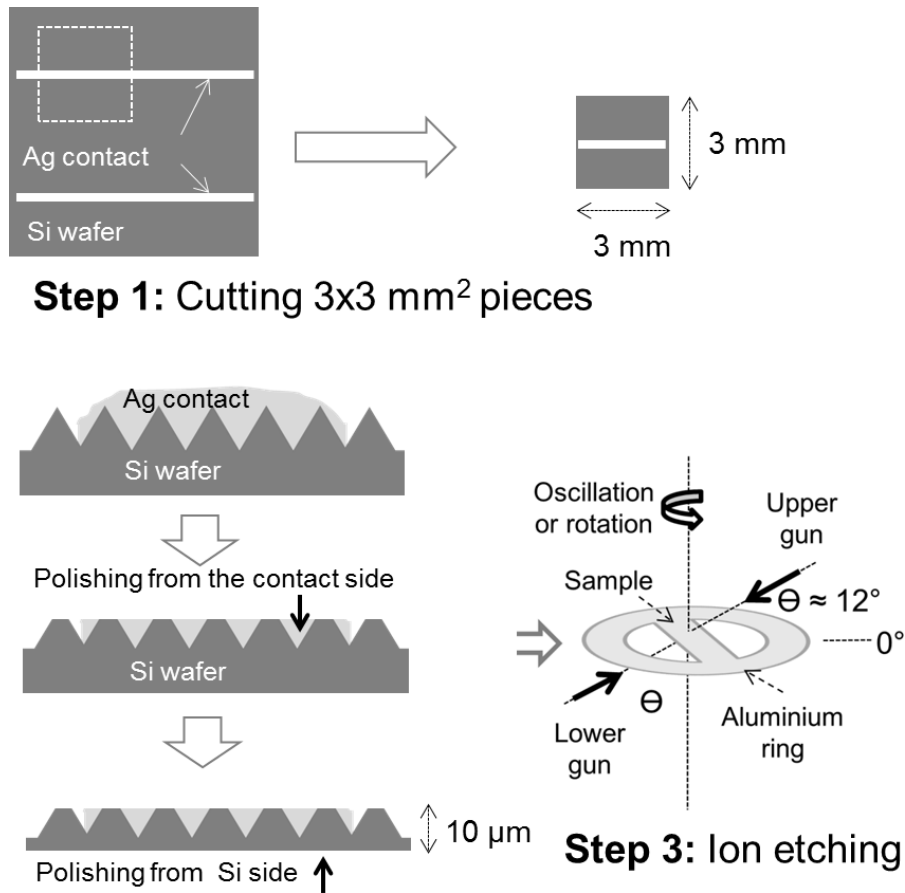
Figure 2.12: Sample preparation methodology used for the solar cell investigation.

At the beginning of the sample preparation, the cross-section samples had an additional gluing step in which a glass dummy was glued to the front side of the solar cell. The sample was then grinded and polished on a tripod polisher and the polished edge was placed parallel to a contact finger of the cell. The polishing was controlled by a light microscope by looking through the glass dummy on the surface of the cell. When the polished edge hits the contact finger, the process of polishing

was stopped and the cross section sample was grinded from the other side to 15–20 μm thickness. After this, the sample was mounted on an Al ring and ion etched with the same conditions as the plan-view sample.
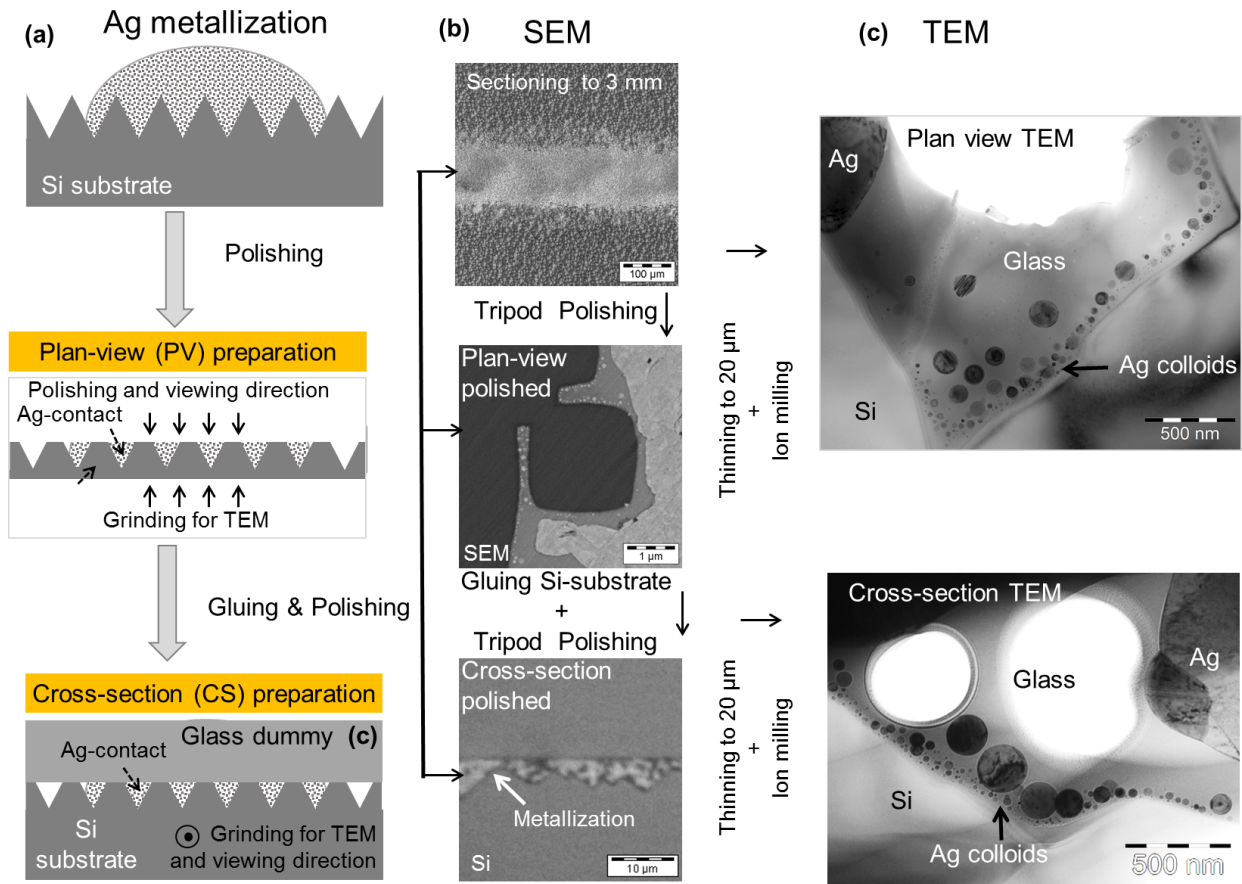

Figure 2.13: Methodology and characterization technique used for the solar cell.

2.8 How structure-property correlation works?

The microstructure and chemical composition of a material strongly affect its macroscopic physical properties and is referred to as structure-property correlation. An example of the structure-property correlation of solar cells is illustrated in Figure 2.14. The electrical property of solar cells such as contact resistance is linked with its microstructural features at the Si/metallization interface.

The microstructre at the interface is very sensitive to the processing conditions, the paste used and the Si surface orientation. Therefore, cells with outstanding contact and series resistances were selected for the microstructural analysis. In a next step, the microstructural features at the Si/metallization interface could be identified i.e, low contact resistance cells showed a high density of Ag colloids in the glass layer while a small density of Ag colloid was found for cells with a high contact resistance and a low efficiency. The correlation between the microstructural and electrical properties of the cell yields a sound structure-property for solar cells. In the next chapters, structure property correlation has been explained for high-efficiency p- and n-type solar cells.
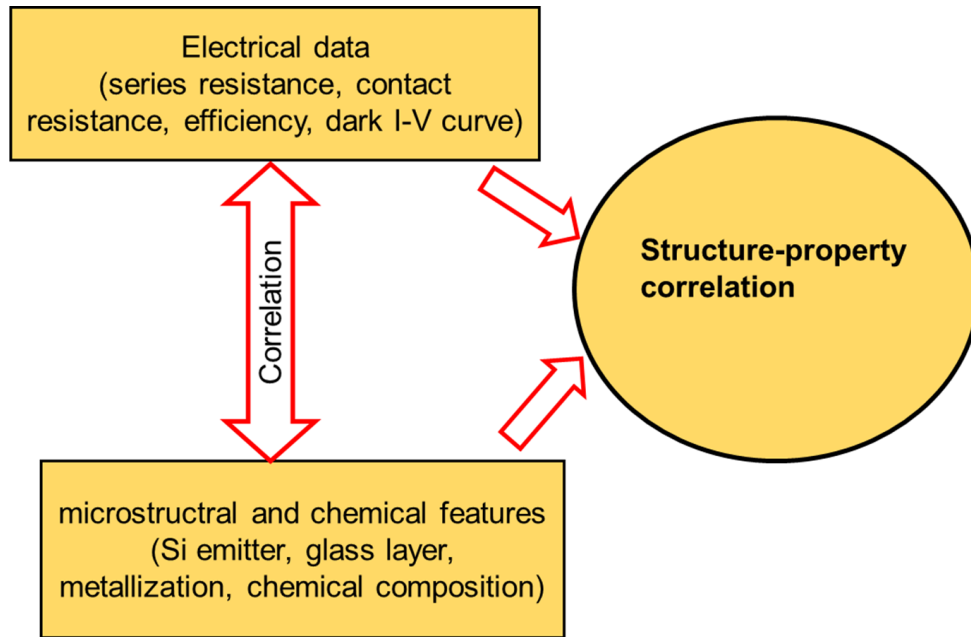
Figure 2.14: Structure-property correlation of Si solar cells.

2.9 Electrical measurements on small cells

p-type and n-type cells were processed identically and contacted with different front side metallization pastes. The most significant difference between the cells was the contact resistance, since different pastes were applied. The design of the metallization was such, that the finger and busbar resistances were expected to be smaller than the contact resistance. Therefore, the essential parameter affecting the series resistance was the contact resistance of the front side metallization. If these assumptions hold true, then the temperature-dependent measurements of the series resistance would yield an indirect way to asses the temperature-dependent of the contact resistance. Such analysis are important for determining the dominating current path across the Si/metallization interface.

A temperature-dependent electrical characterization on small cells has been introduced that bridges the gap between the microstructural analysis and the electrical measurements of the large cells measured at room temperature (RT). Within this work, small cells ($1 \times 1 cm^2$) were cut out from the large wafers and the temperature dependent dark current I-V curves were acquired between 80 K and RT, in an optical cryostat. The special features of the cryostat are built-in transparent glass windows that allowed for optical experiments on the analyzed samples. The cryostat is designed for continuously cooling with liquid nitrogen (LN_2) and the setup is shown in Figure 2.15.

The temperature dependence of the series resistance R_S was determined by fitting the dark I–V curve with the two diode model equation [61, 62, 63]. A detailed description of the temperature dependent dark I-V measurements is described in Refs. [61, 62, 63].

The current distribution in dark measurements is the one that most sensitively probes the area under the contact and, therefore, this method is particularly useful for understanding of the metallization related losses, especially R_S that provide insights of the underlying current path in the front side metallization.

Optical Cryostat
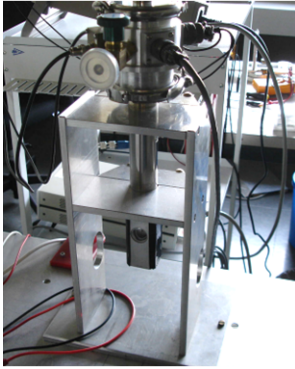
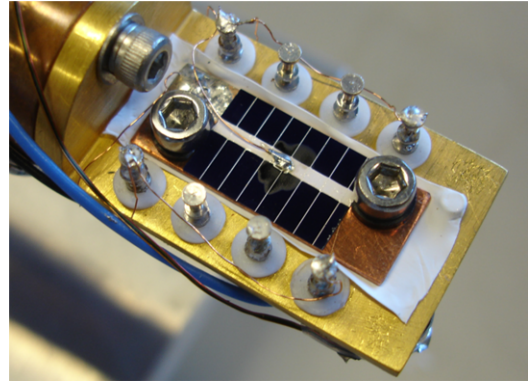**Cryostat window**

Cell mounted on the cold finger

Figure 2.15: Temperature dependent electrical characterization set up for small sized solar cells.

Part III

Structure-property correlation of high-efficiency, single-crystalline, p- and n-type Si solar cells

Chapter 3

Contact Formation of Front Side Metallization in p-type, Single Crystalline Si Solar Cells: microstructure, temperature dependent series resistance and percolation model [26]

3.1 Background

For the past 30 years, considerable efforts have been made to improve the contact formation on front side silver (Ag) thick film contacts in single-crystalline silicon (Si) solar cells with n-type emitters. Screen printing is the most relevant contacting technology, due to its simplicity, cost effectiveness and high throughput [64].

Pastes used for front side metallization typically consist of glass frits, Ag powder, organic binders, and metal oxides. Altogether more than 10 different elements are contained in a paste and it is chemically very complex. The contact formation has been reviewed by Horteis et al. [64] considering electrical properties and conduction mechanisms, microstructural features of the contact and proposing chemical reactions for the contact formation that occur during the high-temperature annealing.

For contacts prepared by screen printing technology, the contact resistance is typically in the range of a few $m\Omega\,cm^2$. Such contacts do not significantly degrade the efficiency of the cell, since the series resistance remains still acceptably low. Therefore, preparing optimal contacts by screen printing has turned out to be a key for providing cost-efficient, high-efficiency solar cells. In contrast, contacts that are prepared with more advanced technologies yield a contact resistance of 10^{-5} $\Omega\,cm^2$ for the same substrate [65]. Screen printed front side contacts exhibit a complex Si/Ag interface [22, 24]. At this contact interface, Ag nanocrystals penetrate the Si emitter. Typically, a glass layer with thicknesses varying from few nms up to several hundred nanometers that contains highly conductive Ag nanocolloids.

The metal−semiconductor contact interface has attracted scientific interest over decades, starting before Bardeen´s paper was published in 1947 and ending today with still many unsolved questions around [14]. Fundamental basics of the metal contact relevant for solar cells are given in Refs. [16, 17, 18]. The correct understanding of Schottky barriers at metal−semiconductor interfaces took decades and the role of the atomic structure at the interface determining the Schottky barrier height (SBH) was realized by Tung [15, 66]. It turned out that the orientation of the Si substrate plays a key role for the SBH of epitaxially deposited silicide films.

For solar cells screen printing technology, it was realized late and only recently that the structure of the contact (strongly) influences its electrical properties. The paper of Ballif et al. [24] received the widest attention (cited 130 times) and is still the most frequently cited reference on this topic. Both papers the paper of Tung for epitaxially grown silicides on Si and the paper of Ballif et al. for

screen printed solar cells stress the importance of the microstructure for the electrical properties of the metal−semiconductor contacts [15, 24]. The paper of Ballif et al. showed microstructure of the contact down to the nm scale (by TEM). Therefore, this paper added considerable insight also for a better understanding of the electrical properties of the contact. The main question for understanding contact resistances was: where does the current flow? The essential result of Ballif et al. was that Ag nanocrystals are present at the Si surface and that authors measured a very low contact resistance of 10^{-7} Ω cm^2 for such nanocrystals to the emitter by conductive AFM [24]. It was then concluded that the current path would go only over such nanocrystals, preferably via direct connections to the bulk Ag. If direct connections would not be available then a "tunneling" through the glass layer was proposed. The glass layer was assumed to be insulating with a specific resistance of 10^9 Ω cm [24]. It is well known, however, that in oxides electrical conductivity is determined by oxygen vacancies and doping and that this assumption, therefore, is not applicable without considering the details. It is worth noting that Ballif et al. investigated (i) planar <100> Si surfaces and (ii) that they did not measure the contact resistance of that sample for which microstructural analysis was carried out. Rather they pointed out that contact resistance usually is in the range of mΩ cm^2. We will show in this paper that the results of Ballif can easily be understood in a misleading way if the (i) orientation of the substrate was not considered and, (ii) if the contact resistance was not measured explicitly. Indeed the number of papers that combine contact resistance measurements with microstructural analysis are very few.

A number of papers were published on the topic of solar cell metallization: where does the current flow? by Kontermann and Willeke and by Pysch and Glunz [67, 68]. Kontermann and Willeke obtained microscopic $I-V$ measurements on individual Ag crystals on <100> Si and claimed contact resistances of 3 mΩ cm^2, measured by TLM [67].

The applied method of microscopic $I-V$ measurements is technically complicated, can only be performed on a very small number of samples and, therefore, is not widely spread. In contrast, Pysch et al. identified the role of the Si substrate orientation for forming different types of Ag nanocrystals and referred to a paper of Khadilkar et al. [68, 69]. However, this important message was not received with the necessary attention by the community. It is this paper by Pysch et al. that is the right starting point for understanding the results presented here. Pysch et al. applied standard methods: (i) contact resistance measurements by TLM together with microstructural analysis and (ii) recognized the influence of the Si surface on the microstructure of the Ag nanocrystals to a first extent [68]. The main target of this paper was, however, the silver plating on a seed layer and not the screen printed contact itself. Therefore, still major questions remained to be solved for the screen printing: (i) what is the influence of the paste, (ii) what is the influence of the Si orientation on the contact resistance, and (iii) where does the current flow?

In summary, two models were reported in the literature to explain the contact resistance: model I assumes that Ag crystals penetrating the Si surface represent the dominating current path, especially if they are directly connected to the Ag bulk [22, 24, 68]. Model II assumes that the current flows through the glass layer by Ag nanocolloids assisted tunneling [25, 70], since the resistivity of the glass layer is assumed to be significantly lower with Ag nanocolloids present in the glass phase. In addition, Lin et. al suggest that the Ag colloids in the glass phase are more favorable than a few Ag crystals and play a vital role for the transport through the glass layer at the Si/Ag interface [71].

The orientation of the Si substrate was investigated in the literature [69, 72, 73, 74, 75] and affects the shape of Ag nanocrystals, however, no explanation with respect to the electrical properties was given in these publications. Cabrera et al. observed a high contact resistance on planar <100> Si as compared to textured Si having (111) faces, the results were discussed in more detail in [62, 73]. The existence of two models rather than one for the current path as explained above comes from the two very different Si metal interface structures of <100> and <111> oriented Si: primarily <100> planar contacts were studied, textured cells have <111> oriented surfaces yielding a different microstructure and also electrical properties. However, the differences in structural and electrical properties of planar and textured contacts have not been fully realized. Since these two contact types yield very different microstructures, as will be shown here, two models are necessary, one for <100> planar, the other for textured cells which are mostly related to <111> planar. Also the term "tunneling through the glass layer" has been used in a misleading way together with the assumption that the glass layer was insulating [24].

The influence of paste composition, firing process and the role of the gas atmosphere on the specific contact resistance were studied [22, 64, 76, 77, 78, 79, 80]. However, a detailed investigation of Ag nanocrystals formation on differently oriented Si substrates (planar <100> and <111>) and its correlation to macroscopic electrical properties particularly the series and contact resistances has not been systematically carried out yet.

A large number of planar and textured cells were produced [59, 60, 62], their electrical properties, series and contact resistance, in particular, were measured. Among these cells, few of them were selected for microstructural analysis in order to investigate the effect of the surface orientation and the paste properties on the contact resistance, because microstructural analyses require a substantial effort. The following important findings could be made: (i) the crystallographic orientation of the Si substrate and (ii) the wetting behavior of pastes strongly affect the contact microstructure and determine the contact resistance.

The objective of the experimental work summarized here was to investigate the contact formation mechanism and the potential current paths from the Si emitter to the Ag bulk. For this processing of the cells was identical for all textured cells, only the front side metallization differed, an analogous procedure was used for planar cells. For investigating the orientation dependence planar cells with <100> and <111> Si orientation were processed and correlate the shape of Ag nanocrystals to the measured contact resistance [60]. Anisotropy of surface properties in Si are well established: (111) planes of Si are closed packed, and yield a small surface as well as interface energy as compared to other crystallographic planes i.e. (100). Cheek et al. reported that (111) oriented Si oxidizes three times faster as compared to (100) oriented Si [81]. Also, they pointed out that the <111> Si has lower contact resistance than <100> Si.

For investigating the effect of the paste and in particular its wetting behavior, the microstructure of the contact region was investigated by scanning electron microscopy (SEM) and transmission electron (TEM) microscopy [59, 60]. In addition, energy dispersive X-ray (EDX) microanalysis was carried out both in the SEM and TEM to analyze the phases formed during the contact formation. The poor detection limit of the EDX analysis fails to yield doping and impurity concentrations in the emitter and in the space charge region of Si. To compensate for these shortcomings the temperature dependent $I-V$ measurements provide a complementary view to the findings of the microstructure

analysis and yield a more detailed understanding of the electrical properties. Microstructural analysis of solar cells alone is not sufficient to correlate directly with their electrical properties, particularly series and contact resistance. *Paste and orientation dependent effects have to be identified in electrical <u>and</u> microstructural investigations, then yielding a structure-property correlation.*

Therefore, a combination of microstructural analysis together with detailed temperature dependent $I-V$ measurements were carried out in this work. Note that such temperature dependent $I-V$ measurements yields the temperature dependent series resistance and from this the temperature dependent contact resistance. If transport through the glass would be relevant then a semiconducting contact resistance should be observed. With this approach a clear understanding of a structure-property correlation between microstructural and electrical data is then established. Results of the microstructural characterization were converted into a percolation model to explain the role of Ag colloids in the glass layer of such cells.

3.2 Experimental details

Planar cells were processed on FZ grown p-type Si wafers, whereas textured cells were realized on Cz grown p-type Si wafers. Details of solar cells emitter processing and metallization parameters (i.e. firing temperature) are described in Refs. [59, 60, 82]. The cells were identically processed except for the screen printing paste. The metallization was realized by a screen printing technology, and four different pastes referred to as FSP1, FSP2, FSP3 and FSP0 were used to contact the Si emitters. Paste FSP2 and FSP3 have a similar chemical composition with paste FSP3 being a newer batch of paste FSP2.

For the microstructural characterization, planar cells were prepared only in cross-section and textured cells were prepared and investigated in plan-view and in cross-sections. The Si/Ag interface was examined using a Jeol 6500F scanning electron microscope (SEM) equipped with an Oxford Pentafet energy-dispersive X-ray (EDX) detector. An electron energy of 5 keV was chosen to keep the lateral resolution as small as possible for the microanalysis. Low magnification backscattered electron images were acquired to identify the different phases and wetting behavior of the paste. High-resolution scanning electron microscopy (HR-SEM), magnifications of 20-50 k, was used to image the metallic nanocolloids at the Si/Ag interface.

Electrical properties of the large cells (i.e. illuminated $I-V$ curves) were measured with an industrial solar cell tester under flash illumination based on the spectrum AM1.5G IEC60904-3Ed.2 (2008) [59]. In addition, the specific contact resistance measurements were carried out at Fraunhofer ISE in Freiburg by applying the transmission line (TLM) method on small strips of a solar cell at room temperature (RT). Temperature dependent dark $I-V$ and series resistance measurements were obtained on small sized cells and the same cells were used for microstructural investigations.

3.3 Results

3.3.1 Electrical properties

3.3.1.1 Large cells

Planar cells are denoted as # P1, # P2, # P3, # P4 and # P5, whereas textured cells are indicated by # T1, # T2 and # T3, respectively. Table 1 summarizes the processing parameters and electrical properties

of the investigated cells. Planar cells # P1, # P3 and # P5 were processed on <100> oriented FZ grown Si wafers and contacted with front side metallization pastes FSP1, FSP3 and FSP0, respectively. Cell # P2 and # P4 were processed on FZ grown <111> oriented Si surfaces and contacted with front side metallization pastes FSP3 and FSP0, respectively. Cell # P2 and # P4 with <111> oriented Si revealed the lowest contact resistance (1.8–4.9 mΩ cm^2) and the highest efficiencies of 17.2 % among all the planar cells.

Solar Cells		Substrate	Paste	T_{FFO} [°C]	η [%]	R_S [$\Omega.cm^2$]	R_P [$\Omega.cm^2$]	ρ_c [m$\Omega.cm^2$]	FF [%]
	# P1	FZ-Si<100>	FSP1	930	7.8	–	–	33	42.1
	# P2	FZ-Si<111>	FSP3	930	17.1	–	–	4.9	81.3
Planar	# P3	FZ-Si<100>	FSP3	930	16.1	–	–	11.2	78.1
	# P4	FZ-Si<111>	FSP0	930	17.2	–	–	1.8	81.5
	# P5	FZ-Si<100>	FSP0	930	10.5	–	–	38	53.7
	# T1	Cz-Si<100>	FSP2	900	18.0	0.61	32123	5	79.1
Textured	# T2	Cz-Si<100>	FSP1	900	16.9	0.87	4495	21	77.1
	# T3	Cz-Si<100>	FSP1	960	13.6	3.91	4451	131	61.8

Table 3.1: Process parameters and results of the electrical measurements (i.e. firing temperature T_{FFO}, efficiency η, and specific contact resistance ρ_c) obtained on planar and textured solar cells. Pronounced differences appear in the specific contact resistance and efficiency of the Si solar cells are attributed to: (i) the crystallographic orientation of the Si wafers, (ii) the applied front side paste and (iii) the peak firing temperature.

All textured cells were processed on Cz grown <100> Si wafers. Cells (# T2 and # T3) were contacted with the same front side metallization paste FSP1, whereas cell # T1 was contacted with front side metallization paste FSP2 which yielded the smallest contact resistance of 5 mΩ cm^2.

Planar and textured cells were optimally fired at their corresponding set temperatures (930 °C and 900 °C). Cell # T3 was slightly overfired at set peak point of 960 °C and yielded a significantly higher contact resistance (131 mΩ cm^2) and a low efficiency (13.1 %). Figure 3.1 shows the specific contact resistance (ρ_c) measurements obtained on planar (<100> and <111>) and textured cells contacted with different front side pastes. The bars indicate the scatter of data found within each batch of the individual cells [60].

Planar <111> oriented Si cells show unprecedented low contact resistances as compared to planar <100> Si when contacted with pastes FSP3 and FSP0, even smaller than the contact resistance of textured cells. Typical values of the contact resistance at RT for planar <111> oriented Si cells were less than 5 mΩ cm^2, whereas for planar <100> orientation it was beyond >10 mΩ cm^2. To our knowledge, these are the first results of high-efficiency solar cells proving the large anisotropy of the Si surface with respect to the contact resistance. Also, such a high-quality Ag metallization yielding low contact resistance on the planar <111> Si surfaces has not been reported before in the literature. In addition, cells (planar and textured) contacted with paste FSP1 yielded significantly higher contact resistance as compared to the cells contacted with pastes FSP3 and FSP0 [59, 60].

In summary, within one set of cells produced with one particular paste the sequence of contact resistance is still maintained: textured and <111> oriented planar surfaces have a lower contact resistance than <100> oriented planar surfaces.
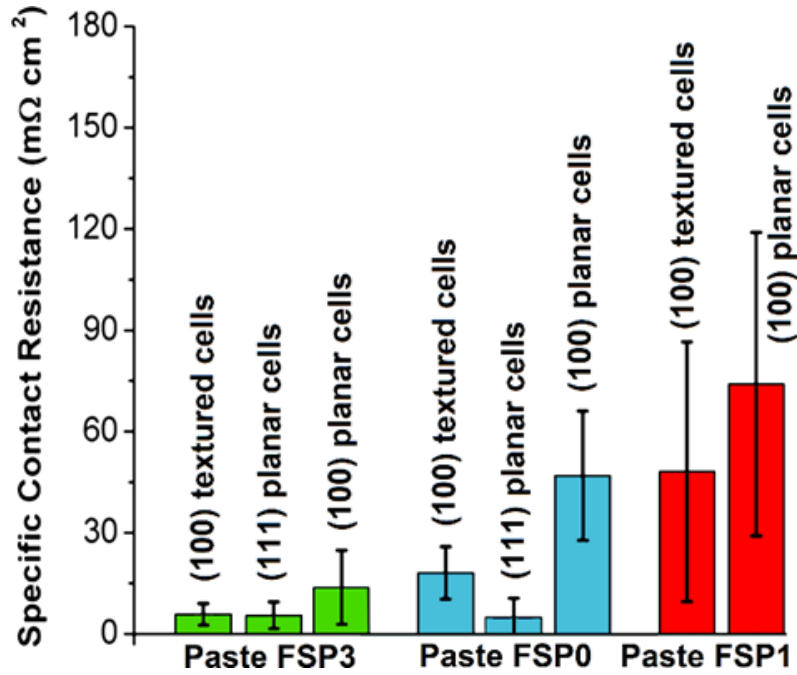
Figure 3.1: Specific contact resistance measurements (TLM) of the planar and textured cells, with <100> and <111> oriented Si substrates, contacted with different pastes (FSP0, FSP1 and FSP3) were investigated in this work. <111> planar Si surfaces show a remarkably low contact resistance as compared to <100> oriented Si.

3.3.1.2 Small sized planar cells

In general, the temperature dependent series resistance (R_S) of different cells correlated with the contact resistance of the same cells measured at RT. The series resistance was significantly larger for cell # P1, 2918 mΩ at RT, grown on <100> planar Si and contacted with paste FSP1, as compared to cell # P2, 123 mΩ, grown on <111> planar Si and contacted with paste FSP3 (Figure 3.2a). For both cells, the series resistance yielded a semiconducting temperature behavior. The series resistance was determined from $I-V$ curves (Figure 3.2c and d) using the large current integration method [10]. Investigations on additional planar cells confirm that the contact resistance depends primarily on the orientation of the Si surface [62].

3.3.1.3 Small sized textured cells

Fig. 2b shows the temperature dependent series resistance data obtained from the textured cells # T1, # T2 and # T3 respectively. For cell # T1, series resistance was about 15 mΩ at 80 K and 35 mΩ at RT. Cell # T2 yielded R_S of 46 mΩ at RT which was in the same range as for cell # T1. In contrast, the series resistance of cell # T2 at 80 K, about 67 mΩ, was significantly larger than for the cell # T1. Both cells revealed a clearly different temperature dependence; for cell # T1, R_S yielded a weak metallic behavior, whereas cell # T2 yielded a semiconducting series resistance. The series resistance of the overfired cell # T3, processed with paste FSP1, displayed a temperature dependence similar to that of the optimally fired cell # T2, however, the absolute values measured at RT and 80 K were significantly larger than for cell # T2.
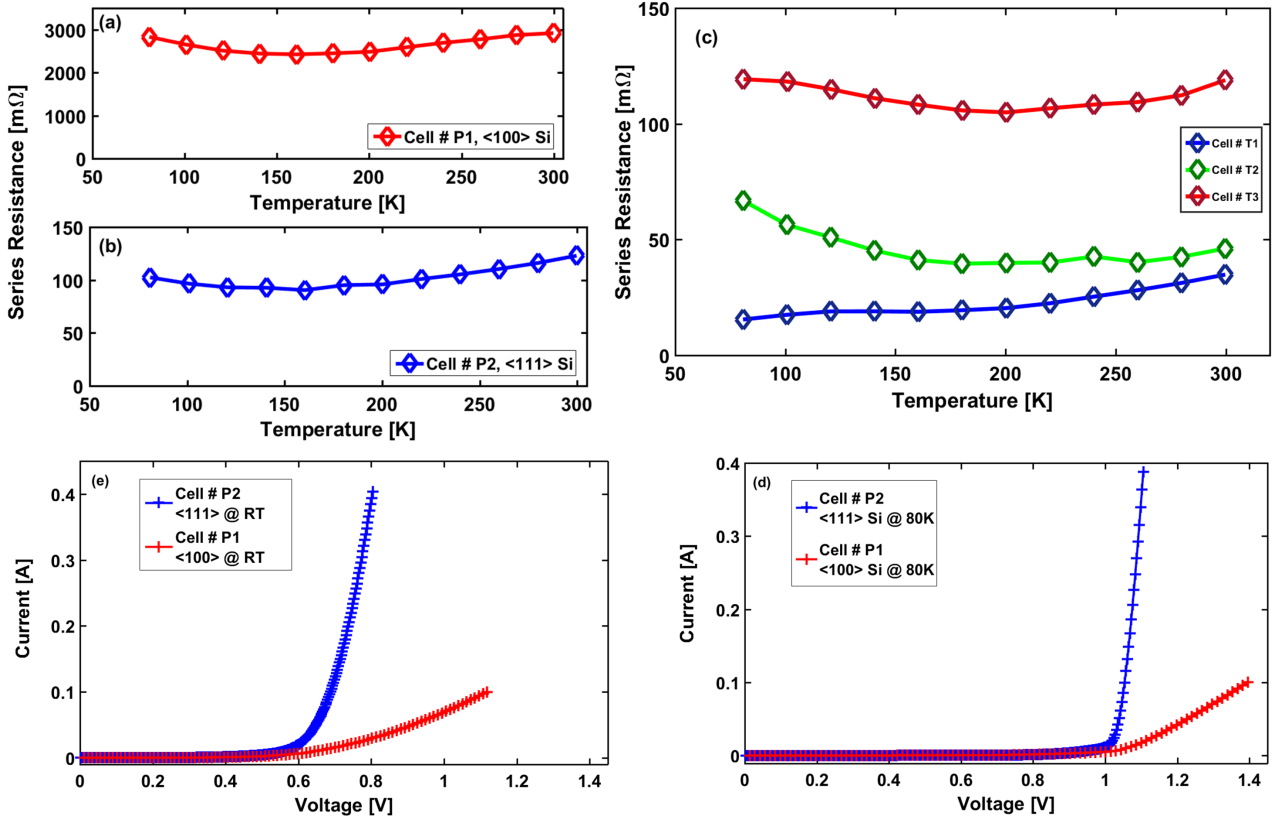
Figure 3.2: (a, b) Temperature dependent series resistance measurements obtained on the planar cells # P1 (<100> oriented, FSP1) and # P2 (<111> oriented, FSP3). (d–e) Corresponding dark current I–V curves measured at 80 K and RT. (c) the temperature dependent series resistance measurements on the textured cells # T1, # T2 and # T3, respectively. Cells # T2 and # T3 reveal a semiconducting behavior whereas cell # T1 shows a weak metallic behavior, especially at low temperatures.

3.4 Microstructural analysis

3.4.1 Planar cells

Figure 3.3a to e show high-resolution cross sectional SEM images of the planar cells (# P1, # P2, # P3, # P4 and # P5) obtained at the Si/Ag interface. Cell # P1 (see Figure 3.3a) with <100> oriented Si revealed pyramidal shaped Ag crystals at the Si/Ag interface. The height of the pyramidal Ag crystals was measured between 70 and 150 nm with a penetration depth of about 50−125 nm into the Si emitter. On the other hand, cell # P2 with <111> oriented Si yielded lens shaped Ag crystals directly connected to the Si emitter (see Figure 3.3b). Laterally, they are bigger in size (0.5−1 μm wide) with relatively shallow penetration depths of about 20−40 nm. For cell # P2 (FSP3) with <111> oriented Si, more than 20 % of the Si/Ag interface was covered by such lens shaped Ag nanocrystals. For cell # P1 (FSP1), the coverage fraction was less than 15 %. Moreover for cell # P2 a continuous glass layer with a significant density of Ag colloids was found at the interface, whereas cell # P1 showed a discontinuous glass layer with a smaller fraction of Ag nanocolloids. Ag colloids close to the Si surface are smaller in size as compared to colloids present in the central and upper part of the glass layer.

Cells # P3 (<100> oriented, pyramidal shaped Ag), # P4 (<111> oriented, lens shaped Ag) and

P5 (<100> oriented, pyramidal shaped Ag) confirm that the crystallographic orientation of the Si surfaces determines the shape of the Ag crystals. Lens shaped Ag crystals are formed only on <111> oriented Si, whereas for <100> oriented Si the Ag crystals are pyramidal. Because of their increased lateral dimensions of $0.5-1\ \mu$m the lens shaped Ag crystals are ideal to ensure a high lateral conductivity/charge transport for such interfaces. Pyramidal Ag crystals are typically 100 nm wide.
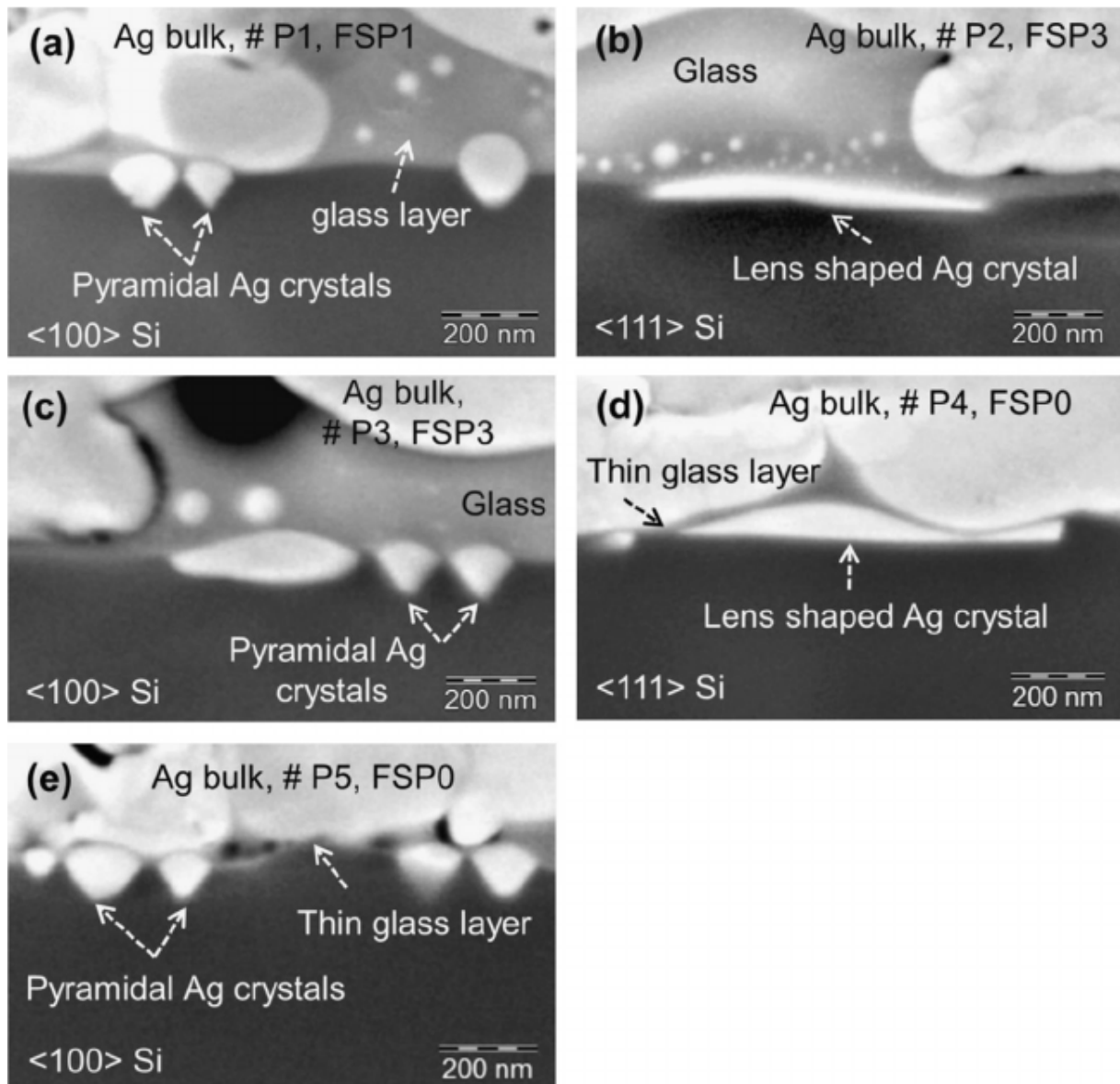
Figure 3.3: HRSEM images of planar cells obtained at the Si/Ag interface with <111> and <100> oriented Si. Figure 3.3a, c and e, cells # P1, # P3, and # P5 with <100> Si and contacted with three different pastes (FSP3, FSP0 and FSP1) showed the formation of pyramidal shaped Ag crystals onto the Si emitter. In (b) and (d) cells # P2, # P4 with <111> Si contacted with paste FSP3 and FSP0, yielded lens shaped Ag crystals directly connected to the Si emitter. For all cells an inhomogeneous glass layer (few nm to 500 nm) was found at the Si/Ag interface.

3.4.2 Textured cells

Figure 3.4a, c and e show low-magnification color coded plan-view BSE images of the textured cells # T1, # T2 and # T3 respectively, obtained at the Si/Ag interface. The corresponding high-magnification

images are shown in Figure 3.4b, d and f. This type of images yields the phase distribution according to the variation in atomic number (Z-contrast) of the specimen. The different colors could be assigned to the different phases by SEM-EDX microanalysis, i.e. Si pyramids (yellow), Ag (blue), glass phase (pink), carbon (green) and Zn-rich oxide phases (sky blue). Additional high-resolution images of the cells # T1, # T2 and # T3 are shown in Figure 3.5.
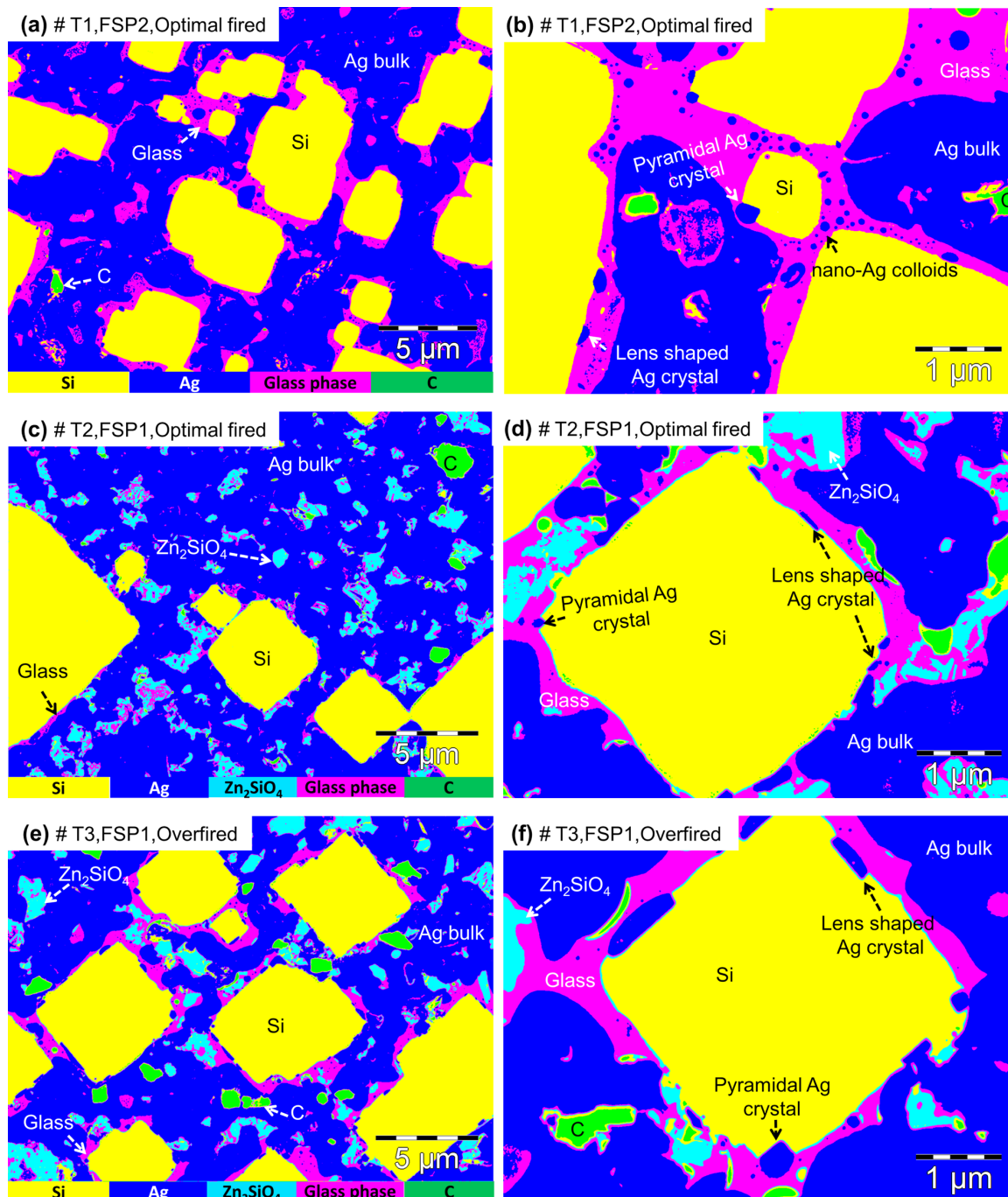
Figure 3.4: Plan-view false color BSE images obtained at the Si/Ag interface. (a) cell # T1 contacted with FSP2 paste and (b–c) cells # T2 and # T3 contacted with paste FSP1. (d–f) represent the corresponding high-magnification images of the individual cells.

For the optimally fired cell # T1 contacted with paste FSP2, the glass layer ($<10-1000$ nm) showed a continuous wetting of the Si emitter and was decorated with a considerable density of metallic Ag

nanocolloids (120 Ag colloids/μm^2). The size of Ag nanocolloids was measured between $5-200$ nm. Figure 3.4b shows different types of microstructural features appeared at the contact interface: (i) some regions were dominated by high fractions of Ag nanocolloids in the glass layer, (ii) whereas others contained pyramidal as well as lens shaped Ag crystals directly connected to the Si emitter. In accordance with the results obtained on the planar cells, pyramidal shaped Ag crystals are formed at the edges of Si pyramids, whereas lens shaped Ag crystals (see Figure 3.4b) are formed at the planar side of Si pyramids [60, 74].
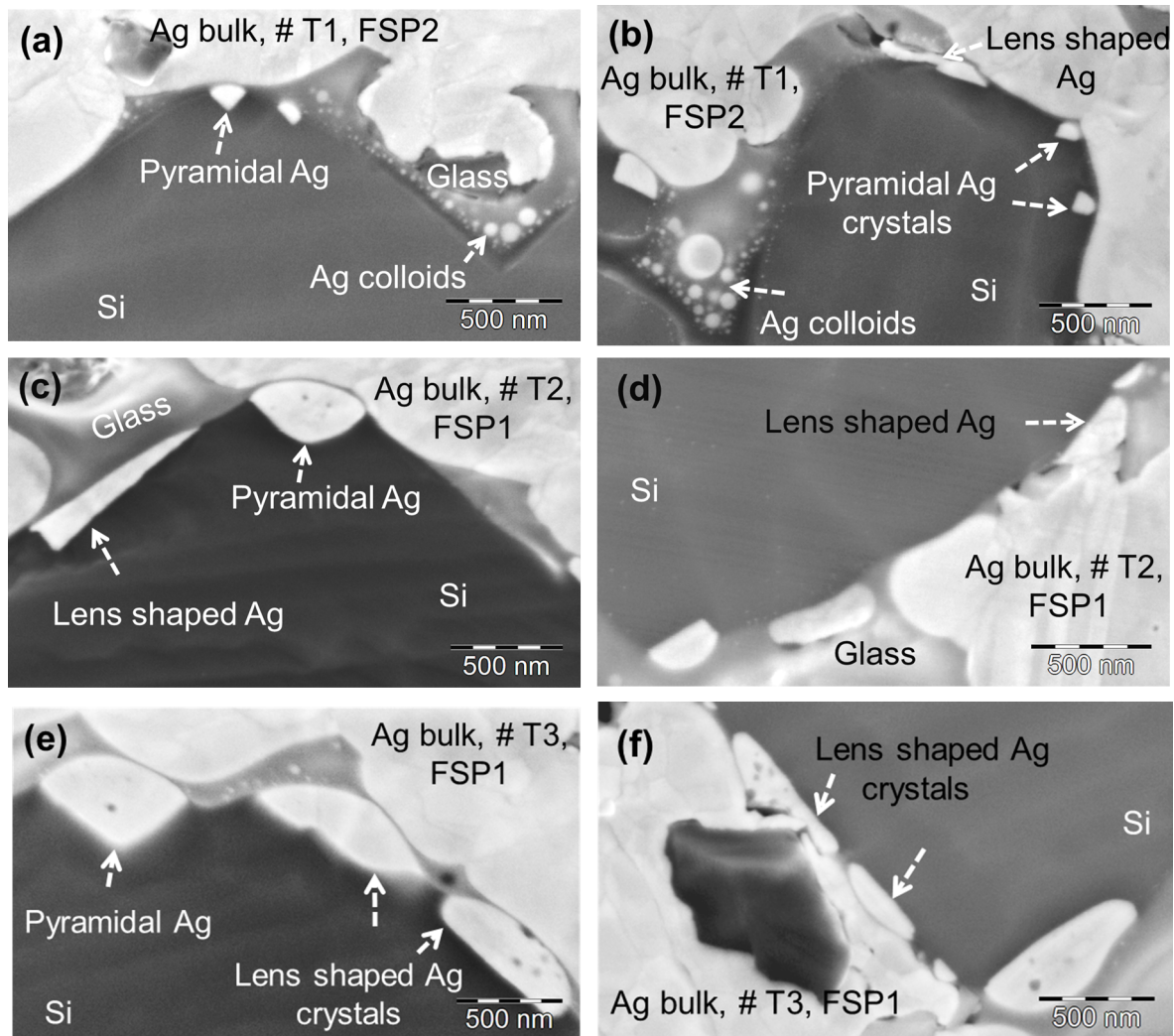
Figure 3.5: High-resolution SEM images in cross-sectional and in plan-view obtained at the Si/Ag interface for three textured cells # T1, # T2 and # T3. (a–b) optimally fired cell # T1 in cross-sectional and plan view, (c–d) optimally fired cell # T2, and (e–f) overfired cell # T3 in cross-sectional and corresponding plan-view image.

In contrast to cell # T1, optimally fired cell # T2 contacted with paste FSP1 revealed a discontinuous wetting of the glass phase at the Si surface (see Figure 3.4c), wherein Zn rich oxide phases were observed in the glass phase. The glass phase was $10-800$ nm thick and contained only a small density of metallic Ag colloids.

The pyramidal and lens shaped Ag nanocrystals were less in number and smaller in sized as compared to cell # T3. At few locations lens shaped Ag crystals are closely located to the Ag bulk contacts. Overfired cell # T3 (see Figure 3.4e) contacted with paste FSP1 also showed a discontinuous wetting

of the Si pyramids by the glass phase, similar to one as observed for cell # T2. The thickness of the glass phase was estimated between a few tens of nm to 1 μm. At the contact interface, a significant amount of Zn_2SiO_4 rich oxide phases were observed in the glass phase.

In addition, over firing yielded significant changes in the shape (distorted pyramidal/lens shaped Ag crystals) as well as on the density of the Ag nanocrystals formed at the Si emitter (see Figure 3.4f). The pyramidal Ag crystals were larger and their width varied from 300−600 nm, while their penetration depth was about 300 nm. On the other hand, lens shaped Ag crystals were bigger in size (0.5−1 μm) and penetrating 70−100 nm into the Si emitter. For cell # T3 a small density of Ag colloids was identified in the glass layer. Microstructural analyses cannot explain the difference in contact resistance between cell # T2, and # T3.

3.4.3 Chemical composition of the glass phase

The chemical composition of the glass phase of cells # T1, # T2 and # T3 was investigated by Energy Dispersive X-ray (EDX) microanalysis in SEM. The chemical composition of the glass phase showed (SiO_X)Pb, as main constitutes and Zn, Ti, Al, Ag, P and B as minor constituents with mole fractions above the detection limit of EDX [60]. Figure 3.6a to d show the SEM-EDX spectra acquired in the glass phase of cells # T1, # T2 and # T3, respectively.
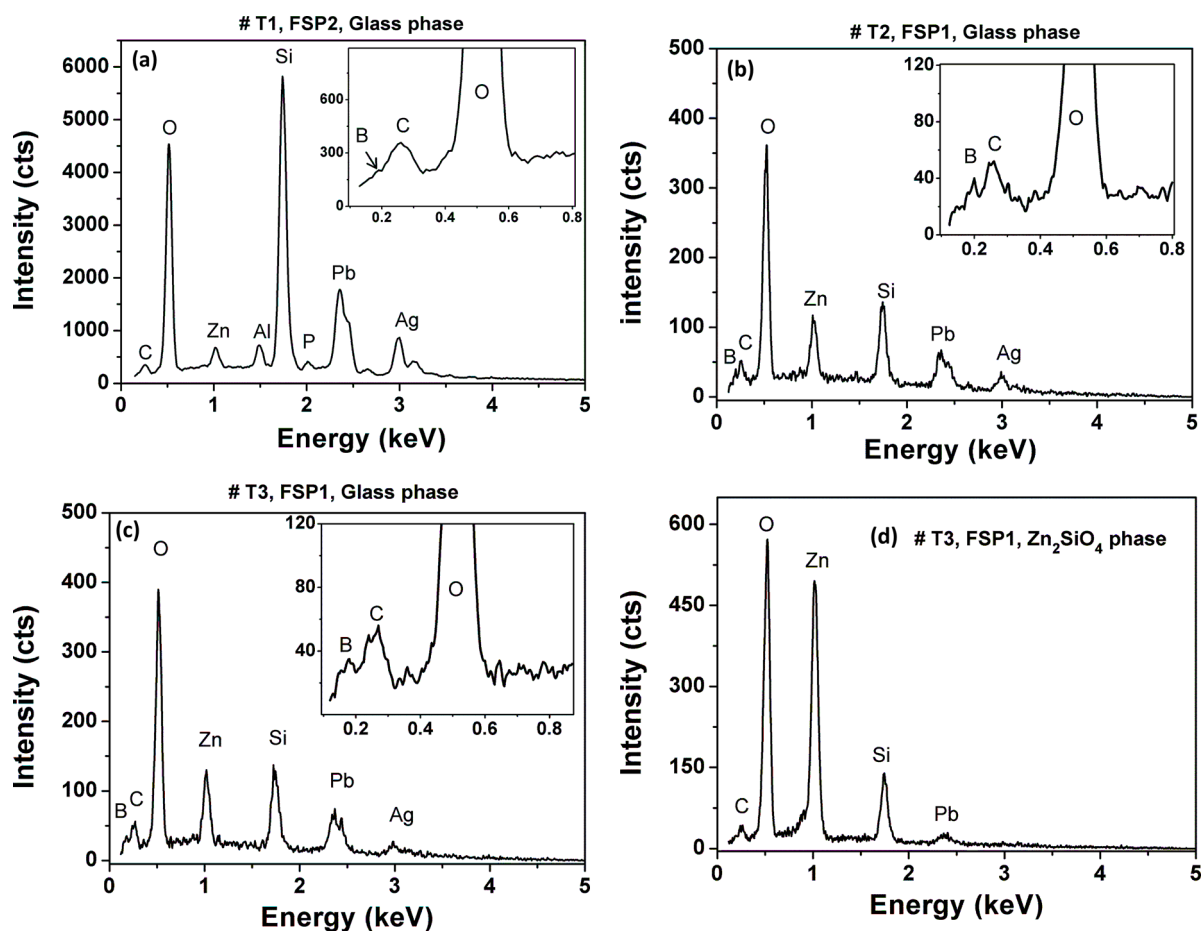
Figure 3.6: SEM-EDX spectra obtained in the glass phase for textured cells; (a) # T1, small Zn, and P peaks were found in the glass. (b–d) # T2 and # T3 reveal a huge Zn peak comparable to cell # T1 and a small B peak in the spectrum. Note that the P peak is not visible in the spectrum of cell # T2 and # T3.

Cell # T1 contacted with paste FSP2 revealed a small mole fraction of Zn (2 at %) and an Al peak (see Figure 3.6a) in the glass layer. Also, note that P and B peaks were identified in the spectra. A small shoulder at 0.183 keV could be identified as a B peak and can be seen in the inset of Figure 3.6a.

For cells # T2 and # T3 contacted with same paste FSP1, a large Zn peak was observed yielding a Zn mole fraction of 8 at %. For both cells, a B-K peak was clearly observed (see inset Figure 3.6b and c) in the spectrum of the glass phase. The overfired cell revealed a high B peak in the spectrum as compared to the optimally fired cell # T2. Also, Zn_2SiO_4 rich oxide phases were found in the glass phase for both cells (see Figure 3.6d). In contrast to cell # T1, no P peak was detected in the glass layer of cells # T2 and # T3.

3.5 Discussion

3.5.1 Low contact resistance of <111> oriented Si planar cells

The explanation of the contact resistance by microstructural details, as observed by a microscopic analysis, is not possible in a direct manner. Instead, the contact resistance is affected by: (i) the Si orientation and (ii) chemical composition and wetting behavior of the paste used. The microstructure, particularly the formation of Ag nanocrystals is strongly affected by the orientation of the Si substrate. As a consequence, cells with significantly different contact resistances and microstructures were processed and based on this analysis a correlation of contact resistance and microstructure was carried out. It could be shown that a low contact resistance is determined by the shape of the Ag nanocrystals and the wetting behavior of the paste together with the density of Ag colloids in the glass layer. The exact shape of the formed Ag nanocrystals is important since they are responsible for the current transport in screen printed silver contacts [60, 68]. In several publications, the exact shape of these Ag nanocrystals has not been clearly addressed due to selective etching process applied during the sample preparation [22, 73]. We believe that the etching process used for the sample preparation yielded a considerable amount of artifacts in the SEM images and, therefore, it is difficult to interpret the shape unambiguously by this preparation method.

Based on the microstructural and contact resistance analysis, the following three points can be summarized: Firstly, the formation of the lens shaped Ag crystals on <111> oriented Si yields a low contact resistance. Si <111> planes are closed packed, they yield small surface and interface energies as compared to <100> planes of Si. This anisotropy seems to be important for both the contact formation and the contact resistance.

Secondly, the contact resistance correlates to the wetting ability of the paste. A continuous glass layer filled with a high density of Ag nanocolloids correlates with a low contact resistance. On the other hand, a discontinuous glass layer containing small Ag nanocolloids yields a large contact resistance.

Finally, due to an increased lateral dimension and less penetration depth, lens shaped Ag crystals are necessary for achieving a low contact resistance. Since pyramidal Ag crystals are embedded deeper than lens shaped Ag crystals, therefore such nanocrystals are not necessary for providing a low contact resistance path. These observations are consistent with the work of Kontermann et al. in which they showed that the coverage fraction at the Si/Ag interface and the pit depth determine the specific contact resistance [83].

The effect of Si substrate orientation on the shape of Ag nanocrystals has been investigated in the literature [69, 72, 73, 74, 75]. Cabrera et al. found an increase of the contact resistance of <100> planar Si as compared to textured cells, which fully agrees with our experimental observations. The results of Cabrera et al. have been interpreted in such a way that a strong paste dependence of the contact resistance was claimed for <100> planar samples. We do not believe that this conclusion is right: if the ratio of the contact resistances of textured vs. planar samples is considered, the effect of paste on this ratio is only about a factor of 2. It just indicates that the effect of paste is small (factor of 2) and that the effect of Si surface orientation is the dominant quantity setting the ratio of the contact resistance of planar (100) oriented vs. textured cells with (111) faces between 12.5 and 25 [73].

3.5.2 Structure-property correlation in the textured cells

In accordance with the planar cells results, pyramidal Ag crystals are only formed at the tip and at the edges (intersection of {111} plane) of the Si pyramids. However, lens shaped Ag crystals are formed at the faces of the Si pyramids. As the faces of the Si pyramids are {111} oriented, therefore, the lens-shaped crystals are more important for the low contact resistance as compared to pyramidal Ag crystals.

For the optimally fired cell # T1, a continuous wetting of the glass layer together with a high density of Ag nanocolloids is mainly responsible for a low contact resistance. The temperature dependent series resistance of such cells shows a weak metallic behavior. Moreover, the chemical analysis of the glass layer confirmed that the paste FSP2 contained a small mole fraction of Zn, Al and P. Thus, the differences in the chemical composition of the pastes render the prominent differences in their wetting ability and hence the electrical properties of the cells.

For the optimally fired cell # T2, a thin glass layer and relatively small oxide phases were observed that yield a lower contact resistance in comparison to the overfired cell # T3. As mentioned in the above section, the overfired cell # T3 showed a thick, discontinuous glass layer embedded with Zn_2SiO_4 rich oxide phases. These oxide phases act as blocking layers for the current transport through the glass layer to the Ag bulk. The difference between the optimally fired cell # T1 and cells # T2 and # T3 is the wetting behavior and density of Ag colloids in the glass layer. Cells # T2 and # T3 show poor wetting and a small density of Ag colloids as compared to cell # T1.

3.5.3 Possible current paths for cells with low contact resistance – a 2D model of the percolative current path via Ag colloids in the glass layer

In the literature, one-dimensional transport models are suggested yielding a direct current path from Ag crystallites to the Ag bulk [24, 64, 67, 73, 84]. Our microstructural analysis does not support these one-dimensional transport models. Large differences in Ag nanocolloid densities were observed in the microstructural analyses for the different cells. Indeed the cell # T1 with the largest density of nanocolloids yielded the smallest contact resistance. As a result, a large volume fraction of Ag nanocolloids correlates with a small contact resistance and a weak metallic behavior in the temperature dependent series resistance.

Also, we found that a very thin glass layer seemed to be always present between the Si emitter and the Ag bulk of the contact finger [22, 24]. If direct contacts between Ag nanocrystals and bulk Ag

existed this would yield a metallic signature of the contact resistance. Only for # T1, a weak metallic behavior of the series resistance was observed, not for the other samples. The contact resistance of # T2 is four times larger as for # T1 at room temperature and the temperature dependence switches from metallic to semiconducting. For explaining these observations we suggest a three-dimensional percolative current path that runs through the glass layer and consists of Ag nanocolloids. The density of the Ag nanocolloids and the resistivity of the glass determine the contact resistance in this model. The proposed percolation model is purely geometrical and assumes that the electrical resistance of the glass (ρ_{Glass}) is large but finite and the resistance of the Ag nanocolloids is negligible compared to the glass. The Ag nanocolloids generate current filaments across the glass layer with reduced resistivity and thereby introduce a percolative nature of the current. The goal of the model is to describe how the density and size of the Ag nanocolloids will affect the contact resistance. For periodically arranged nanocolloids with identical size an analytical expression for the percolation limit is derived that depends only on the volume fraction of the Ag nanocolloids, but not on the size of the nanocolloids. The model explains that in solar cells with small densities of nanocolloids large contact resistances are found.

From Figure 3.7b we assume a n×n matrix arrangement of the square shaped Ag colloids in a glass layer with thickness a. The colloids generate 2d filaments, with a length a and a width D, the size of an Ag colloid. Note that the size of the Ag nanocolloids is smaller than the thickness of the glass layer. Along such an individual filament, path #1 in Figure 3.7b, the resistance is $R_{Filament}^{ind} = \rho_{Glass} * n * \left(\frac{a}{nD} - 1\right)$ an individual filament of path #1 consists of n identical segments the resistivity of each segment is $\rho_{Glass} * \frac{1}{D} * \left(\frac{a}{n} - D\right)$, $\frac{a}{n} - D$ is the length of the segment, D is the width. It is reduced with respect to pure glass path #2 in Figure 3.7b. For path #2 between such two filaments, the 2d resistance is $R_{Glass}^{ind} = \rho_{Glass} * \frac{a}{\frac{a}{n} - D}$, a is the length of path #2 and a/n-D is its width. ρ_{Glass} is the specific resistance of the glass in 2d, unit Ohm.

The resistance of all the filament paths in a square $a*a$ of the glass layer, path #1 with Ag nanocolloids and path #2 without Ag nanocolloids, are combined in parallel to calculate the total resistance.

$$R_{Total}^{-1} = R_{\#1}^{-1} + R_{\#2}^{-1}. \quad (3.1)$$

$$R_{\#1}^{-1} = n * R_{Filament}^{ind\ -1} = \frac{1}{\rho_{Glass} * \left(\frac{a}{nD} - 1\right)}. \quad (3.2)$$

$$R_{\#2}^{-1} = n * R_{Glass}^{ind\ -1} = \frac{1 - \frac{D\,n}{a}}{\rho_{Glass}}. \quad (3.3)$$

Dn/a in Eq. (3.3) is the fraction of the filaments along a length *a* perpendicular to the current and (*1-Dn/a*) in Eq. (3.3) is the fraction of the pure glass. Putting Eq. (3.2) and Eq. (3.3) into Eq. (3.1) we get the total resistance in Ohm of a square $a*a$ matrix of the glass layer

$$R_{Total}^{-1} = \left(\rho_{Glass} * \left(\frac{a}{n\,D} - 1\right)\right)^{-1} + \left(\rho_{Glass} * \frac{1}{1 - \frac{n\,D}{a}}\right)^{-1}. \quad (3.4)$$

Introducing the volume fraction (VF) of the nanocolloids, i.e. the area ratio of the Ag nanocolloids to the total area

$$VF = \frac{n^2\,D^2}{a^2}. \quad (3.5)$$

47

Putting Eq. (3.5) this into Eq. (3.4) we get the final expression for the total resistance (R_{Total}) which only depends on the volume fraction but not on the size of the nanocolloids.

$$R_{Total} = \rho_{Glass} * \frac{1 - \sqrt{VF}}{1 + VF - \sqrt{VF}}. \quad (3.6)$$
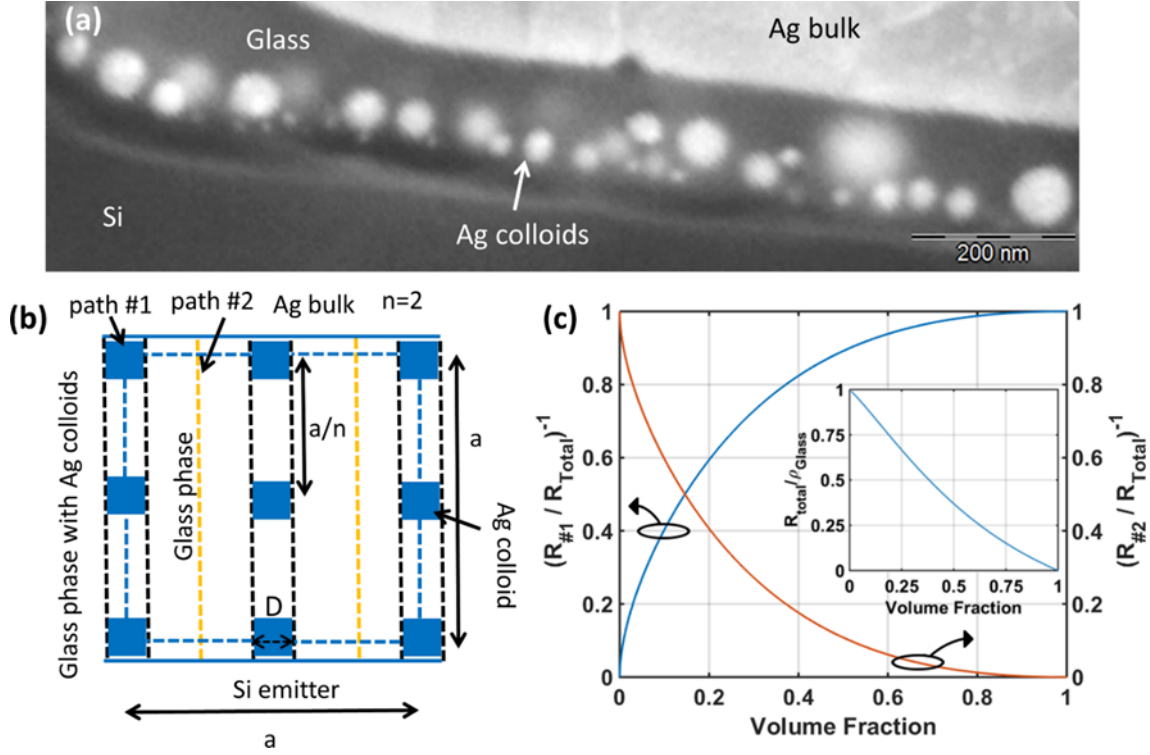
Figure 3.7: (a) HRSEM image of the Ag nanocolloids obtained at the Si/Ag interface. (b) Schematic model of the possible current paths trajectories (path # 1 via Ag nanocolloids and path # 2 glass phase) from the Si emitter to Ag bulk contacts. (c) Resistance vs. Volume fraction of circular Ag nanocolloids. The percolative limit is reached with a volume fraction close to 15%.

In Figure 3.7c the contributions of the conductance of path #1, $R_{Total}/R_{\#1}$ and path #2 $R_{Total}/R_{\#2}$ to the 2d total conductance are plotted against the volume fraction of Ag colloids. The conductance of path #1 is dominant for volume fractions of Ag nanocolloids larger than 15 %. The intersection appears for the volume fraction VF for which $R_{\#1} = R_{\#2}$ and can be calculated as the percolation limit of $VF_{Limit} = \left(\frac{3-\sqrt{5}}{2}\right)^2 \approx 0.15$.

3.6 Conclusions

In this work, the formation of microstructure and its correlation to the contact resistances are summarized for the front side metallization. The contact resistance is affected by the orientation of the Si surface and the properties of the paste. Microstructure, particularly the Ag nanocrystal formation is controlled by the orientation of the Si substrate: on planar cells lens shaped Ag crystals are formed on <111> oriented Si and pyramidal shaped Ag crystals for <100> oriented Si. TLM measurements confirmed that planar <111> oriented Si solar cells yielded a low contact resistance, and therefore, lens shaped Ag nanocrystals are important for achieving a low contact resistance.

Moreover, a low contact resistance is linked to the wetting behavior of the paste and a high density of Ag colloids in the glass layer. A continuous glass layer filled with metallic Ag nanocolloids correlates to a low contact resistance. Temperature dependent series resistance measurements reveal a weak metallic signature on such cells. Based on the above findings a 2d geometrical model has been proposed, in which an Ag nanocolloid network assists a percolative charge transport through the glass layer to the Ag bulk of the finger. For the percolation transport, a minimum of 15 vol% of Ag nanocolloids in the glass layer is necessary, as shown by analytical expressions.

Chapter 4

N-type single-crystalline Si solar cells: front side metallization for solar cells reaching 20 % efficiency [85]

4.1 Background

Over the past years, there has been an active interest to use n-type single-crystalline Si solar cells which offer great possibilities and advantages over p-type cells, due to their high carrier lifetimes of minority charge carriers, the absence of light induced degradation, and reduced sensitivity towards metal impurities [86, 87, 88]. Screen printing technology using Ag pastes has been sufficiently matured to contact the P doped emitters, [23, 64] but does not successfully transfer to B doped emitters and, therefore, yields a high specific contact resistance of > 50 mΩ cm^2 [89, 90]. The main challenge with B doped emitters is to achieve a low contact resistance without degrading the cell performance. Previous studies have reported that adding Al to the Ag paste significantly reduces the specific contact resistance to a few mΩ cm^2 [89, 90, 91, 92, 93]. However, depending on the amount of Al, the screen-printed Ag-Al paste exhibits Ag/Al spikes (deeper than 1 μm) grown at the Si surface [91, 92, 93]. Such inappropriate spikes penetrate the p-n junction and introduce higher dark saturation current density beneath the metal contacts. This, in turn, decreases the open circuit voltage (V_{OC}) [90, 94] and is limiting the efficiency of such cells.

Up to now, only a few attempts have been made to overcome these drawbacks and to further understand the contact formation mechanism on B doped emitters [90, 95, 96]. Lago et al. suggested that addition of Si powder into the Ag-Al paste significantly prevents the spiking problem. Despite of preventing the spike formation and recombination losses, the efficiency reported in that paper was only 14.4 % [90]. Recently, Lohmüller et al. reported that the recombination losses beneath the Ag-Al contacts can be reduced (i) by increasing the junction depth deeper than 0.5 to 1 μm or (ii) by the formation of small Ag nanocrystals for obtaining a specific contact resistance of about 2 mΩ cm^2 [96]. In spite of these studies, no systematic studies on B doped emitters including detailed chemical composition, microstructural and temperature dependent series resistance measurements have been carried out yet. Also, alloying Al into the Ag paste significantly changes the chemical reactivity of the paste and reduces the contact resistance of the front side metallization. Therefore, it is worthwhile to optimize the chemical composition of the paste, in particular, its Al content, in more detail to control the contact formation mechanism.

The front side contact of n-type cells has been investigated in detail by Edler et al. indicating large dark saturation current density below the metal contacts [97]. This is dramatically different as compared to p-type cells for which these dark saturation currents are much less. Nevertheless, similar questions appear for p and n-type cells: what is the relevant current path and by which mechanisms is the contact resistance controlled.

To date, different current models were reported in the literature for p-type solar cells: Model I assumes a direct connection between Ag nanocrystals and the Ag bulk of the finger [24]. Model II assumes that the current flows through the glass layer by metallic Ag colloids assisted tunnelling [25]. Recently, we proposed a percolation model in which metallic Ag colloids generate current filaments with reduced resistivity across the glass layer [26]. The glass layer is decorated with a high density of Ag colloids and plays a decisive role for the charge transport across the Si/Ag interface. The role of the glass layer, particularly its chemical composition was investigated in detail [26].

In the present study, we report a combined microstructural, chemical analysis and temperature dependent series resistance measurements of n-type cells with B doped emitters, using two different front side pastes: one containing Ag-Al and the other one Ag paste without Al. The microstructure and chemical analysis of the contact interface were investigated by scanning electron microscopy (SEM). The contact interface was analyzed according to; wetting behavior of the paste, Ag colloid/nanocrystals formation, chemical composition of the glass phase and the presence of a residual SiN_X layer.

In addition, temperature dependent electrical measurements on small cells were carried out, as explained for p-type cells in Refs. [26, 62]. These measurements are important, because microstructural analysis by SEM-EDX is not sensitive enough to detect the distribution of dopants and impurities, particularly in the emitter and the space charge region. Microstructural analysis of solar cells alone is not sufficient to correlate directly with their electrical properties, particularly series and contact resistance. Paste dependent effects have to be identified in electrical and microstructural investigations, then yielding a structure-property correlation. Therefore, a combination of microstructural analysis together with detailed temperature dependent I–V measurements were carried out in this work. Note that such temperature dependent I–V measurements yield the temperature dependent series resistance and from this the temperature dependent contact resistance [26].

Results of the microstructural characterization of both n and p-type cells were converted into a percolation model to explain the role of Ag colloids in the glass layer [26]. The Ag nanocolloids generate current filaments across the glass layer with reduced resistivity and thereby introduce a percolative nature of the charge transport.

4.2   Experimental details

4.2.1   Solar cell fabrication and characterization

All cells were identically processed only the front side metallization was different. Large area (15.6 x 15.6 cm^2) PERT (Passivated Emitter Rear Totally diffused) Si solar cells were fabricated on n-type $< 100 >$ oriented Cz wafers with a base doping of 3 Ω-cm at ISC-Konstanz. The cell processing and the schematic representation of the n-PERT cell are described under [98]. The homogenous diffused p+ (boron) emitter and n+ (phosphorous) BSF regions had sheet resistance of 66 Ω/sq and 50 Ω/sq, respectively. A schematic representation of the n-PERT cells is shown in Figure 4.1. Two different commercially available pastes were used for the front side metallization in this study: paste Ag–Al containing Al and paste Ag without Al. Cells # T1 and # T2 were contacted with paste Ag–Al, whereas cell # T3 was contacted with paste Ag. On cells # T1 and # T3 busbars (BB) were realized using a firing through BB paste, whereas on cell # T2 a non-firing through BB was printed. All cells

were fired at a set peak point temperature of 830 $^\circ C$, however, a separate firing optimization for the Ag paste was not performed.
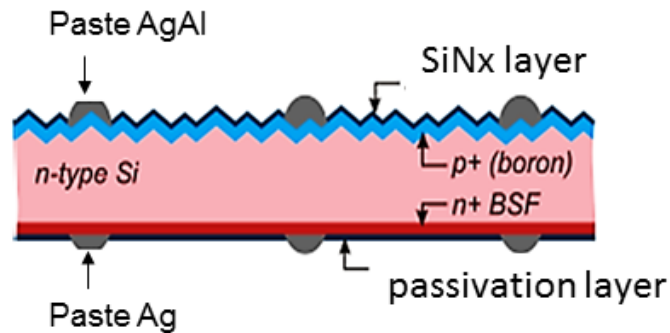
Figure 4.1: Schematic representation of n-PERT Si solar cells.

The dark and sun I–V measurements on large area samples were carried at room temperature (RT) measured from an AAA Halm I–V measurement setup. The series resistance parameters were extracted through shifted I–V and light I–V fit methods and shunt resistance parameters through dark forward dark reverse and light I–V fit methods from Halm I–V setup. These methods provide an insight on the effect on cell resistance due to the operation conditions. Under illumination, due to increased current density, the effect of a low shunt resistance can be distinguished on # T3 in comparison with # T1 and # T2. The specific contact resistance of the front side fingers was measured by TLM method, on dedicated stripes at room temperature (RT).

4.2.2 Sample preparation and electrical characterization of small cells

For microstructural analyses samples were investigated in plan-view and in cross-sections. The Si/Ag metallization interface was studied using a Jeol 6500F scanning electron microscope (SEM) equipped with an Oxford Pentafet energy-dispersive X-ray (EDX) detector. [17, 20]. Low magnification backscattered electron images (BSE) were acquired to identify the wetting behavior of the paste and different phases present at the Si/Ag metallization interface. Details of the sample preparation are given in Refs. [26, 60]. Temperature dependent dark current I–V curves were obtained in a temperature range from 80 K to RT. From this the temperature dependent series resistance on small cells was determined by fitting the dark I–V curves with the two diode model [10, 63].

4.3 Results

4.3.1 Electrical properties of large area cells

The electrical properties of the large cells (15.6 x 15.6 cm^2) are summarized in Table 4.1. Cells # T1 and # T2 contacted with paste Ag–Al showed specifically lower specific contact resistances (4 mΩ cm^2), smaller series resistances (0.53–0.57 Ω cm^2) and higher efficiencies ($\sim$ 20.0%). In contrast, cell # T3 contacted with paste Ag yielded a significantly higher specific contact resistance ($>$ 100 mΩ cm^2), series resistance (1.60 Ω cm^2) and a lower efficiency (16.09%). The series resistance values shown above were extracted from the shifted I–V method.

Cells	Paste	J_{SC} [mA/cm²]	V_{OC} [V]	FF [%]	η [%]	ρ_C [mΩ.cm²]	R_S [Ω.cm²]		R_P [Ω.cm²]		T_{FFO} [°C]
							Shifted I-V method	Light forward I-V method	Dark forward-Dark reverse method	Light forward I-V method	
# T1	AgAl	38.98	0.647	78.68	19.86	4	0.57	0.54	6740	9885	830
# T2	Ag–Al	39.21	0.650	78.24	19.96	4	0.53	0.54	7060	8727	830
# T3	Ag	38.52	0.634	65.86	16.09	>100	1.60	1.26	4070	792	830

Table 4.1: Summarizes the electrical properties of large cells obtained on three textured cells # T1, # T2 and # T3, respectively, and were contacted with two different front side pastes: paste Ag–Al and paste Ag. Cells # T1 and # T2 contacted with paste Ag–Al yielded a lower specific contact resistance, small series resistance and higher efficiency as compared to cell # T3 contacted with paste Ag. The series resistance parameters were extracted from the shifted I–V and light I–V fit methods, whereas shunt resistance parameters were determined from the dark forward dark reverse and light I–V fit methods from Halm I–V setup.

We consider the Rs value of cells # T1 and # T2 was in the same range, since the Rs extracted from the light I–V method points out in this direction (see Table 4.1). However, slight variation in FFs values might come from the process in-homogeneities.

Both cells # T1 and # T2 yielded similar electrical properties due to the same front side paste. In fact, because of non-firing through busbars on cell # T2, a gain of 3 mV in V_{OC} is observed, due to the reduced metallization induced losses at the busbar metal contact area [99]. With the addition of Al into the Ag paste significantly reduces the series and specific contact resistance yielding high cell efficiency. Recent studies [100, 101] shows possible Al- free contact to boron doped emitters, however, it has to be demonstrated for the fabrication of solar cells with superior cell properties.

4.3.2 Electrical properties of small cells

4.3.2.1 Temperature dependent dark I–V curves and series resistance

Figure 4.2 a–c show the temperature dependent dark current (I–V curve) of cells # T1, # T2 and # T3, respectively. In Figure 4.2 currents are displayed they directly correspond to current densities, since the cell area was in the range of 1 cm^2.
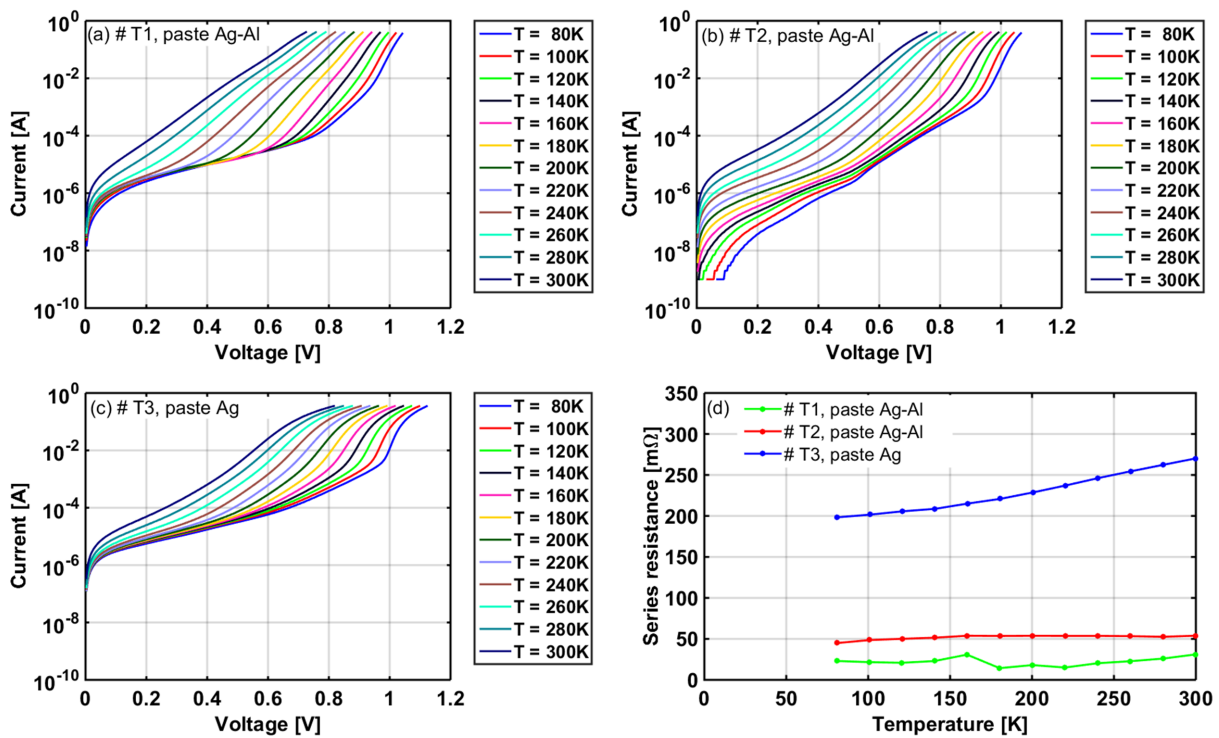
Figure 4.2: Temperature dependent dark current *I–V* curves measured on small cells. (a, b) cells # T1 and # T2 contacted with paste Ag–Al paste, (c) # T3 contacted with paste Ag. For each cell, the measurements were carried out between 80 K to 300 K. (d) shows the temperature dependent series resistance measurements obtained on the same cells.

The magnitude of the dark current densities at low voltages is affected by the shunt resistance of the diode, small shunt resistance would yields large dark saturation current densities and poor efficiency and are best seen in semi-logarithmic plots close to zero biasing voltage.

Cell # T1 contacted with paste Ag–Al yielded small current densities at low voltages of 10^{-7} A/cm^2

at RT and 10^{-8} A/cm^2 at 80 K, respectively. For cell # T2 contacted with same paste but non firing through busbars showed the smallest current densities, especially, at low temperatures 10^{-7} A/cm^2 at RT and 10^{-9} A/cm^2 at 80 K as compared to cell # T1. In contrast, cell # T3 contacted with paste Ag showed the highest current densities at low voltages of 10^{-6} A/cm^2 at RT to 10^{-7} A/cm^2 at 80 K correlated with its small shunt resistance and decreased efficiency as compared to cells # T1 and # T2. The current at large voltages is related to the series resistance, a large slope corresponds to a small series resistance. The high current regime of the I–V curves showed the smallest slope for cell # T3 contacted with paste Ag as compared to cells # T1 and # T2 contacted with paste Ag–Al. It is also noticeable that the slope increases with decreasing temperatures, indicating a lower series resistance close to 80 K.

The temperature dependent series resistance was determined quantitatively from I–V curves and are shown in Figure 4.2. For cells # T1 and # T2 contacted with paste Ag–Al, the series resistance was below 35 and 50 mΩ cm^2 at RT, respectively. Note that the series resistance was only weakly temperature dependent for cells that were Al alloyed, as typically seen for alloys. For cell # T3 contacted with paste Ag showed a large series resistance of 270 mΩ cm^2 at RT. The series resistance was about 200 mΩ cm^2 at 80 K and decreases almost linearly, indicating a metallic behavior in the entire temperature range. In short, cells # T1 and # T2 contacted with paste Ag–Al revealed a lower series resistance (35–50 mΩ cm^2) as well as a significantly lower specific contact resistance (4 mΩ cm^2) and the higher efficiency, whereas a higher series (270 mΩ cm^2) and specific contact resistance (>100 mΩ cm^2) was found for cell # T3 contacted with paste Ag.

4.3.3 Microstructural analysis

4.3.3.1 Wetting behavior of the paste Ag–Al and paste Ag

Figure 4.3a–c show the plan-view color coded backscattered electron images (BSE) of the textured cells # T1, # T2 and # T3, respectively, acquired at the Si/Ag contact interface. In BSE images the gray value of each phase depends on its mean atomic number, i.e. it was possible to assign a different color to each phase, i.e. Si pyramids (yellow squares), carbon (green), Ag (blue) and glass phase (pink).

Cells # T1 and # T2 contacted with paste Ag–Al showed a more pronounced wetting of the glass phase between the Si emitter and the Ag bulk of the finger (see Figure 4.3a–b). At this contact interface a continuous glass layer with a varying thickness from 500 nm down to few tens of nm was found that contained a high density of metallic Ag colloids (70 Ag colloids/μm^2) as shown in Figure 4.3d–e. For both cells # T1 and # T2, no marked differences could be observed in the microstructural analyses.

For cell # T3 contacted with Ag paste yielded a thin glass layer, typically few nms to 400 nm thick at the Si/Ag contact interface (see Fig. 3c and 3f). Besides this, the glass layer contained only a small density of Ag colloids (15 Ag colloids/μm^2) and precipitates. Different to cells # T1 and # T2, no accumulation of the Ag colloids was observed at the Si surface for cell # T3 contacted with paste Ag.

4.3.3.2 Microstructural analysis at the Si/Ag–Al and Si/Ag interface

The microstructure at the Si/metallization contact was investigated by high-resolution SEM both in plan-view and in cross-sectional view. Figure 4.4a–c shows the cross-sectional SEM images of the textured cells # T1, # T2 and # T3, respectively, the corresponding plan view images are shown in

Figure 4.4d–f.
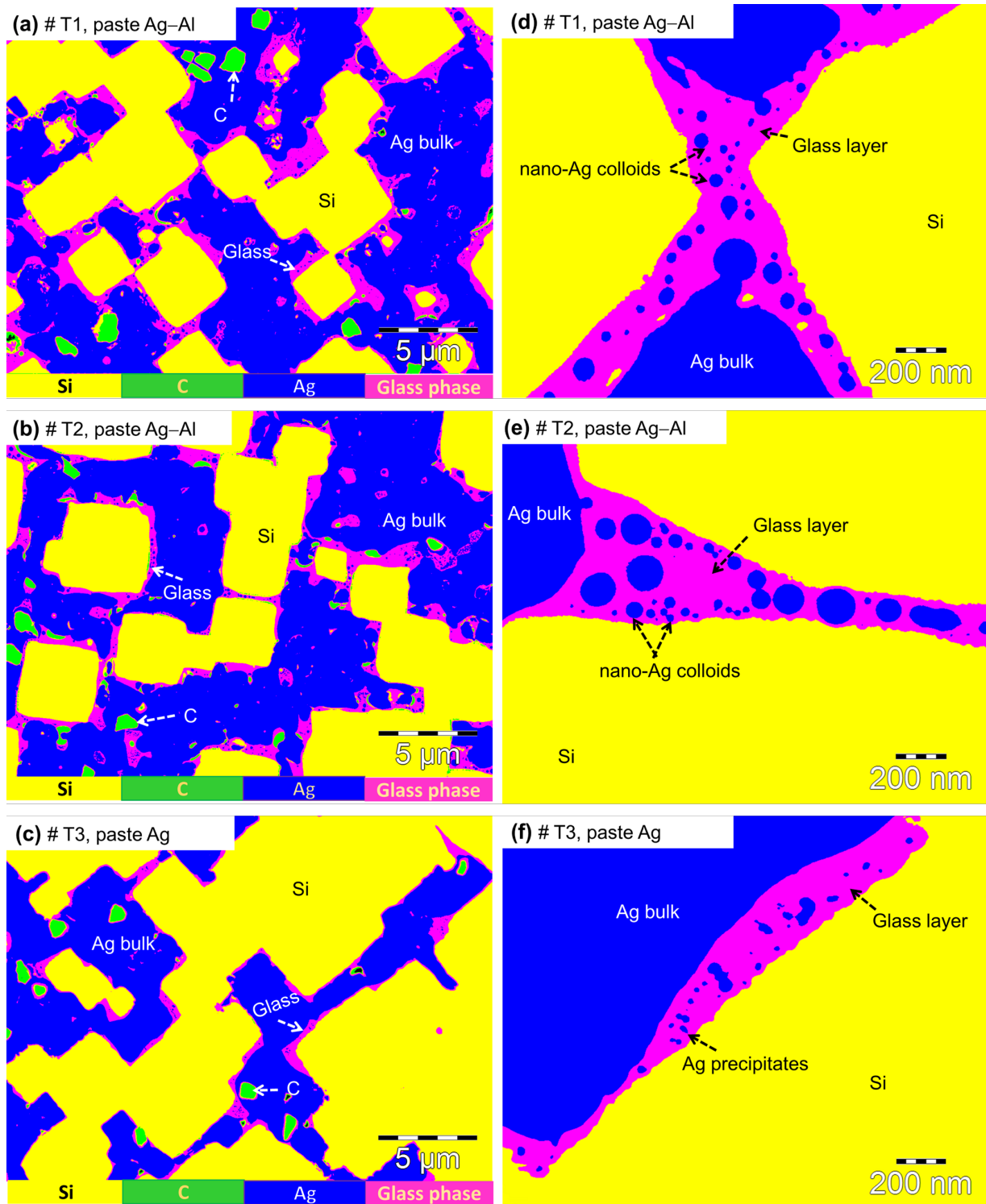
Figure 4.3: Plan-view false color coded BSE images of the cells # T1, # T2 and # T3 obtained at the Si/Ag interface. (a–c) low magnification BSE images showing the wetting behavior of paste Ag–Al and paste Ag. (d–f) show the corresponding high-magnification images.

Along the contact interface, an inhomogeneous glass layer with varying thickness was present which contained a significant amount of Ag colloids and precipitates. Cells # T1 and # T2 contacted with paste Ag–Al yielded a glass layer embedded with a high density (70 Ag colloids/μm^2) of Ag colloids

(see Figure 4.4a, b, d and e). The size of the Ag colloids was between 5–150 nm in diameter. For cell # T3 contacted with paste Ag, the glass layer contained a small density of Ag colloids (15 Ag colloids/μm^2). Interestingly, pyramidal Ag nanocrystals and Ag/Al spikes were not observed at the Si emitter for all cells.
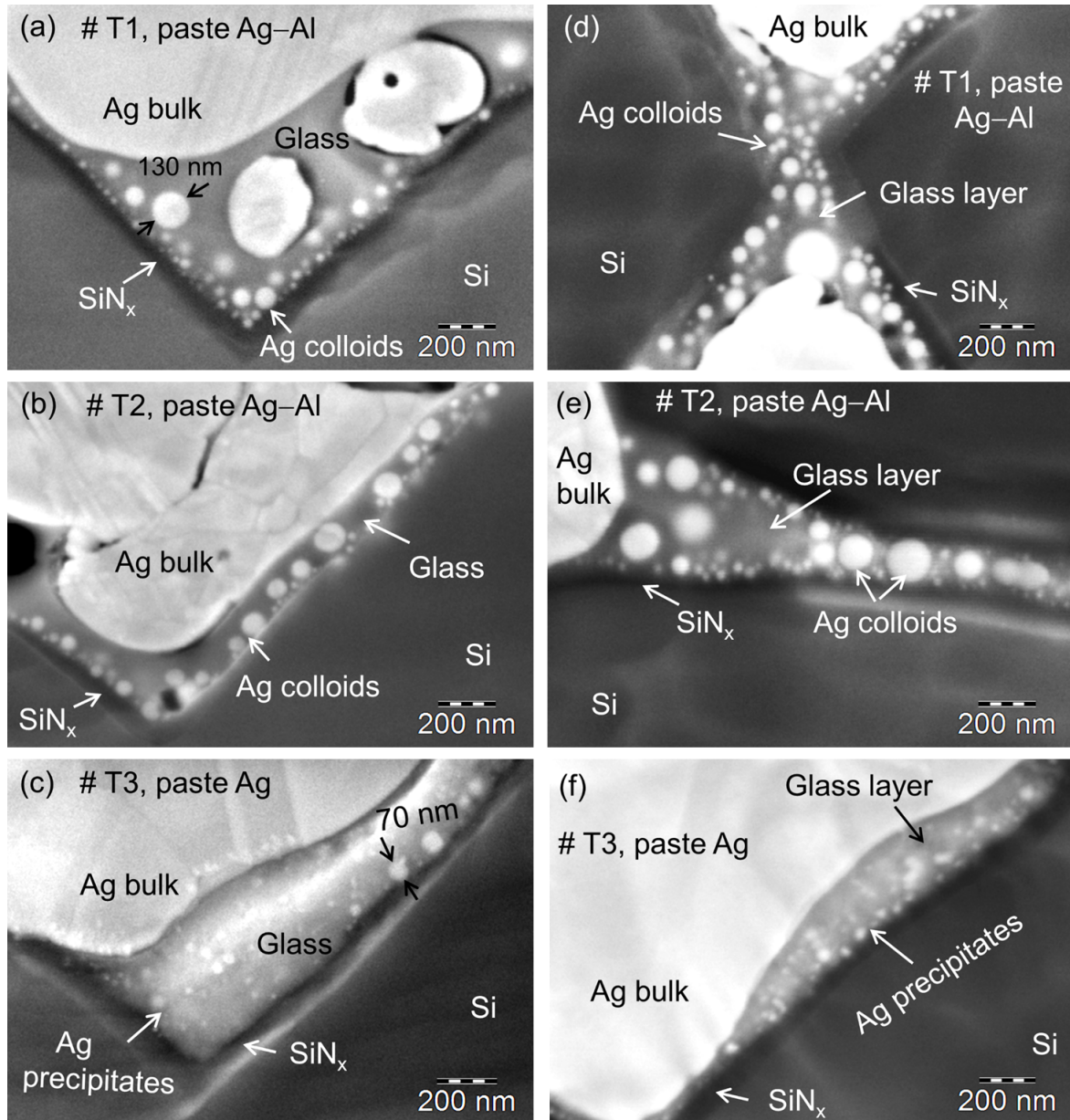
Figure 4.4: (a–c) show HRSEM cross-sectional images of the cells # T1, # T2 and # T3 acquired at the Si/Ag interface. (d–f) represent plan-view images of the same cells. Cells # T1 and # T2 contacted with paste Ag–Al revealed a high density of Ag colloids in the glass layer, whereas cell # T3 contacted with paste Ag yielded a small density of Ag colloids.

The thickness of the SiN_X layer was 20–60 nm for cells # T1 and # T2 contacted with paste Ag–Al. On the other hand, cell # T3 contacted with paste Ag showed a thicker 40–70 nm SiN_x layer at the contact interface. Both pastes did not remove the SiN_X layer completely and a discontinuous layer resulted with segments being up to several μm long: at various locations the SiN_X layer was completely removed where Ag colloids had direct contact with the Si emitter. Ag colloids sitting close to the Si surface are smaller in size as compared to colloids within the glass layer. The density of the Ag

colloids was affected by the presence of the SiN_X layer: with the SiN_X layer present, a high density of Ag colloids was observed in the glass layer.

The SiN_X layer might block the diffusion of Ag and Al into the Si emitter according to the contact formation model developed by Hong et al. and, therefore, precipitation starts in the form of Ag colloids in the glass layer [76]. Hörties et al. also reported the local opening (10 %) of the SiN_X layer at the contact interface for n- type cells [64], which is consistent with our microstructural results.

4.3.4   Quantitative chemical analysis of the glass phase and the SiN_X layer

The chemical composition of the Si/Ag interface was further investigated by SEM-EDX spectroscopy. All spectra were plotted in a logarithmic fashion to highlight elements with small mole fractions.

Figure 4.5a–c shows EDX spectra by EDX point spectroscopy in the SEM obtained in the glass phase of cells # T1, # T2 and # T3 respectively. These spectra were quantitatively analysed, and their mole fraction ratios are given in Table 4.2. The matrix phase of the glass of all cells consists of SiO_2, Pb (5–6 at.%) and Ag being dispersed in the glass phase (see Table 4.2) yielding a Si-Pb oxide [76, 78]. Besides these three elements, Zn and Al were found as additives. Their mole fractions were only 1–3 at.%. For cell # T3, Zn and Al peaks were not detected in the glass phase and the mole fractions of these elements were below the detection limit. EDX spectroscopy could prove that the glass layer reflects the composition of the paste: Al being present in the glass phase (1.2 at.%) if paste Ag–Al was used and not detectable in the glass phase of the Ag paste.

Paste	Si [at.%]	O [at.%]	N [at.%]	Pb [at.%]	Ag [at.%]	Al [at.%]	Zn [at.%]	Phase
Ag−Al	28.8±3.4	61.8±1.4	–	5.0±0.03	4.5±1.3	1.2±0.3	2.4±0.4	glass
Ag	26.7±4.9	60.9±1.0	–	6.1±0.1	6.3±3.8	–	–	glass
Ag−Al	75.5±8.3	15.4±3.5	8.8±6.0	–	–	–	–	SiN_X
Ag	64.4±6.1	13.8±5.2	21.7±2.6	–	–	–	–	SiN_X

Table 4.2: Quantitative chemical analysis by EDX spectroscopy in the SEM. The chemical composition of the glass and SiN$_X$ phases of cells contacted with paste Ag−Al and paste Ag was investigated.

EDX spectroscopy also proved the presence of the SiN_X layer, which is seen in the SEM images as a faint, dark contrast. Imaging alone would be ambiguous and would not prove the presence of this layer.

The SiN_X layer was quantitatively investigated (see Table 4.2) and the spectra corresponding to cells are shown in Fig. 5 d–f. Cells # T1 and # T2 contacted with paste Ag–Al yielded a 20−60 nm thin SiN_X layer, fairly large Si peak and small N and O peaks were detected, due to the poor lateral resolution (0.5 μm) of SEM-EDX. For cell # T3 contacted with paste Ag the SiN_X layer was thicker, about 40−70 nm, and apart from the Si peak, a fairly large N peak was clearly identified in the spectra (see Figure 4.5f). Note that for all cells, contacted with both paste Ag–Al and paste Ag, dopant elements such as B and P were not detected in the glass phase. These elements were detected in the glass phase of p-type cells [26].
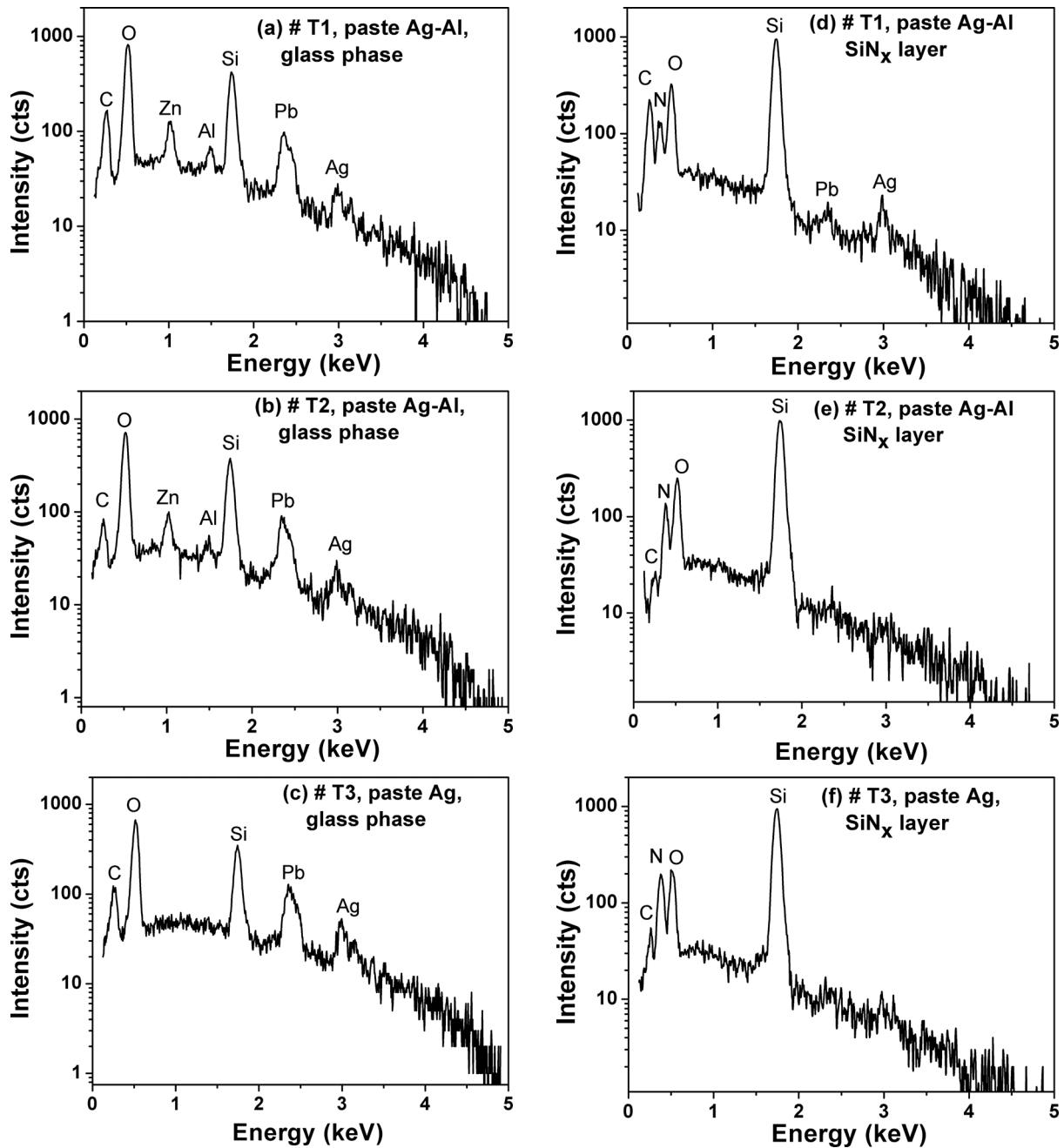
Figure 4.5: SEM-EDX spectra of different phases presented at the Si/Ag interface. All spectra are shown in the logarithmic scale. (a–c) show the glass phase of cells # T1, # T2 and # T3, respectively. Cells # T1 and # T2 contacted with paste Ag–Al showed a small Zn and Al peaks in the glass phase, whereas, for cell # T3 contacted with paste Ag, Al and Zn peaks were not detected in the spectra. (d–f) show the spectra of a residual SiN_X layer.

4.4   Discussion

4.4.1   Microstructural analysis, series, and specific contact resistance

Screen printed single-crystalline n-type Si solar cells yield efficiencies that are limited by electrical losses due to a high-temperature front side metallization process, especially at the p^+ contact interface [97]. The electrical losses are strongly depending on the metallization fraction and are much more

severe for p^+ emitters (n-type cells) as compared to n^+ emitters (in p-type cells). For n-type cells, J_{01} is strongly inhomogeneous over the area of the cell and peaked at areas below the metallization [97]. Because of this inhomogeneous current distribution, a 2D simulation approach was applied by Elder et. al in which the emitter is understood as a structured region containing areas with and without metallization that have (strongly) different physical properties [97].

So far, the microstructural features observed at the contact interface and its correlation to the contact resistance at RT was investigated in the literature [89, 91, 93]. However, microstructural analysis of cells alone is not sufficient to correlate directly with their electrical properties determined at room temperature, particularly temperature dependent I–V curves, series and contact resistance give new insight.

Temperature dependent I–V curves yielded significant differences between the three cells investigated in this study: particularly the low voltage (0 V) and high voltage regimes are of interest. Note that the currents of the three different cells investigated here differ by orders of magnitude in the low voltage regime (Figure 4.2). Cell # T3 with the lowest efficiency shows the maximum current densities of about $10^{-3} mA/cm^2$, at low voltages. In Figure 4.2 currents are displayed they directly correspond to current densities, since cell area in the range of 1 cm^2 were used. A similar trend was seen in p-type solar cells [62] cells contacted with different pastes yielded significantly different current densities in the low voltage regimes in their I–V curve. Differences were also orders of magnitude, and current densities reached values up to $10^{-2} mA/cm^2$, see Fig. 5 in [62] for details. These increased current densities are more markedly seen when temperature dependent I–V curves are studied.

From temperature dependent I–V curves temperature dependent series resistance was determined, this procedure is, however, not straight forward. Different methods exist for determining the series resistance from I–V curves, for a detailed discussion see [10, 63]. Here we applied the method at large voltages which essentially is based on acquiring dark current I–V curves and fitting the two diode model. From this the series resistance at RT was determined as; 35–50 mΩ cm^2 for cells # T1 and # T2 contacted with paste Ag–Al and 270 mΩ cm^2 for cell # T3 contacted with paste Ag, cell area 1 cm^2. The ratios of series resistance measured on the small cells matched well with the results observed on the large cells, which were three times smaller for cells # T1 and # T2 as compared to the cell # T3. The absolute values of series resistance between small and large cells did not match: small cells yielded significantly smaller series resistance as compared to large cells. This is qualitatively understood that the dark I–V measurements use inject carrier into the contacts. The current crossing the junction is not homogenous and most of the current flows underneath the contacts, whereas in case of light I–V the current crossing the junction is nearly uniform and flows along the emitter to the contacts. This yields a low Rs value in the dark I–V measurements as compared to illuminated I–V curve for large cells [102].

The current distribution in dark I–V measurements probes more directly area under the contact [63]. The series resistance of different pieces of a single wafer yielded similar results indicating lateral homogeneity of the wafers for n-type cells. Cells contacted with paste Ag–Al yielded a significantly lower specific contact resistance (5 mΩ cm^2), small series resistance and high efficiency (20.0 %) as compared to cell # T3 contacted with paste Ag. The contact resistance of the cells # T1 and # T2 was 5 mΩ cm^2, whereas cell # T3 yielded a large contact resistance of about 100 mΩ cm^2. The series resistance was only weakly temperature dependent for cells # T1 and # T2, whereas cell # T3 yielded

a higher series resistance but more pronounced metallic temperature dependence. Microstructural analyses cannot explain the origin of the metallic behavior in the temperature dependent series resistance.

The microstructure of the front side contact was similar to that found in p-type cells [26]: the Si emitter was covered by a glass layer, typically 500 nm thick and containing Ag colloids, on top of which the bulk Ag of the finger was located. For cells # T1 and # T2 contacted with paste Ag–Al the glass layer contained a high density of 70 Ag colloids/μm^2. In contrast, cell # T3 contacted with paste Ag, contained only a small density of 15 Ag colloids/μm^2.

Note that for n-type cells studied here the chemical composition of the glass phase is different as compared to p-type cells: in the glass phase dopant elements such as B and P were below the detection limit of EDX microanalysis, whereas for p-type cells P can only be detected in the glass phase if paste FSP2 was used. However, B was found in the glass phase of both paste FSP1 and FSP2. We expect that B comes from the glass frit made of borosilicate glass [26]. Since the glass phase is in direct contact with the Si emitter and a high-temperature annealing was carried out, elements of the glass phase are assumed to diffuse into the emitter region. Therefore, the chemical composition of the glass phase is important for understanding the formation of low resistivity contacts.

Microstructural analyses of p-type cells yielded pyramidal and lens shaped Ag nanocrystals formed at the Si surface. These nanocrystals were covered by an interfacial glass layer containing metallic Ag colloids [23, 26, 60, 68, 77]. In case of n-type cells, no pyramidal or lens shaped Ag nanocrystals were formed at the Si surface.

The formation of pyramidal shaped Ag nanocrystals is related to an etching process since the pyramidal shape is introduced by (111) planes acting as surfaces of the pyramids [103]. It is well known that etching in Si depends sensitively on doping [104]. B doped emitters are used in n-type cells different to P doped emitters as used in p-type cells. Particularly important is the directional anisotropy of the etching: for B doping etching along $< 100 >$ is found on (111) oriented surfaces, this is not seen for P doped Si for which $< 111 >$ surfaces are etched in the $< 111 >$ direction [105]. Therefore, the absence of pyramidal shaped Ag nanocrystals for B doped emitters might be due to the etching property of this emitter that does not yield (111) oriented surfaces.

Another important finding is that Ag/Al contact spikes were not observed at the Si surface for cells contacted with paste Ag–Al. This might be due to the presence of a residual SiN_X layer detected at the contact interface. The residual SiN_X layer is beneficial twofold: (i) it prevents the diffusion of Ag/Al towards the Si surface, avoiding the formation of Ag/Al contact spikes in to the Si emitter, and (ii) minimizes excess etching of the Si surface by the glass frit.

Few publications reported a low contact resistance due to the presence of a high density of Ag/Al contact spikes and Ag nanocrystals [91, 92, 93, 106]. Such Ag/Al contact spikes might yield a low contact resistance but also might degrade the cell performance: if Ag/Al contact spikes are embedded deeper at the Si surface, shunts of the p-n junction occur together with higher dark emitter saturation current. This negatively affects the open circuit voltage and, hence, the efficiency of cells [90, 94, 97]. Therefore, the firing temperature has to match the chemical composition of the paste and is of paramount importance for controlling the optimum thickness of the SiN_X layer avoiding Ag/Al spike formation.

4.4.2 Structure-property correlation

Electrical data of large cells, microstructure analyses and the temperature dependent series resistance measurement of small cells yielded a detailed characterization of high efficiency n-type cells, necessary to establish a structure-property correlation. Previous investigations of p-type cells proved the relevance of this approach [26, 62]. For p-type cells, we observed that the contact resistance of the front side contacts sensitively depended on the density of Ag colloids and the wetting behavior of the glass phase [26]. The specific contact resistance of high efficiency p- and n-type cells was found in the same range of about 5 mΩ cm^2.

For n-type cells contacted with paste Ag–Al, the addition of Al to the Ag paste yielding a more pronounced wetting of the Si emitter by the glass phase and a high density of metallic Ag colloids in the glass layer. The higher density of Ag colloids in the glass layer is correlated with the lowest specific contact and series resistance. These results have been supported by other groups for details see Refs. [107, 108, 109]. Therefore, we assume that the wetting behavior and the density of Ag colloids in the glass layer determine the contact resistance in a similar way as for p-type cells [26].

A significant difference to p-type cells is that the pyramidal Ag nanocrystals are not observed in n-type cells, whereas they are formed in p-type cells [26]. Therefore, it can be concluded that for n-type high-efficiency cells, pyramidal Ag nanocrystals are not necessary for a low contact resistance. In fact, a low contact resistance correlated with a more pronounced wetting of the glass phase together with a high density of Ag colloids in the glass layer. Liang et al. suggested that for n-type cells the nucleation and growth of Ag nanocrystals is unfavorable for optimally fired cells [108]. Recently, they reported the formation of pyramidal shaped Ag nanocrystals only in overfired cells and observed a significant decrease of V_{OC} as compared to optimally fired cells [109]. Therefore, the authors concluded that the decrease in V_{OC} is associated with the intrusion of the pyramidal Ag nanocrystals at the Si emitter surface [109]. This is one convincing argument why pyramidal shaped Ag nanocrystals are not necessary for contacts yielding low contact resistance.

Furthermore, for cells contacted with paste Ag–Al the series resistance was only weakly dependent on temperature, as typically seen for alloys. However, cells contacted with Ag paste yielded a significantly increased series resistance as compared to cells contacted with paste Ag–Al. For such cells, the temperature dependent series resistance was large but also more strongly temperature dependent. In summary, these results prove that for achieving a low contact resistance in n-type cells, the wetting behavior and the density of Ag colloids in the glass layer play a decisive role, rather than the direct contacts between pyramidal Ag nanocrystals and the bulk Ag of the finger. A similar result was found for p-type cells [26].

4.4.3 Possible current paths of front side contacts

In the literature several models have been proposed to explain the relevant current paths for the front side metallization of Si solar cells, however, no conclusive picture has been drawn yet for B doped emitters [23, 24, 25, 91, 108]. There is experimental evidence that the glass layer contributes to the current: under FGA treatment a significant reduction of the contact resistance was seen by several groups [77, 80]. FGA treatment significantly reduces the contact resistance, due to the reduction of the metal oxides, i.e. PbO to Pb and, therefore, the conductivity of the glass layer increases [80]. However,

FGA because of oxygen vacancies weaken the adhesion of the gridline. The glass is assumed to be insulating by several authors [24], however, this approach appears too rigid. Indeed we believe that FGA treatment will create oxygen vacancies in the glass layer and might yield a moderately conductive semiconductor instead of an insulator. Even the untreated glass might be semiconducting rather than insulating considering the rapid thermal annealing processes usually applied. The point defect equilibrium at high temperatures will be quenched in yielding semiconducting material.

A high density of Ag colloids was found for cells with low contact resistance, both for n-type and p-type cells, and suggest that also for n-type cells a three-dimensional percolative charge transport through the glass layer is assisted by the presence of metallic Ag colloids [26]. It appears that the same microstructure is responsible for a reduced contact resistance, both in n-type and p-type cells, respectively. Therefore, we propose a percolation model, both for n- and p-type cells, in which Ag colloids present in the glass layer generate current filaments with reduced resistivity. The percolation model specifies a minimum volume fraction of Ag colloids, i.e. 15 %, necessary to carry the majority of the current through the glass layer by the filaments containing Ag colloids [26, 27].

4.5 Conclusions

In this work, we present a detailed analysis of microstructure, chemical composition and the temperature dependent series resistance of screen printed front side contacts on B doped emitters reaching maximum efficiencies of 20.0 %. Adding Al to the Ag paste yielded a lower specific contact resistance, series resistance and hence the higher efficiency. Microstructural analysis of such cells revealed a more pronounced wetting of the glass layer and a high density of Ag colloids, i.e. 70 colloids $/\mu m^2$ as determined from SEM micrographs for cells contacted with paste Ag–Al. From this, it was concluded that the specific contact resistance decreases as the density of Ag colloids increases in the glass layer. For cells contacted with paste Ag, a smaller density of Ag colloids, i.e. 15 colloids $/\mu m^2$, was observed in the glass layer and is responsible for the higher specific contact and series resistance. The chemical composition of the glass layer was measured quantitatively: (i) for cells contacted with paste Ag–Al 1 at.% of Al was determined, (ii) B and P could not be detected in the glass layer and were below the detection limit for n-type cells. In high-efficiency p-type cells B and P could be detected in the glass layer.

For both pastes, pyramidal and lens shaped Ag nanocrystals were not formed at the Si surface, different to p-type cells. As a result, the formation of pyramidal Ag nanocrystals is not needed for achieving a low contact resistance, consistent with more recent results of the literature [25, 26, 60, 108]. Additionally, cells contacted with paste Ag–Al yielded a small series resistance, similar to high-efficiency p-type contacts, but weakly temperature dependent. Cells contacted with Ag paste yielded a significantly higher series resistance, which increased linearly with temperature. The presence of a residual SiN_X layer at the contact interface avoided the formation of Ag/Al spikes at the Si surface and the SiN_x layer acts as a protecting layer. Despite a complex Si/metallization contact interface, a high density of Ag colloids was found for cells with low specific contact resistance, both for n- and p-type cells. This suggests that also for n-type cells a three dimensional percolative charge transport through the glass layer is relevant and assisted by the presence of metallic Ag colloids.

Chapter 5

High-efficiency, single-crystalline, p- and n-type Si solar cells: Microstructure and chemical analysis of the glass layer [110]

5.1 Background

For standard screen printing technology, commercially available front side pastes (FSP) are mainly used for contacting phosphorous (P) and boron (B) doped emitters [23, 24, 25, 26, 59, 60, 64, 68, 78, 85, 89, 90, 91, 101, 109]. The FSP typically consist of silver (Ag) powders, glass frits, some organic binders and small amount of metallic additives and dopants such as zinc (Zn), aluminium (Al), titanium (Ti), B and P [23, 64, 78]. Due to the given chemical complexity, the exact composition of these pastes particularly the metallic additives contents and its effect on the contact quality is largely unknown.

The contact formation and phase forming reactions are given in Refs. [23, 64, 111]. Previous studies have shown that the front side Si/metallization interface consists of a Si emitter embedded with Ag nanocrystals [25, 26, 59, 60, 85, 109], a glass layer typically <1 μm thick that contains a high density of nano-Ag colloids and on top of it a bulk metallization finger [25, 26, 59, 60, 85, 109]. Depending on the chemical composition of the paste and firing conditions, microstructural features such as continuous or discontinuous wetting of the glass phase at the Si emitter and density of nano-Ag colloids can have a significant impact on the contact resistance and hence the efficiency of the cell.

In the literature, several models have been reported [23, 24, 67, 73] considering the current path. Pyramidal Ag nanocrystals, 100 nm, in size, at the Si emitter were considered as essential together with tunneling through a thin glass layer. These models assumed that the glass layer was insulating and that tunneling might play a role. Table 5.1 summarizes an overview of the different models and their key statements published in the literature. In [26, 60, 85] we could prove that pyramidal Ag nanocrystals are not directly linked to a low contact resistance and that no evidence exists that the glass layer would be insulating. Tunneling in a rigid sense occurs over barriers usually only a few nm thick. These thin barriers are not present in the glass layers and, therefore, these models do not describe the current path correctly.

The understanding of the formation of Ag nanocrystals in the literature is ambiguous, the effect of the glass chemistry and firing conditions on cell properties has not been carried out systematically. We found a systematic and convincing understanding for the formation of Ag nanocrystals based on our experimental findings and based on physical properties of the relevant material, i.e. Si. Si yields anisotropic surface properties, which strongly influence the electrical properties of interfaces [26]. This is now well known from Schottky barriers [15] for which it took decades to understand the physics correctly. A similar problem we have with the screen printing metallization contacts [26].

There are four main microstructural findings summarized in our papers:

(i) Formation of Ag nanocrystals depends on the surface orientation of the Si [26, 60].

(ii) $< 100 >$ and $< 111 >$ Si surfaces yield different shapes for the Ag nanocrystals: pyramidal for $< 100 >$ and flat or pancake like for $< 111 >$ oriented Si [26, 60].

(iii) n-type cells with B doped emitters do not show pyramidal Ag nanocrystals, independent of the paste chemistry and firing conditions, the reason for this has been explained in Ref. [85]. Such cells, however, yield a low contact resistance [85].

(iv) Textured $< 100 >$ Si cells have predominantly $< 111 >$ oriented surfaces and pyramidal Ag nanocrystals appear only at the edges of the Si pyramids [26, 60].

Combining with electrical properties we concluded three additional findings: (v) Planar $< 100 >$ Si cells yield pyramidal Ag nanocrystals and high contact resistances [26, 60].

(vi) Planar $< 111 >$ Si cells yield flat, pancake like Ag nanocrystals and low contact resistances [26, 60].

(vii) In summary, pyramidal Ag nanocrystals are not considered be relevant for achieving low contact resistance. It is the shape of the nanocrystals that makes the difference, flat shaped is the more favorable shape, independent from paste chemistry and firing conditions.

Paste chemistry and firing conditions are important for the wetting behavior and, therefore, also for the series and contact resistance, it will however, not affect the properties of the Si metallization interface determined as outlined above. It means that e.g. paste chemistry and firing conditions cannot generate pyramidal nanocrystals on $< 111 >$ Si surfaces because this would contradict crystallographic arguments of the etching. Also independent of paste chemistry and firing conditions the strong anisotropy of the Si surface energy has to be taken into account: flat Ag nanocrystals will always appear on planar $< 111 >$ Si surfaces, whereas pyramidal shaped will appear on $< 100 >$ Si surfaces. This is also based on a crystallographic argument: $< 111 >$ are close packed planes in fcc structures. In summary, pastes that show favorable wetting behavior due to their chemistry and firing condition generate a higher interface area that is electrically active and thus lower the contact resistance.

Recently, it has been reported that a more prounounced wetting of the paste and a high density of nano-Ag colloids in the glass layer serves as quality criterion for achieving a low contact resistance [25, 26, 59, 60, 85, 109]. The density of such nano-Ag colloids in the glass layer plays a key role for the charge transport through the glass layer [26, 27, 85]. Since the resistivity of the glass layer is assumed to be significantly lower with nano-Ag colloids present in the glass layer and based on that a percolative charge transport model has been introduced [26, 27, 85].

There are few experimental evidences that show that the glass layer itself contributes to the current conduction: forming gas annealing (FGA) treatment as reported by a number of groups had significantly improved both the contact resistance and conductivity of the glass layer [64, 76, 77, 80, 112]. Also, the rapid thermal annealing process introduces oxygen vacancies in the glass layer. Since the high-temperature firing process was applied for the screen printing and oxygen vacancies are formed at high temperatures [113] and will be partially preserved by a rapid thermal annealing at room temperature. Together with oxygen vacancies charge carriers are being generated and might yield a moderately semiconducting glass layer instead of an insulating.

The electrical resistivity of glasses with different compositions was investigated by Zhang et al. [114] with respect to the band gap of the glass and contact resistance values of about $1 \, \Omega \, cm^2$ were achieved for such contacts. This shows the importance of monitoring the chemical composition of the glass

Author	Citation	Proposed model
Schubert et al.	[23]	"Current transport via sparsely distributed direct interconnections between the Ag crystallites and the Ag bulk or via a tunneling through the modified glass layer between the Ag crystallites and the Ag bulk of the finger"
Ballif et al.	[24]	"Current flow from the emitter into the contact is not uniform, but occurs via a few isolated Ag crystallites that are directly connected to the Ag bulk of the contact, or, more likely, by tunneling through ultrathin glass layers"
Li et al.	[25]	"Microstructural observations suggest that a tunneling mechanism (likely assisted by nano-Ag colloids) is responsible for current extraction"
Kontermann et al.	[67]	"Silver crystals at the interface of silver thick film contacts play a major role for the current transport across such contacts, as only few crystals are in direct contact with the contact bulk"
Cabrera et al.	[73]	"Directly connected Ag crystallites at the pyramid tops play a major role in the solar cell's current conduction, while less current flows through the Ag crystallites separated from the silver finger by the glass and the nano-Ag colloids contained within the glass "

Table 5.1: Overview of the different models published in the literature.

layer for achieving lower contact resistances.

A number of papers were published underlying the effect of the glass frit chemistry, Ag particle size and influence of the firing conditions on the microstructural and electrical properties of the cells [25, 76, 77, 78, 115]. Although, the presence and significance of the glass layer was identified long time ago [23, 24, 78], the chemical analysis of the glass layer is hardly found in the literature, particularly important is the quantitative chemical analysis of the glass layer. It even appears that a certain composition is assigned to the glass layer [23, 24, 76], which we will prove not to be the case. The glass phase contained Si, Pb, and O as main constituents wherein Zn, Ti, Ag and other elements were dispersed in the glass layer [26, 60, 85].

In the present study, we take a correlative approach by applying both the SEM-EDX and analytical TEM-EDX spectroscopy in order to quantify the chemistry and the microstructure of the glass layer on a sub-μm scale. By this approach, we obtained unprecedented insights about the role of the glass layer and established a cross-correlation to the electrical losses across the contact interface. Dark-field images in combination with diffraction patterns were applied to investigate the structural features of the glass layer i.e. other precipitates on a smaller length scale. We studied two p-type and one n-type cells processed with different front side metallization pastes. The quantitative chemical analysis of the glass layer on a sub-μm scale yields new possibilities for understanding and optimizing the

chemical composition of the glass layer and hence the efficiency of the solar cell.

5.2 Experimental details

5.2.1 Solar cells processing and electrical characterization

In this study, p-type textured cells were processed on Cz grown $< 100 >$ Si wafers with P doped emitters. Details of the solar cells processing of p-type cells are described in Refs. [26, 59, 60]. Large area (15.6×15.6 cm^2) n-type PERT (Passivated Emitter Rear Totally Diffused) cells with B doped emitters were fabricated on Cz grown $< 100 >$ Si grown wafers with base doping of 3 Ω-cm. For details see Refs. [85, 98]. Cells #1 and #2 with P doped emitters (p-type) were contacted with two different front side metallization paste FSP1 and FSP2, respectively, while cell #3 with B doped emitter (n-type) was processed with an AgAl paste. All cells were optimally fired at their set peak temperatures (for details see Table 5.2).

Cell	Solar cell	Paste	T_{FFO} [°C]	η (%)	ρ_c [$m\Omega.cm^2$]
#1	p-type Si	FSP1	900	16.9	21
#2	p-type Si	FSP2	900	17.8	4.7
#3	n-type Si	AgAl	830	19.96	< 4

Table 5.2: Process parameters and electrical results of the large cell wafer (15.6×15.6 cm^2) such as firing temperature T_{FFO} and efficiency η are summarized in the table. These measurements were carried out by a commercial solar cell tester at Institute for Solar Energy (ISE) Fraunhofer for p-type cells and ISC-Konstanz for n-type cells. Specific contact resistance was measured on small sized cells by the TLM method.

The electrical properties and processing parameters of cells are listed in Table 5.2. Cells #1 and #2 contacted with front side paste FSP1 and FSP2 yielded maximum efficiencies of 16.9% and 17.8%, respectively, while cell #3 contacted with an AgAl paste yielded the highest efficiency of about 20%. In addition, contact resistance measurements were carried out on small stripes typically 1×1.5 cm^2 in size by the TLM (transmission line model) method. Cell #1 showed the highest contact resistance of 20 mΩ cm^2 whereas the contact resistance of cells #2 and #3 was smaller than 5 mΩ cm^2.

5.2.2 SEM and TEM specimen preparation and strategy for quantitative chemical analysis

Samples were prepared by conventional mechanical grinding followed by polishing and ion-milling steps and analyzed in both plan view and cross-section, for details see Refs. [26, 59, 60, 85]. SEM EDX analyses was carried out at low primary energy to improve the lateral resolution of the method, typically a primary energy of 5 keV was selected. A detailed investigation of the microstructural and chemical analysis of the glass layer was carried out by TEM-EDX. The resolution in TEM is significantly better than in the SEM and best suited to precisely measure the glass layer. TEM-EDX spectroscopy is the method of choice for quantitative chemical analysis because of its high-lateral resolution and detection limit in the range of 1 at.%.

Dark-field images in combination with diffraction patterns were applied to investigate the structural features of the glass layer. To investigate the different phases presented at the contact interface, we

used superimposed energy-filtered TEM (EF-TEM) imaging techniques (referred to as RGB imaging) by making a colorful phase map of the area under investigation. RGB imaging was performed by acquiring three EF-TEM images at energy losses of 16 eV (Si plasmon peak), 24 eV (SiO_2 plasmon peak, Ag plasmon peak, Pb-O_{45} edge) and 32 eV (2nd Si plasmon peak) with an energy slit aperture of 5 eV width. Then, the three EF-TEM images were superimposed by assigning a false color to each of the EF-TEM image as 16 eV (Red), 24 eV (Green) and 32 eV (Blue) to yield a superimposed EF-TEM or RGB image. High-magnification bright and dark-field images of the glass layer were acquired with an energy slit of 10 eV. Diffraction patterns were acquired with a selected areas electron diffraction of about 750 nm in size.

The TEM is equipped with a LaB_6 filament, typical beam diameter of about 30 nm, an EDX detector and a low-background specimen holder for chemical analysis with an energy resolution of 136 eV at the $Mn - K_\alpha$ line. All acquired EDX spectra were quantitatively analyzed by applying the Cliff-Lorimer k factor method as described in Refs. [36, 57, 58]. EDX spectra were acquired with a spot size of 32 nm and an acquisition time of 300 s with a stray aperture to avoid stray radiation and to improve the detection limit. The counts of the Si peak were larger than 4000 for EDX spectra acquired in the glass layer.

5.3   Results

For high-efficiency cells (18.0% for p-type and 20% for n-type cells) we observed similar microstructure of the glass layer (Figure 5.1 c and d), i.e. a matrix with a high density of Ag colloids covering the Si emitter and the Ag bulk of the metallization finger. Besides the Ag colloids, smaller precipitates were found in the glass layer.

In addition, the temperature dependent series resistance (Figure 5.1a and b) is similar for n- and p-type cells, both in absolute values and with respect to the temperature dependence. Series resistance measurements were carried out on small cells typically 1×1 cm^2 under dark conditions. The series resistance was only weakly temperature dependent for both high-efficiency p- and n-type cells. We assume that the charge transport is limited by the glass layer which contains a high density of Ag colloids and other precipitates. In addition, p- and n-type cells showed a low series resistance, lower than 60 mΩ. The reason for this low series resistance was explained in [85]: (i) dark measurements use carriers injected into the contacts and the current crossing the junction is in-homogenous and flows only underneath the contacts [85]. In case of illuminated measurements, the current crossing the junction is more uniform and flows along the emitter to the contacts. This current will be affected by the sheet resistance of the emitter. In summary, in the dark condition most of the current crosses the junction underneath the contact and therefore yields a low series resistance as compared to cells under illumination [85], for which a larger series resistance should be measured.

As a third point, the chemical composition measured by EDX spectroscopy (Figure 5.1e and f) of the glass layer both for n- and p-type cells is similar. Therefore, it is concluded that the microstructure of the glass layer determines the series and contact resistance of the front side metallization. This is the main outcome of the detailed analyses we have carried out [26, 60, 85].

These investigations also proved the relevance of the glass layer for the current path for both n- and p-type cells. Low-efficiency cells showed significantly different microstructure and series resistance

at the metallization interface.

Temperature dependent series resistance

SEM-microstructure
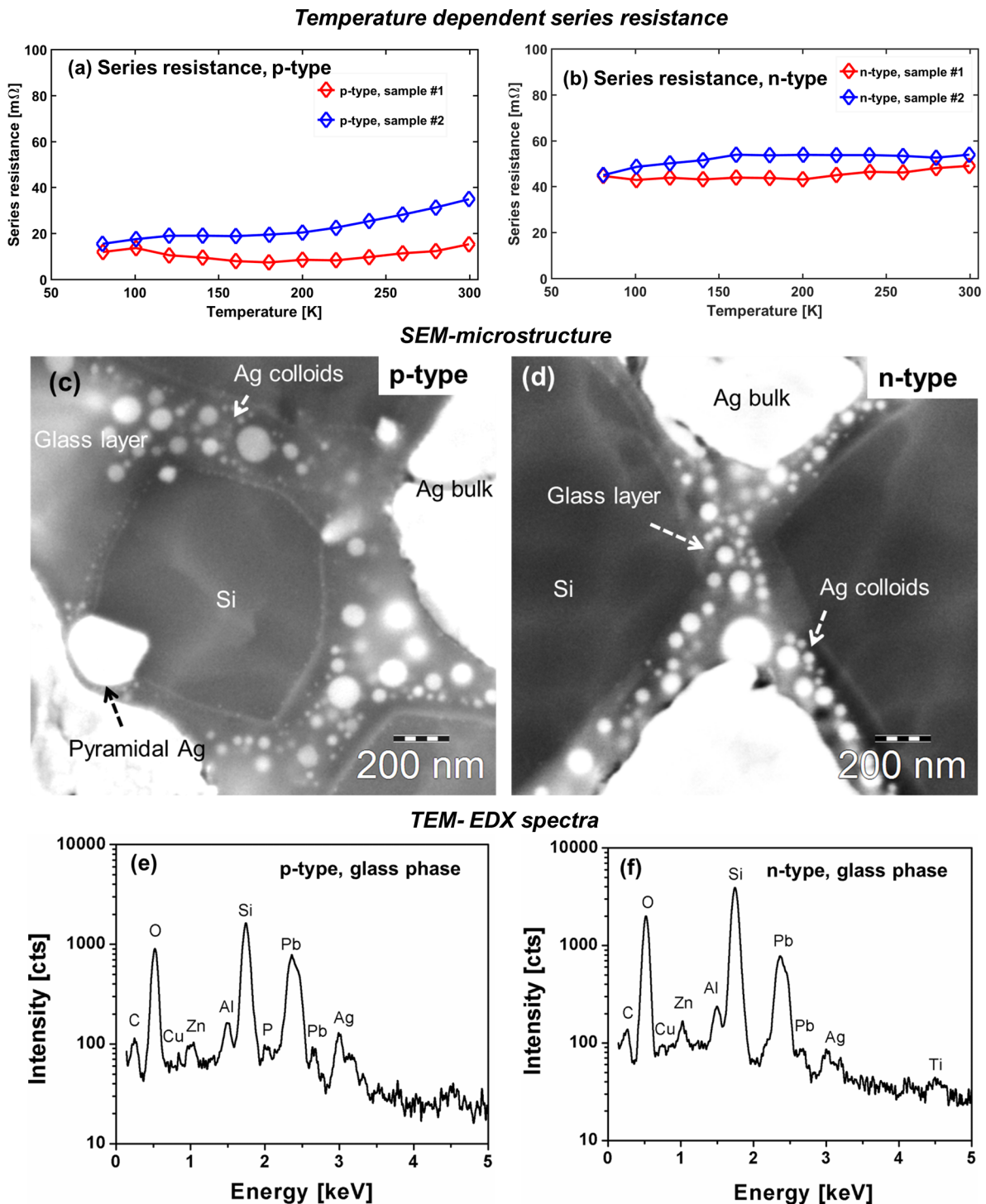
TEM- EDX spectra

Figure 5.1: shows the essential features of high-efficiency p- and n-type cells: (a−b) temperature dependent series resistance, (c−d) microstructure at the Si/metallization interface by SEM and (e−f) TEM-EDX spectra of the glass layer.

In our previous work [27], n- and p- type cells were investigated as shown in Figure 5.2: a low Ag colloid density (c, d) yielded a high contact resistance and a high colloid density (a, b) was linked to a low contact resistance. This confirms that high-efficiency cells always yield the lowest contact resistances and a higher density of Ag colloids in the glass layer. Based on the above arguments and chemical analysis of the previous work (see Table 5.3) we assume that the glass layer is a dirty

semiconductor. "Dirty semiconductor" means that the glass contains precipitates on a smaller length scale as compared to the Ag colloids and point defects such as impurities and oxygen vacancies yielding a semiconducting behavior.
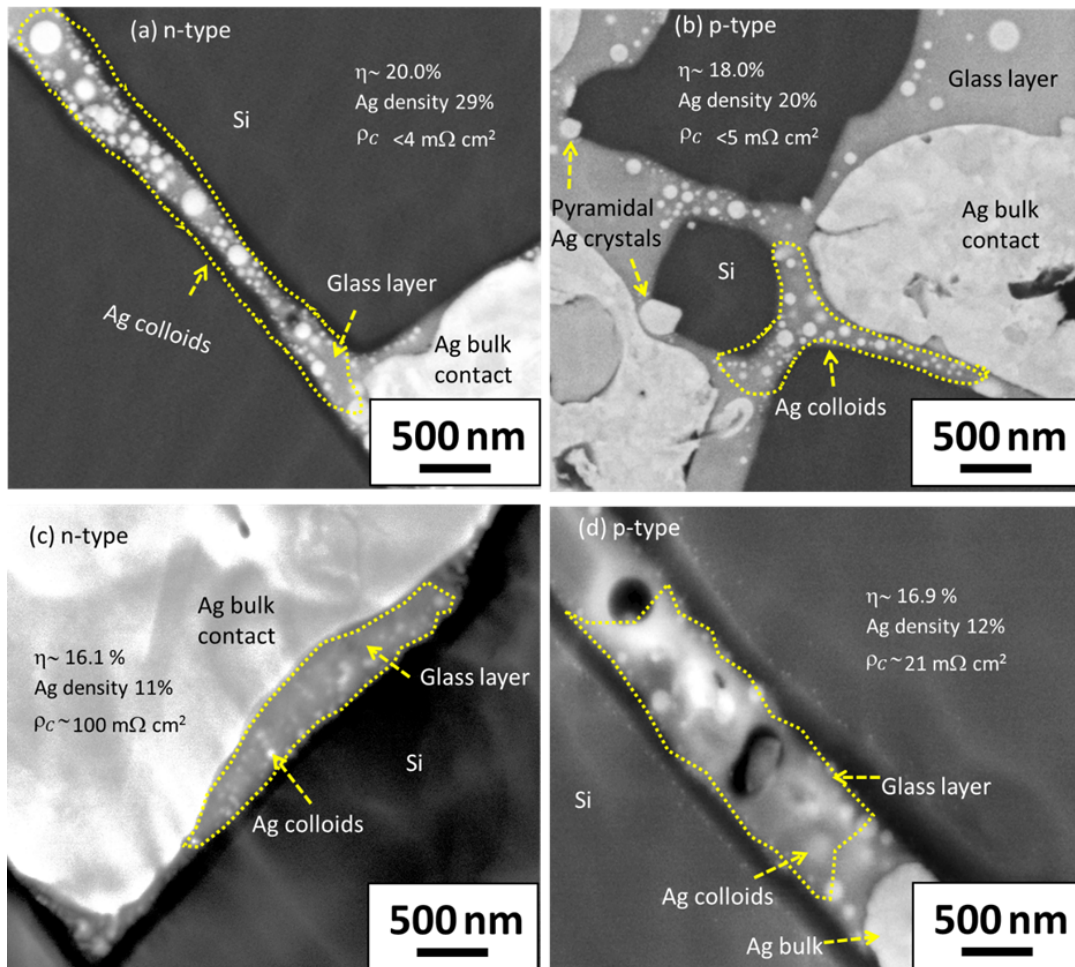
Figure 5.2: Plan-view SEM images of the Si/metallization interface of n-type (a, c) and p-type (b, d) solar cells. The higher density of Ag colloids in the glass layer is clearly visible for the high-efficiency cells (a, b) [27]

Moreover, screen printed front side pastes are subjected to a rapid thermal annealing process that might introduce oxygen vacancies instead of ideal glass layer which yields a stoichiometric composition. Oxygen vacancies are known to generate n-type conductivity in oxides [113]. From this starting point, a percolation model has been proposed [27], in which the microstructural features were introduced and the main features of the model are: (i) a finite electrical resistance of the glass layer and, (ii) colloids reducing the resistance of the individual current paths in a simple geometrical sense.

Different cells that were identically processed up to the front side metallization were screen printed with different pastes yielding significantly different contact resistances and efficiencies (Table 5.2). The glass layer of such cells was investigated by EDX spectroscopy in the SEM and for a sub-group also by EDX spectroscopy in the TEM (Table 5.3). Paste specific features, usually not transmitted by the paste manufacturer, but can be identified in the glass layer (Table 5.4): (i) a Zn-rich paste yielded also a Zn-rich glass layer and (ii) an Al-free paste did not show Al in the EDX spectra of the glass layer. EDX spectroscopy is, therefore, very well suited to identify chemically specific properties of the glass layer, even when the paste features are not known or transmitted by the paste manufac-

S.N	Solar cell	Paste	SEM-EDX	TEM-EDX	Reference
1	p-type Si	FSP1	x	This work	[26, 60]
2	p-type Si	FSP1	x	x	[26, 60]
3	p-type Si	FSP2	x	This work	[26, 60]
4	n-type Si	AgAl	x	This work	[85]
5	n-type Si	AgAl	x	-	[85]
6	n-type Si	Ag	x	-	[85]

Table 5.3: Overview of the chemical analysis of p- and n-type cells with processed different front side pastes and investigated by SEM-EDX and TEM-EDX spectroscopy as published in our previous work.

turer. In summary, the benefit of such an analysis is twofold: (i) with respect to technology, i.e. the glass layer chemical composition depends on the properties of the paste and the firing condition and, (ii) with respect to the percolation model, metallic impurities affect the resistance of the glass layer. In addition, metallic precipitates will be formed in the glass layer that reduces the total contact resistance.

Solar cell	Paste features	SEM-EDX	TEM-EDX
p-type, cell #1	Zn rich	x	x
n-type, cell #3	Contains Al	x	x

Table 5.4: Summarizes the paste features such as Zn rich and containing Al in the glass layer as identified by SEM and TEM-EDX microanalysis.

5.3.1 Microstructural analysis of the glass layer by SEM and TEM

The microstructure of the glass layer at the Si/metallization interface of p- and n-type cells was studied by SEM and TEM based methods. Figure 5.3a−c show high-resolution SEM micrographs of the glass layer obtained on p- and n-type cells contacted with different front side metallization pastes.
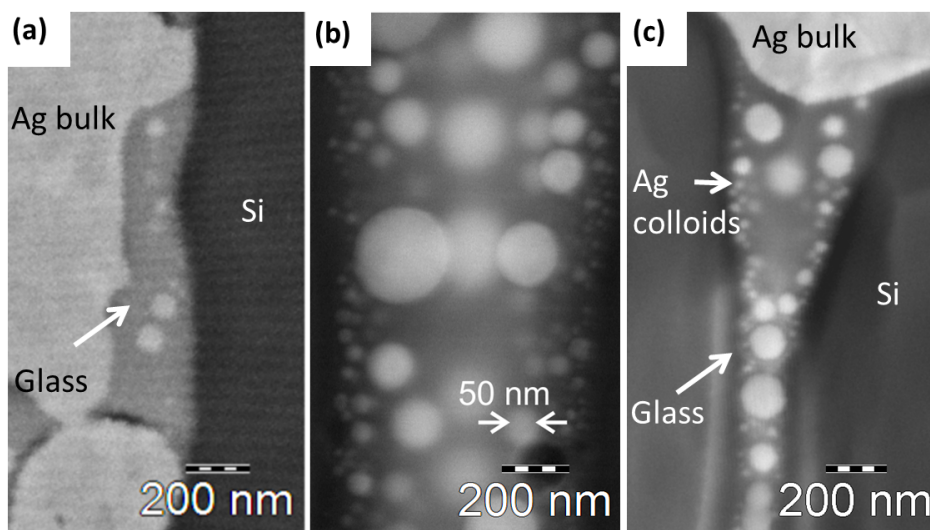
Figure 5.3: High-resolution scanning electron microscopy images of the glass layer: (a) cell #1 contacted with paste FSP1, (b) cell #2 contacted with paste FSP2 and, (c) cell #3 contacted with paste AgAl.

Cell #1 contacted with paste FSP1 showed a discontinuous wetting of the Si emitter by the glass layer and a small density of Ag nano colloids in the glass layer (Figure 5.3a). On the other hand, cell #2 contacted with paste FSP2 (see Figure 5.3b) and cell #3 (see Figure 5.3c) contacted with an AgAl paste yielded a more pronounced wetting of the glass layer and a high density of Ag colloids in the glass layer. From SEM images the diameters of Ag colloids were measured between $5-200$ nm. The thickness of the glass layer was estimated between few tens of nm up to 1μm.

A detailed description of the bright and dark-field images (see Figure A1) of the Si/metallization interface of cell #1 is given in the appendix A. The important features of cell #1 are: (i) a small density of Ag colloids in the glass layer, (ii) small pockets of the SiN_x layer at the Si/metallization interface and, (iii) Zn rich oxide phases in the glass layer.

Figure 5.4a is a low-magnification bright-field image of the Si/metallization contact interface of cell #2. Areas with and without SiN_X layer can be identified at the Si/metallization interface. The density of nano-Ag colloids (with sizes between 5 and 150 nm) is significantly increased in the glass layer of cell #2 (Figure 5.4a right side) as compared to cell #1.

Figure 5.4b is the corresponding dark-field image of the same region. Figure 5.4c$-$d are magnified parts of the glass layer. In Figure 5.4c besides the nano-Ag colloids, small precipitates of sizes <10 nm are present in the glass layer, however, their nature remains unclear due to their small size.
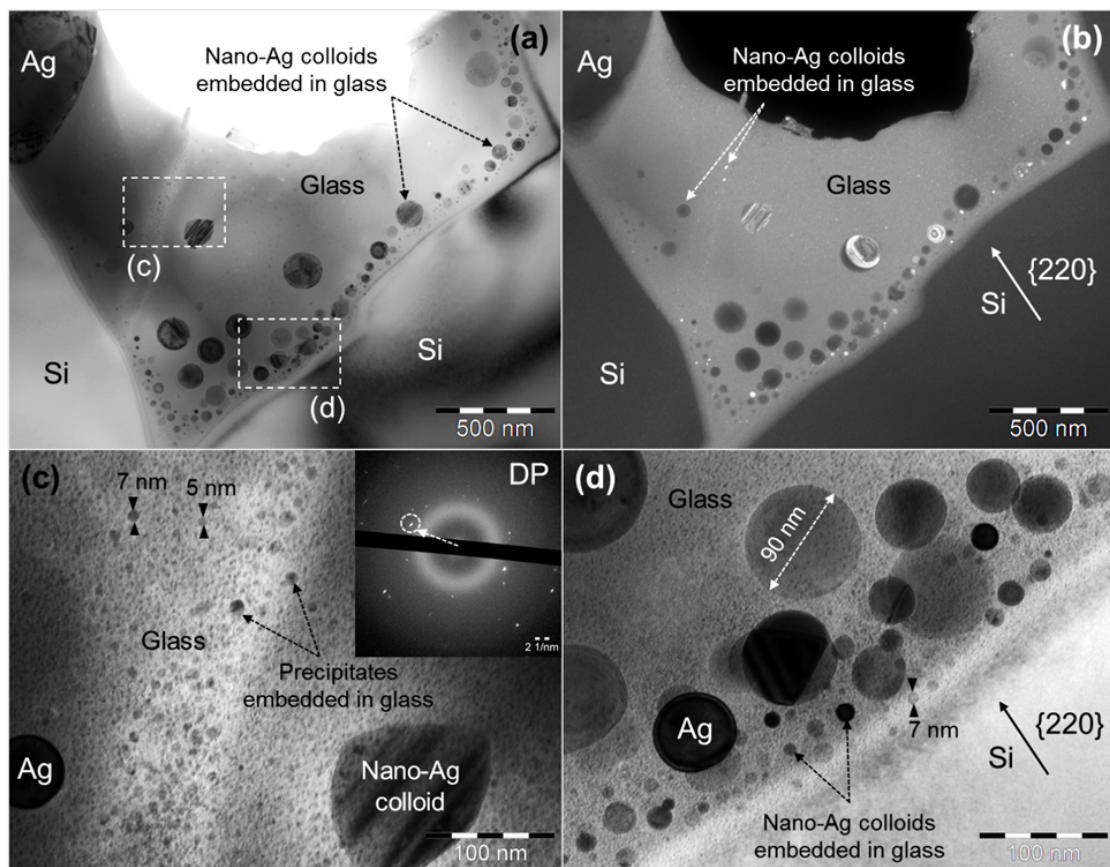
Figure 5.4: Low-magnification (a) bright-field, (b) dark-field images of cell #2 (p-type) in plan-view showing the contact interface, (c) and (d) high-magnification bright-field images of the respective rectangular areas marked in (a). Inset in (c) shows an electron diffraction pattern of the glass layer.

Diffraction patterns and dark-field images were obtained on the glass layer of cell #2 and are shown

in Figure 5.5a–d. Diffraction patterns were acquired with a selected area aperture of about 750 nm in size. The diffraction patterns contain 3 features: (i) amorphous circular structures, (ii) ring patterns due to precipitates in the glass and (iii) reflections of the mono-crystalline Si. Note the large number of reflections on ring structures in the pattern. The diffraction pattern can be interpreted as coming from an amorphous structure (glass) that contains crystalline precipitates. The circular shaped background in the diffraction patterns is due to the amorphous part of the glass layer. Ag (111) and (002) reflections and Si reflections were identified in the glass layer. Additional reflections were identified that belong to other precipitates than the Ag colloids. This is best seen in the corresponding dark-field images.

High-magnification dark field images (see Figure 5.5c–d) showed Ag colloids and other precipitates (<10 nm) dispersed in the glass layer (bright areas in Figure 5.5 b–d). The presence of precipitates also indicates that in the amorphous phase point defects, i.e. impurities, might be present.
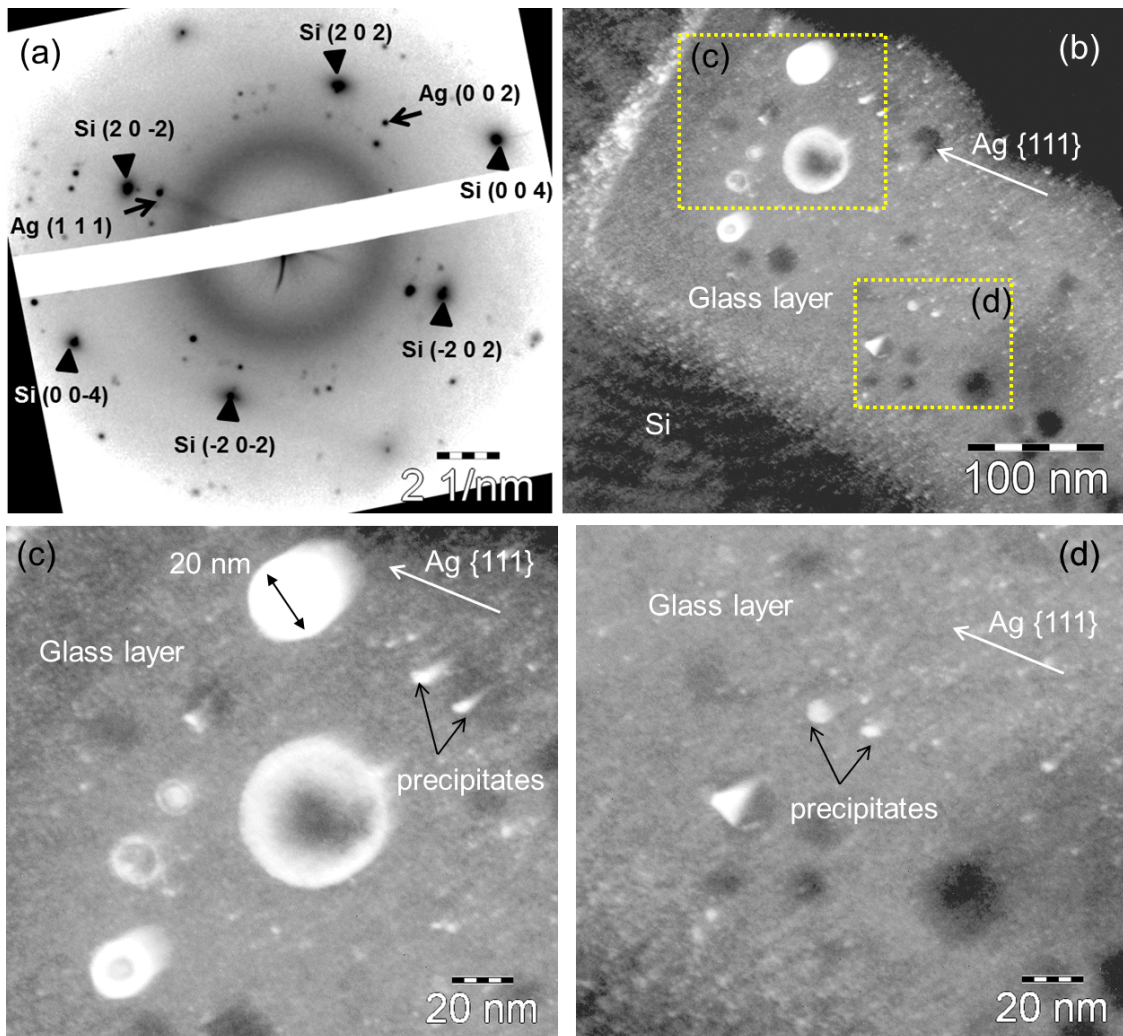
Figure 5.5: Diffraction pattern and dark-field images of cell #2 (p-type) obtained at the Si/glass contact region. Diffraction pattern confirms the presence of Ag reflections in the glass layer. (c–d) show the high-magnification images of the glass layer.

Figure 5.6a–b show the low-magnification bright and dark-field images of cell #3 obtained at the Si/metallization interface. The microstructure is very similar to the one observed for cell #2. A local opening of the SiN_X layer and high densities of nano-Ag colloids were observed in the glass layer.

Nano-Ag colloids sitting close the Si emitter surface are smaller in size as compared to colloids in the inner part of the glass layer.

Diffraction patterns (Figure 5.6c) and dark field images were acquired using Ag (111) reflection. They yielded small sized (10 nm) precipitates in the glass layer (see Figure 5.6b). These precipitates can be best seen in the thinner part of the glass layer. High-magnification images of the glass layer are shown in Figure 5.6d−g. The diameter of nano-Ag colloids was estimated between 5 and 250 nm. The larger nano-Ag colloids are crystalline in nature, as can be seen in Figure 5.6d.
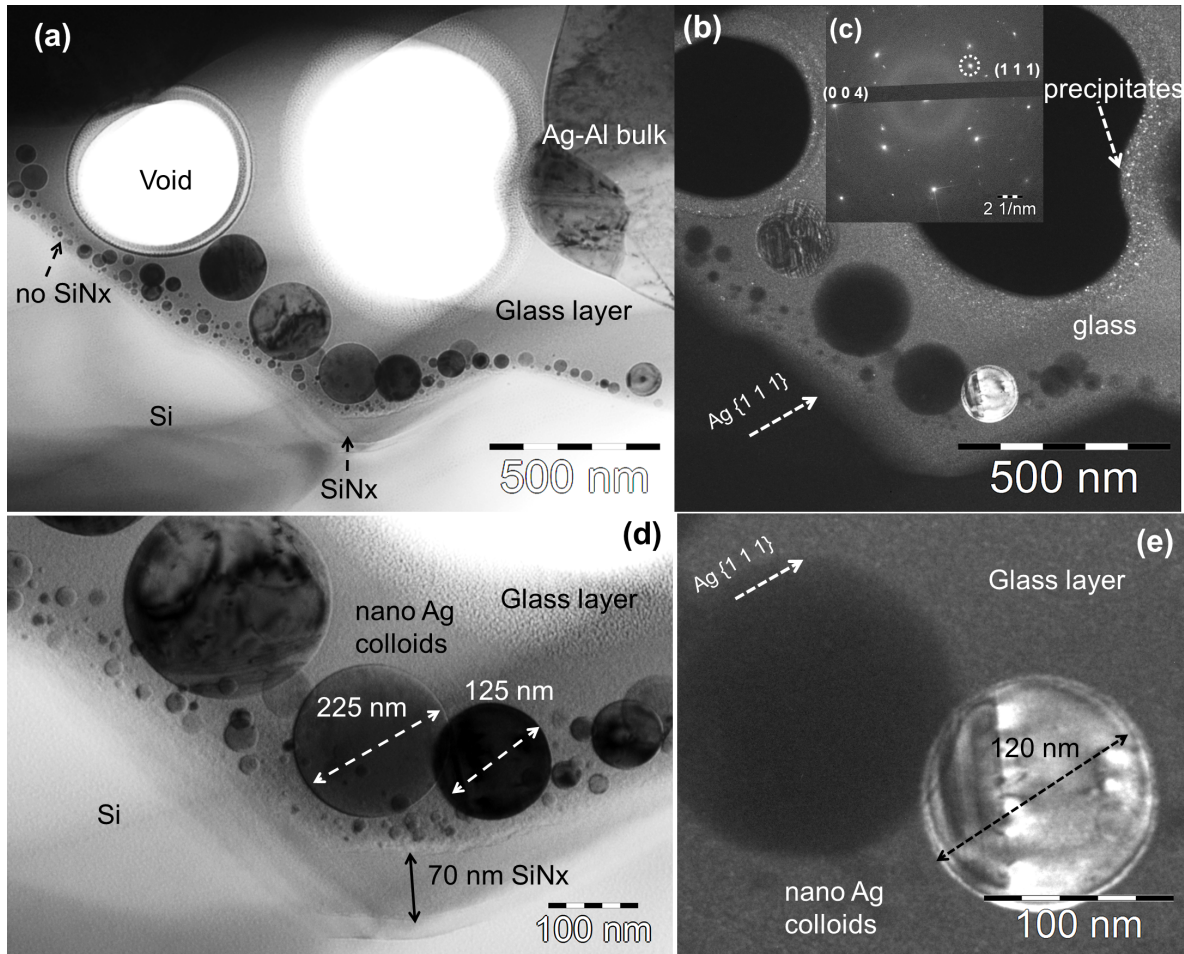
Figure 5.6: Low-magnification (a) bright-field and (b) dark-field image of cell #3 (n-type) acquired at the Si/metal contact interface. Inset (c) shows the diffraction pattern obtained at the Si/glass interface area. (d−e) high-magnification bright and dark-field images of the glass layer.

5.3.2 Phase mapping at the Si/metallization interface

In high-efficiency n and p-type cells, the emitter is covered by a 500 nm thick glass layer on top of which the bulk Ag is present. The microstructure at the metallization interface is complex and EF-TEM images are very suitable to effectively document the essential features of the microstructure by generating phase maps. The combined acquisition of EF-TEM images and EDX spectra turned out to be very useful for the phase mapping. Figure 5.7a−i show the superimposed energy-filtered (EF-) TEM images of cells #1, #2 and #3, acquired at three different energy losses of 16 eV, 24 eV and 32 eV. For each cell more than 5−10 different areas were investigated in detail. These images yield optimized contrast for the identification of the phases; Si emitter (pink), the nano-Ag colloids

(dark blue) and the glass layer (green). In a next step, these phases were quantitatively analyzed by TEM-EDX spectroscopy and spectra corresponding to each cell are shown in the appendix A.
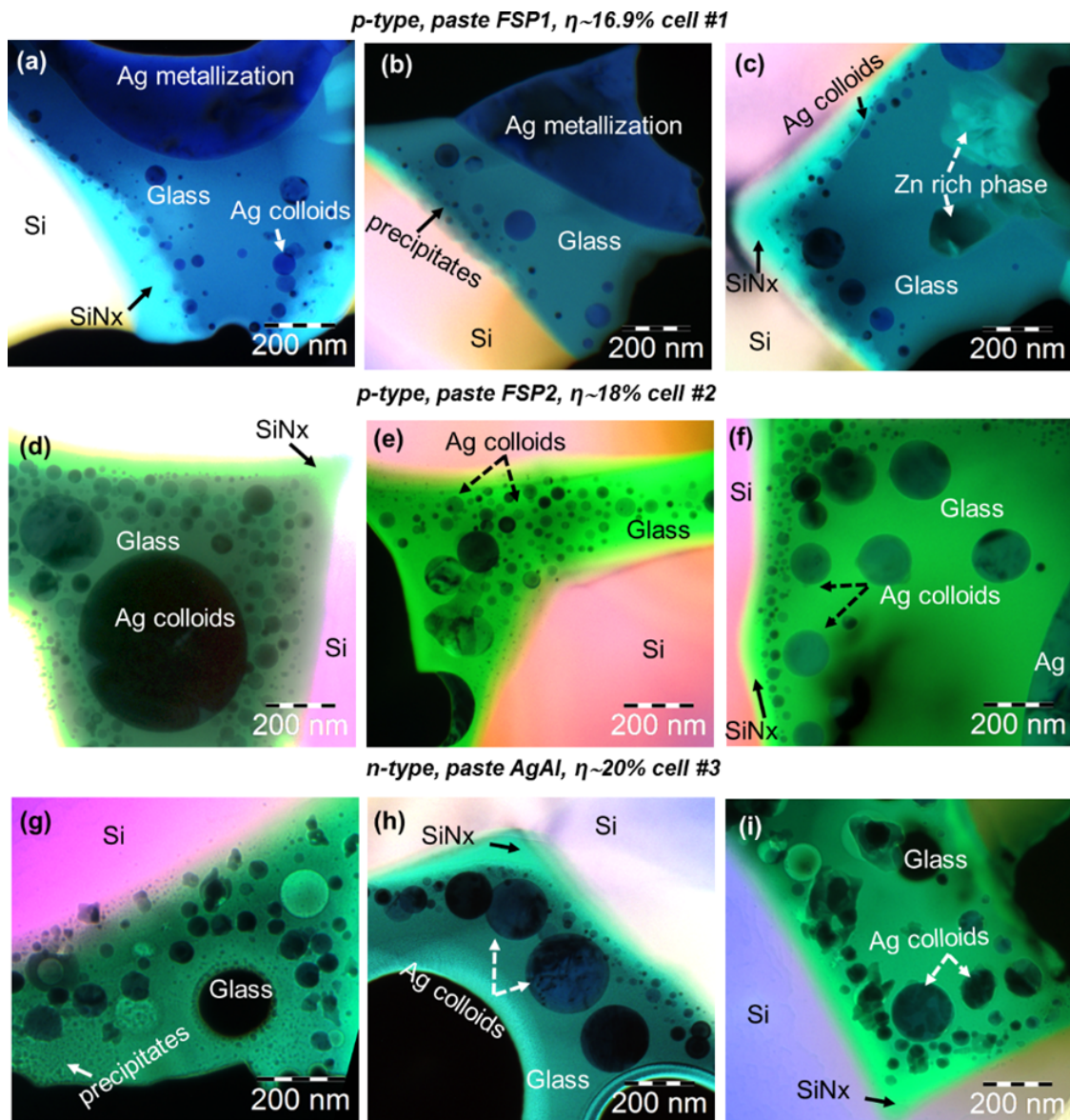
Figure 5.7: High-magnification EF-TEM images of the glass layer (a−c) p-type, cell #1, (d−f) p-type, cell #2 and (c) n-type, cell #3. Different phases such as Si emitter, a glass layer, SiN_X layer and Ag colloids/precipitates are identified at the Si/metallization interface.

The presence of a residual SiN_X layer (Figure 5.7a−c) is important for the contact interface analysis. For cell #1, only small pockets of the SiN_X (marked area in Figure 5.7a) layer were detected whereas for cells #2 (Figure 5.7d−f) and #3 (Figure 5.7g−i) a residual SiN_X layer was identified over a large area at the contact interface.

In some areas, the SiN_X was etched off completely and yielded a reduced density of the nano-Ag colloids in the glass layer. It even appears that the SiN_X layer triggers the density of nano-Ag colloids in the glass layer: with a SiN_X layer locally present, a larger density of nano-Ag colloids was observed. The presence of small precipitates and nano-Ag colloids could be observed in the glass layer. The density of Ag colloids/precipitates is much higher for cells #2 and #3 as compared to cell #1.

75

5.3.3 Quantitative chemical analysis of the glass layer by SEM-EDX spectroscopy

The quantitative chemical analysis of the glass layer of cells #1, #2 and #3 was carried out by SEM-EDX spectroscopy and is summarized in Table 5.5. SEM-EDX analysis of the glass layer is demanding because the thickness of the glass layer is typically less than $1\mu m$. Therefore, to reduce the lateral resolution of EDX, 5 keV accelerating voltage was chosen to keep the lateral resolution suitable for the chemical analysis of the glass layer, particularly for the quantification of the light elements O, N and some metallic impurities.

Glass layer	Si [at.%]	O [at.%]	Ag [at.%]	Zn [at.%]	Pb [at.%]	Al [at.%]
Cell #1, paste FSP1	*19.4*	64.0	3.4	*6.8*	6.4	-
Cell #2, paste FSP2	*28.5*	58.6	5.6	*1.06*	4.84	*1.4*
Cell #3, paste AgAl	*28.8*	59.6	4.0	*2.4*	4.0	*1.2*

Table 5.5: Quantitative chemical analysis of the glass layer of cells: #1 (p-type), #2 (p-type) and #3 (n-type) carried out by SEM-EDX spectroscopy. Quantitative analysis was done including oxygen and average chemical composition of the glass phase is summarized in the table.

Figure 5.8a−c show the spectra of cells #1, #2 and #3 plotted in a logarithmic scale to highlight elements with small mole fractions. The chemical composition of the glass layer consists of a Pb containing SiO_X matrix, while additives such as Ag, Zn, Al, Ti were dispersed in the glass layer [26, 60, 85]. For cells #2 and #3 Pb mole fractions (5−6 at.%) are in the similar range while a slightly higher Pb mole fraction (7 at.%) was observed in the glass layer of cell #1. Zn mole fractions of 6.8 at.% were detected in the glass layer of cell #1, whereas for cells #2 and #3, Zn mole fractions were in the range of 1−2 at.%. An Al mole fraction of 1 at.% was detected in the glass layer of cells #2 and #3, but Al was not detected in the glass layer of cell #1.

A boron (B) peak could be detected in the EDX spectrum of the glass phase of cell #1 (Figure 5.8a), while P was below the detection limit of the SEM-EDX spectroscopy. Only for cell # 2, a P peak could be detected in the glass layer (Figure 5.8b), and the B peak was below the detection limit. Also for cell #3 these elements (P and B) were below the detection limit of EDX.

In summary, for high-efficiency p- and n-type cells small mole fractions of Zn (1 at.%) and Al (1 at.%) were detected in the glass layer. Cells with large Zn (>5 at.%) mole fractions and the absence of Al mole fractions yielded a high contact resistances and a small density of nano-Ag colloids in the glass layer. P and B could be identified only in the glass layer of p-type cells, however, such elements were below the detection limit of the EDX for n-type cells.
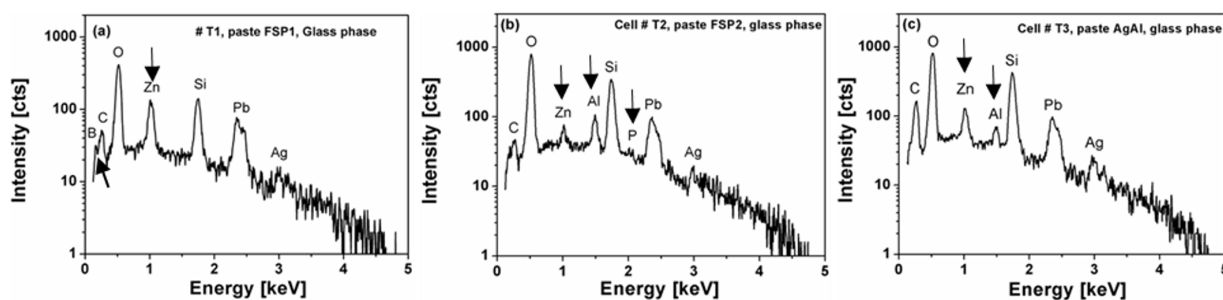
Figure 5.8: SEM-EDX spectra of the glass layer obtained on (a) p-type, cell #1 (b) p-type, cell #2 and (c) n-type, cell #3. All spectra were plotted on a logarithmic scale to highlight elements with small mole fractions.

5.3.4 Quantitative chemical analysis of the glass layer by analytical TEM-EDX spectroscopy

Further quantification of the glass layer was investigated by TEM-EDX spectroscopy, especially for the quantification of the additives (Pb, Zn, Al, and Ti) and dopant elements (P, B). TEM-EDX is best suited for the quantification of the glass layer. For all cells, $10-20$ spectra were acquired with a spot size of 32 nm with stray aperture inserted. By this approach, the minimum detectable mole fractions could be improved significantly [36]. Table 5.6 summarizes the chemical composition of the glass layer of cells #1, #2 and #3, respectively.

Glass layer	Si [at.%]	O [at.%]	Ag [at.%]	Zn [at.%]	Pb [at.%]	Ti [at.%]	Al [at.%]	P [at.%]
k-factor	1.00	2.25	1.76	1.54	3.04	1.09	1.03	0.99
Cell #1, paste FSP1	*28.71*	55.78	2.37	*4.58*	7.27	*1.29*	-	-
Cell #2, paste FSP2	*34.42*	54.78	2.45	*0.42*	6.47	*0.11*	1.02	*0.33*
Cell #3, paste AgAl	*36.60*	56.20	0.72	*0.44*	4.60	*0.12*	1.32	-

Table 5.6: Quantitative chemical analysis of the glass layer obtained on cells: #1 (p-type), #2 (p-type) and #3 (n-type) by EDX spectroscopy in TEM. Quantitative analysis was done including oxygen and average chemical composition of the glass phase is listed in the table.

Oxygen was included in the quantification of the glass layer and the spectra corresponding to each cell are shown in Figure 5.9a−c. The glass layer can be understood as a (SiO_X) Pb phase with a Si/Pb mole fraction ratio of 4 for cell #1 and the slightly higher ratio of 6 for cells #2 and #3. Consistent with the SEM results, only for cell #1 a significantly higher Zn mole fraction (5 at.%) was detected in the glass layer compared to cells #2 and #3 (< 1 at.%). The presence of higher Zn mole fractions yielded Zn rich oxide phases (Zn_2SiO_4) embedded in the glass layer as confirmed by EF-TEM images (Figure 5.7c).
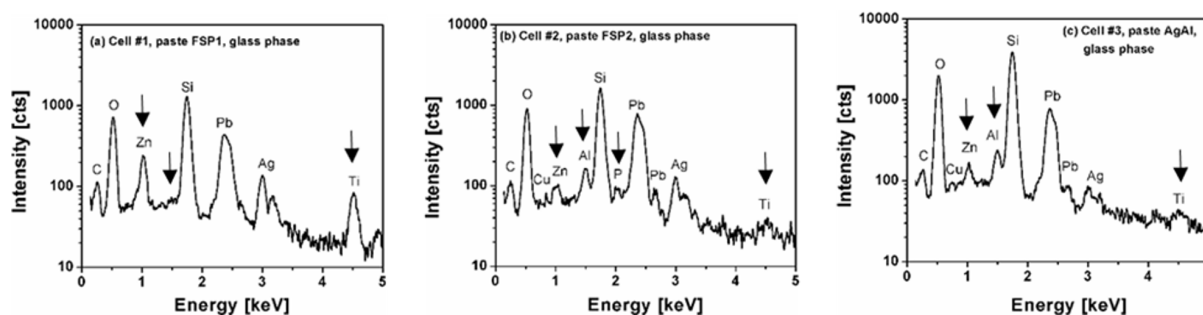
Figure 5.9: (a−c) TEM-EDX spectra of the glass layer of cells: (a) p-type, cell #1, (b) p-type, cell #2 and (c) n-type, cell #3, respectively plotted on a logarithmic scale in order to highlight elements with small mole fractions.

In a next step, O was excluded from the quantitative analysis of the glass layer to improve the minimum detectable mole fraction of the elements such as B, P, and Ti. The results are summarized in Table 5.7. Details of B and P peaks analysis by SEM and TEM-EDX spectroscopy are given in the appendix A.

Figure 5.10 shows a correlation diagram of SEM-EDX mole fractions versus TEM-EDX mole fractions of the glass layer plotted on a semi-logarithmic scale. This diagram correlates the quantitative SEM-

Glass layer	Si [at.%]	Ag [at.%]	Zn [at.%]	Pb [at.%]	Ti [at.%]	Al [at.%]	P [at.%]
k-factor	1.00	1.76	1.54	3.04	1.09	1.03	0.99
Cell #1, paste FSP1	*68.0*	4.26	*9.69*	15.22	*2.83*	-	-
Cell #2, paste FSP2	*74.22*	5.38	*1.24*	15.36	*0.22*	*2.77*	*0.81*
Cell #3, paste AgAl	*84.0*	1.82	*0.97*	10.09	*0.23*	*2.89*	-

Table 5.7: A detailed quantitative chemical analysis of the glass layer of cells: #1 (p-type), #2 (p-type) and #3 (n-type) was carried out by EDX spectroscopy in TEM. Oxygen was eliminated from the analysis to improve the quantification of other elements.

EDX data to quantitative TEM-EDX data for a certain microstructure, i.e. glass layer with Ag colloids and precipitates. The mole fractions values are very close in both measurements, i.e. TEM results follow SEM results. This result is not trivial since the acquisition conditions are very different. Since analysis in the SEM-EDX is much less tedious and widely spread than in the TEM, and therefore this result is of great practical value. Only for Ag and Zn we observed differences: SEM results show slightly higher mole fraction as compared to the TEM results.

In case of additives/impurity elements such as Ag, Zn, and Al SEM results showed higher mole fraction as compared to the TEM results. This is because of the poor resolution of the SEM. On the other hand TEM yielded more accurate mole fractions of the additives/impurity elements. The size of the EDX spot in TEM is 30 nm and yields more precise analysis of the glass layer, however, in SEM-EDX spectroscopy if the choice of right parameters such as low primary energy 5 keV was applied we could significantly improve the lateral resolution of SEM-EDX as shown in the correlation diagram. The lateral resolution of SEM-EDX at 20 keV, which is typically applied in the published literature is too poor and, therefore, unfavorable to investigate the glass layer.
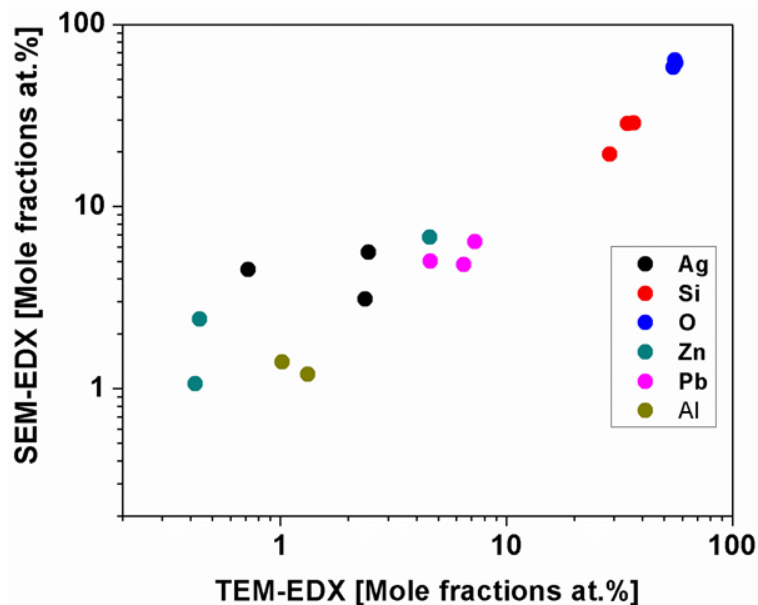
Figure 5.10: A log-log plot of correlation diagram of SEM-EDX mole fractions against TEM-EDX mole fractions measured in the glass layer of cell #1 (p-type), #2 (p-type) and cell #3 (n-type), respectively. Quantitative data of six different elements (Ag, Zn, O, Si, Al and Pb) are shown in the plot.

Additional correlation diagrams of Pb versus Si and Zn+Pb versus Si mole fractions of cells #1, #2 and

#3 are found in the appendix A. In the correlation diagram of Figure A6, it is evident that the glass layer is in-homogeneous with respect to its chemical composition. For both combinations, a negative correlation was observed between Pb and Si and Zn+Pb and Si mole fractions. This indicates that (Pb, Zn) and Si are negatively correlated and, therefore, Pb and Zn both substitute Si.

5.4   Discussion

Microstructure, structure-property correlation, and possible current paths were addressed both for p-type and n-type high-efficiency cells [26, 85]. As a major result, it was found that the microstructure of n-type and p-type high-efficiency cells are remarkably similar. The microstructure consists of a glass layer that is less than 1μm thick and embedded Ag colloids which have a volume fraction of up to 20% and bulk Ag fingers are arranged on top of the glass layer. In addition, structure-property correlation of high-efficiency n- and p-type cells yielded similar contact resistance, series resistance, and common features of the microstructure of the front side contacts, i.e. a glass layer containing high densities of Ag colloids [26, 85]. Only the formation of Ag nanocrystals at the Si emitter is different: in p-type cells Ag nanocrystals are formed, in n-type cells these nanocrystals do not appear [26, 85]. Since the series and contact resistance of high efficiency n-type and p-type cells are comparable it is concluded that (pyramidal shaped) Ag nanocrystals at the Si emitter are not necessary for yielding a low contact resistance. Instead, a high density of nano-Ag colloids in the glass is more relevant for a low contact resistance [85].

This conclusion contradicts Refs [23, 24, 67, 73] in which Ag nanocrystals are suggested to be relevant for the low contact resistance and authors suggested that they contribute significantly to the current path. However, our experimental results do not support this argument but indicated that the glass layer is essential for the current path and that the relevant understanding is a percolation transport model. The Ag colloids constitute current filaments with reduced resistance in the glass layer, thereby introducing a percolative current which is the basis of the proposed model [27]. This model was new and differs from the classical percolation model as it directly relies on the macroscopic resistance of these filaments, and in considering the matrix as semiconducting rather than insulating. The semiconducting matrix is the glass layer and its chemical composition and microstructure directly affect its electrical properties.

A second motivation for analyzing the glass layer in detail is due to the screen printing technology. The glass layer is a finger print of the used paste, as will be discussed below. It contains the elements of the paste and generates the precipitation process in which Ag colloids are formed. We gave two arguments why the analysis of the glass layer is important: (i) understanding the current path and (ii) understanding paste specific differences of the glass layers yielding different series and contact resistances. Despite the obvious importance of the glass layer hardly any analysis of its chemical composition has been carried out yet. Our results are the first quantitative analyses directly addressing its chemical composition.

5.4.1   Microstructure of the glass layer and contact resistance

A key question for understanding the electrical properties of the glass layer is to decide whether it is (i) an insulator or (ii) a semiconductor with significantly reduced resistivity as compared to an

insulator. Electrical measurements of the glass layer do not exist, therefore, microstructural analyses will be used to understand its electrical properties. Also, the temperature dependent measurements of the series resistance are essential for understanding the electrical properties of the glass layer [26, 85].

Microstructural features that would transform the insulator, i.e. stoichiometric, amorphous silicon oxide into a dirty semiconducting phase would be: impurities, i.e. point defects, and electrically conducting precipitates. EDX spectroscopy is able to measure the mole fraction of impurities beyond the detection limit, electron microscopy is able to image precipitates and determine their density. This has been done in great detail in this chapter. We acquired about $10-20$ EDX spectra for each sample in the glass layer. The following elements were found in the glass layer and were significantly above the detection limit of EDX: O, Si, Pb, Ag, Al, Zn and Ti.

The results reported here explicitly address the paste specifications differences both in the microstructure and chemical analysis of the glass layer. High-efficiency cells (#2 and #3) show significantly more nano-Ag colloids and precipitates in the glass layer as compared to cell #1. The density of such precipitates and nano-Ag colloids are paste dependent: (i) for high-efficiency cells #2 (p-type) and #3 (n-type) we observed a high density of precipitates and Ag colloids and a contact resistance of less than $5 \, \text{m}\Omega \, cm^2$ and cell efficiencies of 18% for p-type and 20% for n-type, respectively, (ii) for cell #1 a much smaller density of Ag colloids /precipitates in the glass was observed and, therefore correlated with a high contact resistance ($20 \, \text{m}\Omega \, cm^2$) and hence a low efficiency (16.9%). This indicates that the series and contact resistance of the screen printed front side contacts depend on the microstructural features of the glass layer.

Ionkin et al. reported the influence of nano-Zn grains and micro-Zn pastes on electrical properties such as efficiency, fill factor, and series resistance of the solar cell [115]. The authors concluded that micrometer-sized metallic Zn and ZnO grains are reducing the efficiency of the crystalline Si solar cells compared to cells contacted with the nano-Zn paste. This is in agreement with our experimental findings for cell #1 wherein we observed a relatively large Zn mole fraction and micrometer sized Zn rich phases in the glass layer. This results in a Zn_2SiO_4 rich oxide phases and an interrupted wetting of the glass layer. In case of high-efficiency cells #2 and #3, Zn and Al mole fractions in the range of $1-2$ at.% was detected in the glass layer and therefore yield a more pronounced wetting and a high density of Ag colloids in the glass layer.

These results suggest that the growth of nano-Ag colloids is mainly affected by Zn and Al mole fractions because all other elements were found in the similar range. Given the large number of precipitates found in the glass layers of high-efficiency p- and n-type cells in this study, we assume that current paths across the glass layer, e.g. due to percolation, exist and thus reduce the effective glass layer resistivity. behaves insulating. The glass layer is considered to be a dirty semiconductor containing highly conductive Ag colloids and precipitates on a smaller length scale.

5.4.2 Differences in chemical composition of the glass layer for cells processed with different pastes

The Si/metallization interface consists of a glass layer next to the Si emitter and Ag colloids and precipitates on a smaller length within the glass layer. Paste specific features can be identified by applying imaging and EDX spectroscopy of the glass layer in the TEM. Elemental mapping of such

complex interfaces is essential for understanding the paste specific differences and their effect on the electrical properties of the cell.

Zn, Al and Ti mole fractions in the glass layer vary for cells processed with different pastes. The average Pb mole fractions of cells reported here did not change significantly from cell to cell. For cell #1 Zn mole fractions up to 5 at.% were detected in the glass layer whereas only 1 at.% Zn mole fraction was detected for cells #2 and #3. Al mole fraction of 1 at.% was detected in the glass layer of cells #2 and #3, but not detected in the glass layer of cell #1. The paste composition usually is not known, but could be identified by measuring the chemical composition of the glass layer by TEM-EDX.
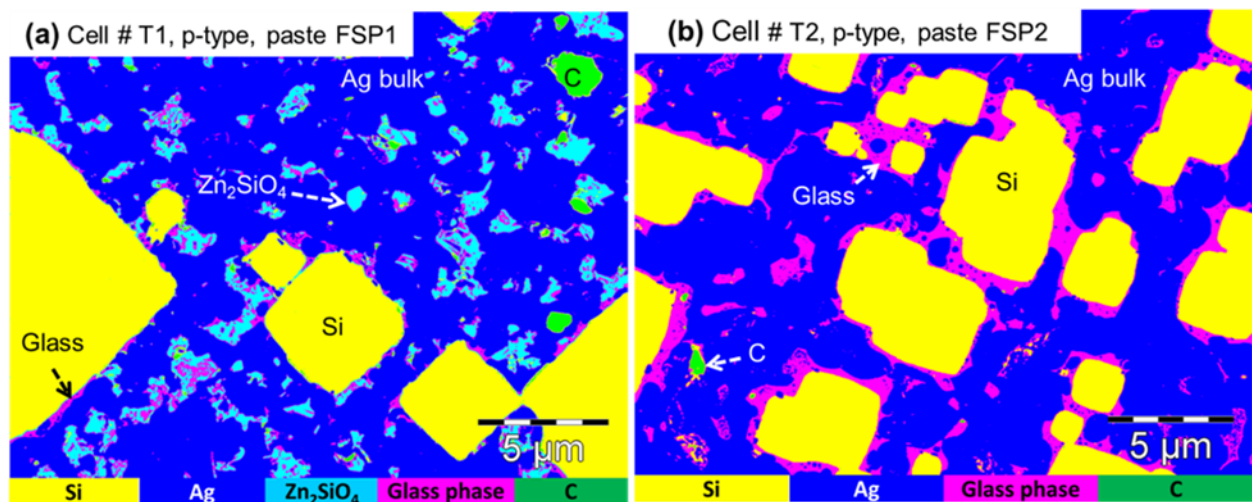
Figure 5.11: Plan-view false color backscattered electron (BSE) images are obtained at the Si/Ag interface of (a) a Zn rich paste FSP1, cell #T1 and (b) a Zn poor paste FSP2, cell #T2. It is evident that Zn rich paste yielded a discontinuous wetting of the glass phase and Zn rich oxide phases at the Si/metallization interface.

The effect of wetting the Si emitter surface by the front side metallization paste can be monitored by BSE images in the SEM. Pronounced wetting yields a continuous glass layer (magenta in Fig. 5.11) at the Si surface (paste FSP2, Fig. 5.11b), whereas restricted wetting yields a discontinuous glass layer (paste FSP1, Fig. 5.11a).

P and B could be detected in the glass layer if their concentration exceeded the detection limit of EDX in the TEM. P in the glass might come from the dissolved emitter or impurities added in the form of P_2O_5 [116] in the paste, whereas B could be detected if borosilicate glass used in the glass frit [85]. Since these elements were not observed in the glass layer of cell #3 and, therefore we consider that they do not play an important role in the reduction of the contact resistance.

5.4.3 Methodology: accuracies and minimum detectible mole fraction, elements in the glass layer

The chemical composition of the glass layer contains more than 10 elements i.e., Si, Ag, Pb, Al, Ti, Zn, O, P and B and determines the series and contact resistance of the front side metallization contacts. The lateral resolution in the SEM is not sufficient for many of the investigated structures (nano-Ag colloids, precipitates and glass layer etc.) and, therefore, a combination of SEM and TEM-EDX was the method of choice. Among the measurement techniques, TEM is highly relevant for analyzing the

microstructure and chemical composition of the glass layer down to sub-μm scale.

The quantitative chemical analysis of the glass layer, especially for the light elements requires improved lateral resolution. Lateral resolution of EDX in the SEM can be substantially improved, if a 5 keV primary energy was applied as shown in this work. Spectra acquired under such conditions can be quantitatively analysed and compared to spectra acquired in the TEM. The Cliff-Lorimer k factor method was used to quantitatively analyze spectra acquired in the TEM [36].

In our recent publication [117], by NanoSIMS (Secondary Ion Mass Spectroscopy) we have shown the effects of the firing conditions on the dopant distributions such as P and B (with a lateral resolution of 80 nm) across the Si/metallization interface and its relation to the series and contact resistance. The quantification as well as imaging of dopants cannot be observed by electron microscopy such as SEM and TEM and, therefore, further analysis of the glass layer by NanoSIMS would be of great interest for imaging precipitates and impurities atoms with a lateral resolution of 100 nm.

5.5 Conclusions

In this work, we report on the microstructure and quantitative chemical analyses of the glass layer of high-efficiency p- and n-type Si solar cells by SEM and TEM-EDX spectroscopy. High-efficiency cells (18.0% for p-type and 20% for n type cells) show similar features: microstructure and chemical composition of the glass layer (a more pronounced wetting and the higher density of nano-Ag colloids), contact resistance less than 5 mΩ cm^2 and the similar temperature dependence of the series resistance.

Given the large density of nano-Ag colloids and other precipitates observed in the glass layer of high-efficiency cells #2 and #3, a percolative charge transport across the Si/meta-llization interface has been proposed.

The chemical composition of the glass layer serves as a chemical bar code of the applied paste used for the screen printing process and affects the contact resistance of the metallization. These findings are of relevance for the paste optimization and charge transport across the Si /metallization interface.

The chemical composition of the glass layer is of importance for understanding its microstructural features and its correlation with the electrical properties. The chemical composition of the glass layer was found to be (SiO_X) Pb, elements like Zn, Ti, Al and Ag were detected in the glass layer as impurities. The mole fractions of these elements were above the detection limit of EDX spectroscopy and, therefore, the glass layer is considered as a dirty semiconductor rather than an insulator.

Al and Zn mole fractions (in the range of $1-2$ at.%) were detected in the glass layer of high-efficiency p- and n-type cells. This implies that the role of additives in the glass layer is essential for the reduction of the contact resistance.

Chapter 6

Direct imaging of dopant distributions across the Si-metallization interfaces in solar cells: Correlative nano-analytics by electron microscopy and NanoSIMS [117]

6.1 Background

Secondary Ion Mass Spectrometry (SIMS) depth profiling has played an essential role for semiconducting devices particularly for Si solar cells technology [118], and thin film solar cells (e.g., CIGS thin film solar cells) [119, 120, 121]. New instrumentation lead to NanoSIMS, i.e. SIMS with a high lateral resolution and high sensitivity [122, 123]. This new possibilities due to instrumentation yielded significant results for contamination of metals and their structural properties. Among the many results obtained by NanoSIMS only few deal with semiconductor technology. Since Nano-SIMS is primarily used in technology calibration and failure analysis which represents confidential information.

Static random-access memory (SRAM) devices based on complementary metal-oxide semiconductor (CMOS) technology were analysed for failure analysis purposes and structures grown in a 130 nm technology could be resolved by NanoSIMS. B, As and P doped active areas on the 130 nm scale could clearly be identified. This shows the great potential of NanoSIMS for providing the local dopant concentration at the 100 nm scale [124]. It should be added that the lateral resolution and sensitivity both affect the minimum detection limit and that resolution and minimum detectable mass fraction have to be proven experimentally for individual cases. This is one of the purposes of this paper. The relatively large dopant concentrations in emitters of Si solar cells make NanoSIMS ideal for studying the dopant distribution in such devices.

The influence of firing conditions on the microstructure and its effect on the contact resistance was reported in the literature [76, 77, 78, 79, 80] , however, no systematic analysis has been carried out, particularly with respect to dopant distribution at the Si/metallization interface. Due to the high temperature firing process, atoms from the metallization are assumed to diffuse as impurities into the emitter as well as space charge region of the solar cell [82]. This in turn increases the recombination current of the emitter and space charge region of the cell, and degrades the cell efficiency.

An important factor that limits the solar cell efficiency is the electrical resistance across the Si metallization interface. The spatial distributions of dopants across this interface play a key role in determining the overall efficiency. Until now, direct imaging of dopant (P, B) distributions across the Si metallization interface has not been reported mainly because the concentrations of dopants are far below the detection limit of conventional analytical tools such as EDX. In the present study, we harness the high-resolution high-sensitivity chemical imaging with NanoSIMS and correlate with microstructural and electrical properties thereby giving us unprecedented insights into the factors

limiting the overall cell efficiencies.

P-type textured cells were processed identically upto the front side metallization, the only difference is the firing temperature. The metallization was realized by a screen printing technology, and front side paste (FSP1) was used to contact the P doped emitters. Cell #T1 was processed under optimal firing condition to a set temperature of ($T_{FF0} = 900°C$), whereas cell #T2 was processed at a too high set temperature (overfired, $T_{FF0} = 960°C$). The overfired cell #T2 yielded a significantly higher series resistance (3.91 Ω cm^2) and a low efficiency (13.1 %) as compared to the cell #T1. Due to overfiring cell #T2 showed a high specific contact resistance (131 mΩ cm^2), whereas cell #T1 had a small contact resistance of (21 mΩ cm^2) and higher efficiency ($\sim$17 %).

6.1.1 Secondary Ion Mass Spectrometry with a high lateral resolution (NanoSIMS)

SIMS is particularly well-suited for the study of dopants in silicon such as B and P thanks to its possibility to detect elements in very low concentrations in depth profile mode [122]. In this study a Cameca NanoSIMS 50 equipped with a double focussing magnetic sector spectrometer was used in imaging mode [125]. The essential features of this recently available instrument are its outstanding lateral resolution together with excellent detection limits enabling the analysis of the dopants in Si. It could be shown that a lateral resolution down to 50 nm can be reached in the negative secondary ion mode under Cs^+ primary ion irradiation, for details see [125]. The instrument was operated with a primary Cs^+ source and a probe current of 1 pA with an impact ion energy of 16 keV. The secondary ion maps were acquired as 256 x 256 pixel images with a dwell time of 5 to 10 ms per pixel on fields of view of 15x15 μ m^2. The instrument was tuned to resolve the mass interference between $^{31}P^-$ and $^{30}Si\,^1H^-$ with a mass resolution M/ΔM above (4000) [122].

The NanoSIMS can be run at high mass resolution without significant loss of the transmission of the instrument [125]. As the coaxial optics of the NanoSIMS requires opposite polarities between the primary and secondary ions, and as a Cs^+ primary ion beam was used, all elements were detected as negative secondary ions. Boron was detected as a cluster with Si ($^{28}Si\,^{11}B^-$), as this cluster has a higher negative ionisation probability than B-.

6.2 Results and Discussion

The microstructure of the Si/Ag metallization contact interface was investigated by SEM both in cross-sectional and plan view as shown in Figure 6.1a−d. The microstructural features of cells #T1 and #T2 are apparently very similar, however, due to overfiring, a slight increased of the Ag nanocrystals size and thickness of the glass layer was found at the contact interface [117]. Therefore, a detailed investigation by NanoSIMS is essential to explicitly address the differences between the cells #T1 and #T2.

6.2.1 Chemical mapping by NanoSIMS on the doping level

In Figure 6.2 both secondary electron (SE) images as well as ion maps are shown, both acquired with a primary ion beam scanning the surface of the sample. The ion maps (in Figure 6.2d−f and j−k)

are presented as RGB overlays by assigning different colors: red for Si, green for P and blue for B (detected as SiB- secondary ions). Ion maps of cell #T1 and cell #T2 are shown in Figure 6.2−6, both linear and log images are displayed.
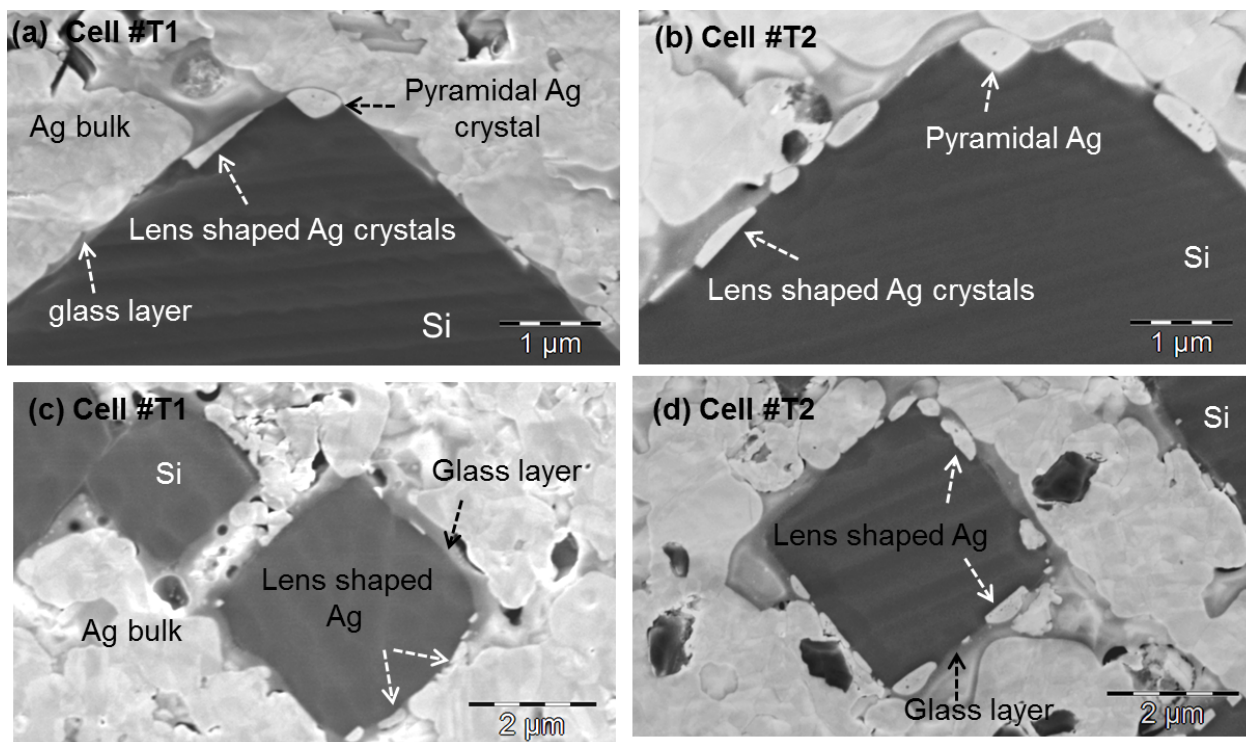
Figure 6.1: Cross-section SEM images of cell #T1 (a) and the overfired cell #T2. (b) Pyramidal and lens shaped Ag nanocrystals are embedded at the Si emitter, (c) and (d) are the plan-view images cell #T1 and cell #T2, respectively obtained at the Si/metallization region.

In appendix B, a guide line is given for reading the maps and assigning the different device relevant areas of the cell. The lateral resolution of the acquired NanoSIMS maps is larger than 80 nm. For optimally fired cell # T1, P rich lines are imaged as green lines in RGB ion maps (Figure 6.2d−f), about 200 nm wide enclosing islands of metallization and are imaged very reproducibly. Such lines correspond to the highly doped fraction of the emitter on top of the emitter structure. It is a key result of this work that these regions can be imaged at all in NanoSIMS ion maps, they also prove that the emitter structure is preserved for cell #T1, but not for cell #T2 (see Figure 6.2j−l).

The emitter structure in cell #T1 displays a high intensity of P signal along the interface with the glass phase, seen here as a bright green line (Figure 6.2d−f). As expected, the P signal strongly decreases towards the Si substrate but lies beyond the detection limit of NanoSIMS in the substrate.

When observing the overfired cell #T2 (Figure 6.2g−h, and j−k), the structure is very different to that of cell #T1, since the high-concentration line (green line) of P at the interface with the glass has disappeared. Instead, P appears as small P rich domains in the metallization area and nowhere in the substrate, meaning that the original emitter structure has not been preserved. A schematic sketch of the Si emitter, metallization and bulk Si for cell #T1 and the overfired cell #T2 is shown in Figure 6.2i and 6.2l, respectively.

Figure 6.3a shows the RGB overlay of cell #T1. In the image arrows indicate lines along which line scans (Figure 6.3c and d) were acquired.
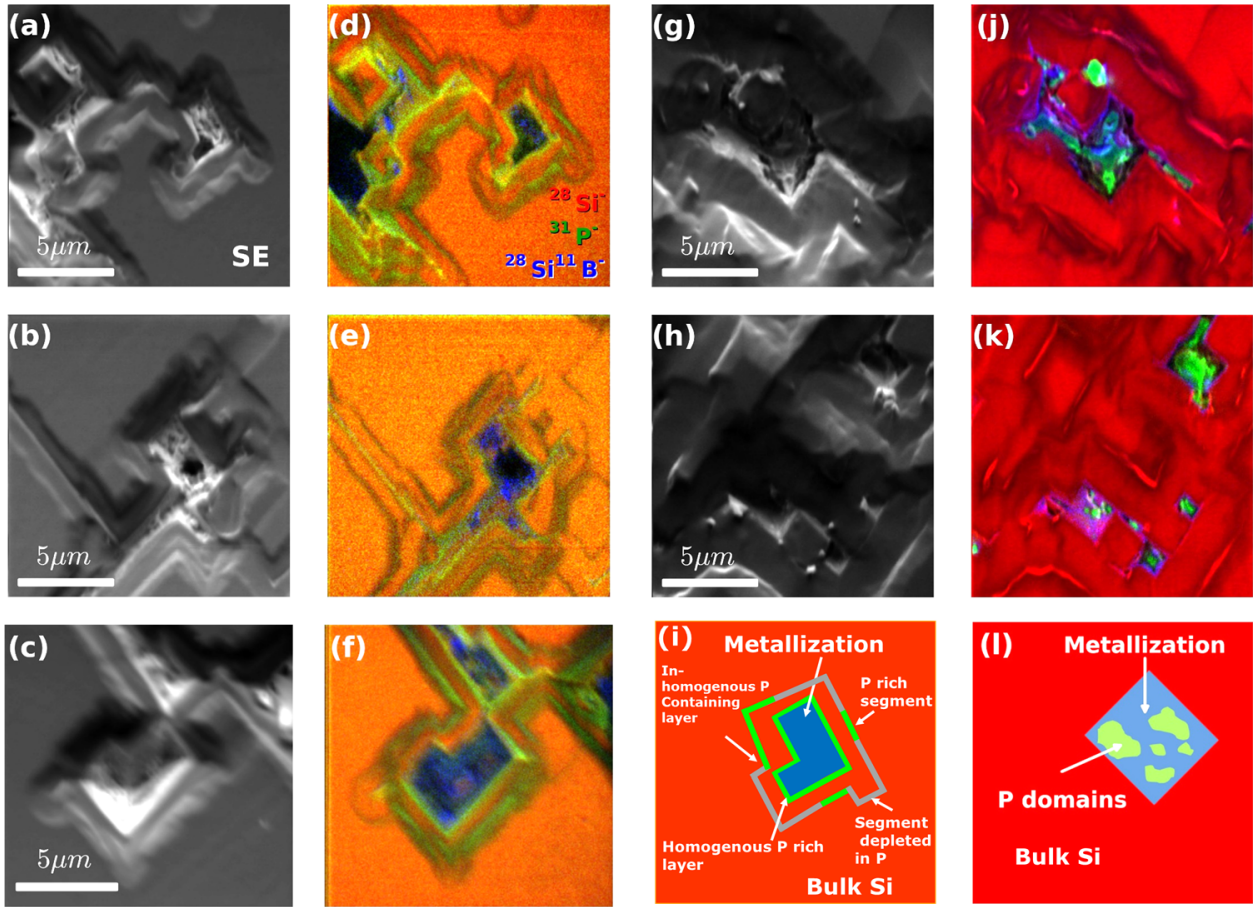
Figure 6.2: (a−c) Secondary electron images obtained on the cell #T1 at three different areas: (a) area 1, (b) area 2, and (c) area 3. (d−f) NanoSIMS RGB elemental overlays of the same areas obtained in the plan-view of cell #T1. Similarly, (g, h) secondary electron images of two different areas (area 1 and 2) and (j− k) NanoSIMS RGB overlays in the plan-view of the overfired cell # T2. RGB overlays are composed of Si (red), P (green) and SiB (blue) signals. Schematic sketch of cell #T1 (see Fig. 6.2i) and the overfired cell #T2 (see Fig. 6.2l) with marked areas has been introduced.

The line scans extend from the metallization into the Si substrate. With the line scans the device relevant areas can be assigned which is done in Figure 6.3b. Metallization (1), P-rich emitter region (2), and emitter region (3) are indicated. Furthermore, an inhomogeneous layer labeled as (4) contains both P-rich segments but also segments depleted in P.

6.2.1.1   Detailed analysis of the cell #T1

Treating the B and P distributions in more detail, two kinds of images have been generated, using linear and logarithmic color scales. While the linear images (for details see Figure 6.4a−b and Figure 6.5a−b) display the areas with higher mole fraction of ions prominently, the regions with lower counts are best displayed in log images. When using a logarithmic scale (see Figure 6.4c−d and Figure 6.5c−d), the areas with lower number of counts are also seen prominently and even small differences in doping can be easily observed.
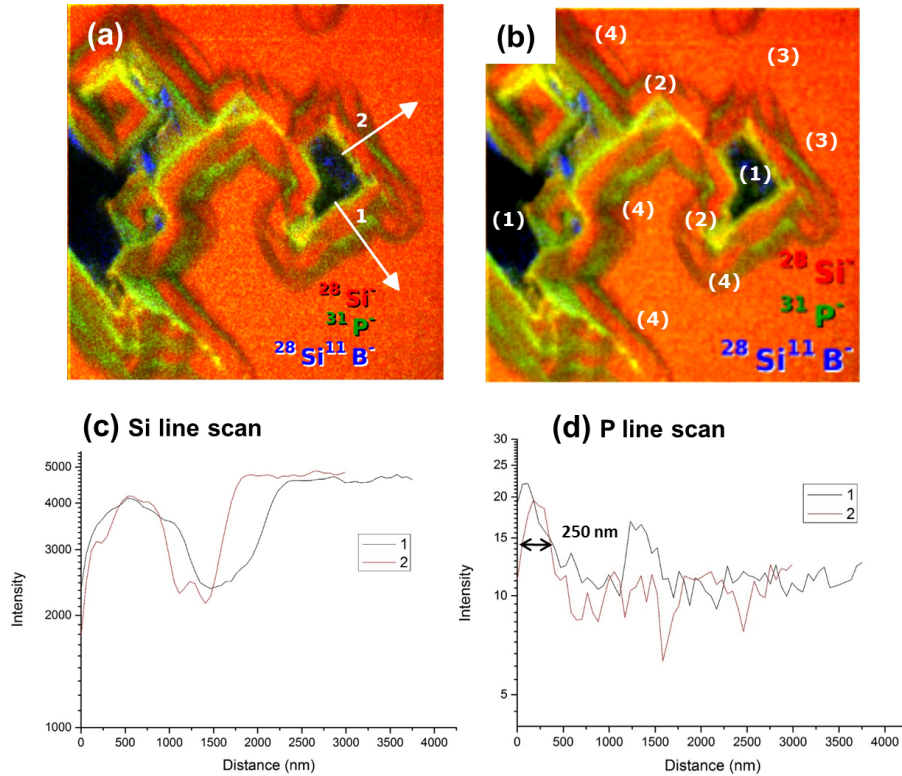
Figure 6.3: Represent the RGB overlay image of cell #T1 (Figure 6.3a-b). Arrows indicate lines along which line scans (as shown in Figure 6.3c and d) were acquired. The line scans extend from the metallization into the Si substrate.
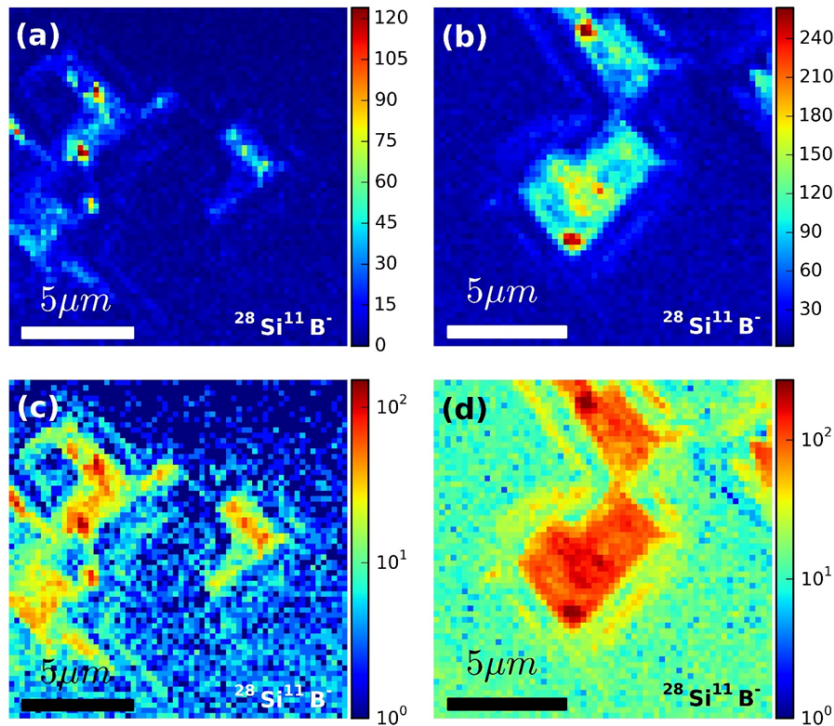
Figure 6.4: NanoSIMS images of the B distribution (detected as SiB^- secondary ions) after 4×4 binning in linear (a, b) and logarithmic (c, d) color scales for two areas (area 1(Figure 6.4a) and area 3 (Figure 6.4b)) of cell #T1. Despite the binning, the structures with lower signal intensity are still not very prominent in the linear scale shown in (a) and (b). However, by displaying the images in the log scale as in (c) and (d), even the structures with relatively lower intensity emerge prominently.

Furthermore, binning has been introduced for the SiB images to increase the counting statistics and to decrease the noise. This yields a loss in lateral resolution but also an improvement with respect to the signal-to-noise ratio.

We can observe that the maximum B mole fraction is found in some areas of the metallization (see Figure 6.4a−b). Observing the same images in logarithmic scale (see Figure 6.4c−d), we can still see that the maximum B mole fraction is found in the metallization, but also that B extends into the Si and having a maximum distribution in a 1-2 μm cloud surrounding the metallization. Similarly, in the P distribution as shown in (see Figure 6.5a−b) the linear images show that the higher mole fraction was found at the Si/metallization interface. The logarithmic version of the images (see Figure 6.5c-d) shows also that the dopant distribution is homogeneous in the substrate. Overall, in the cell #T1, the emitter region appears fairly homogeneous, where P increases close to the Si/metallization interface and B is mainly found in the metallization.
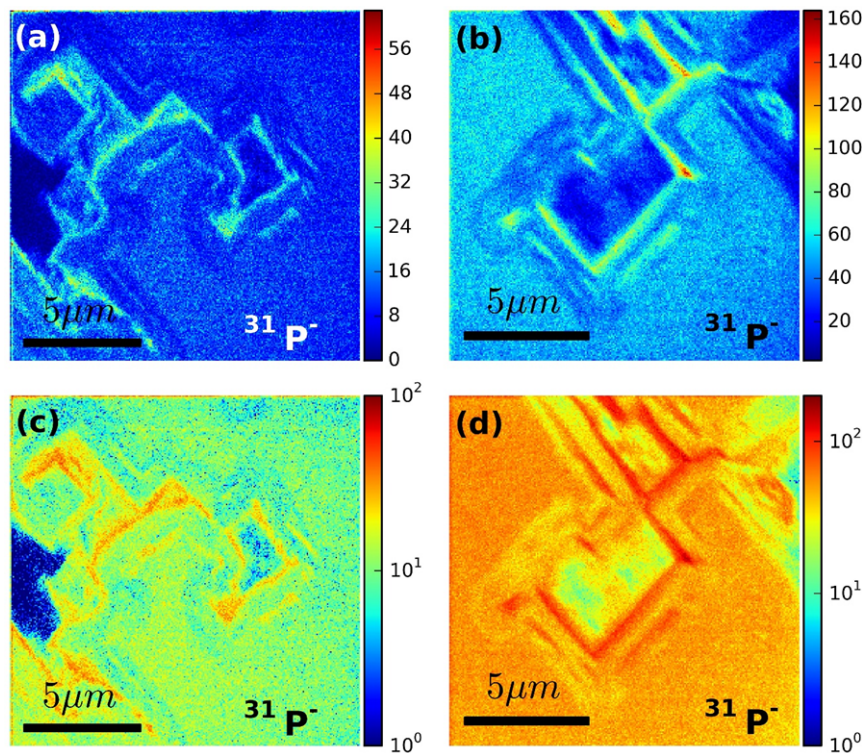
Figure 6.5: NanoSIMS images of P distribution as-acquired (no binning) in linear (a, b) and logarithmic (c, d) color scales for two areas (area 1(Figure 6.5a) and area 3 (Figure 6.5b)) of cell #T1. In the bottom row note the red areas of high intensity and the inhomogeneity in the P distribution.

6.2.1.2 Detailed analysis of the overfired cell #T2

The overfired cell #T2 was investigated both in cross-section (Figure 6.6a−c) and plan-view (Figure 6.6d−f). Looking at the plan-view, B remains mostly in the metallization, with lower mole fraction in the Si substrate (Figure 6.6d−e). The most noticeable change is the disappearance of the higher intensity P lines (1−2 μm) that were observed only for cell #T1 (see Figure 6.2, green line).

In the cross section, we can find an area of high B below the metallization (red areas in Figure 6.6b). In the P map the high intensity lines found at the interface of the metallization for cell #T1 (Figure 6.2) disappeared for cell #T2 (see Figure 6.6). Furthermore, in contrast to cell #T1, P signals in the bulk

are now lower than in the metallization. The enrichment of P in the metallization can be explained by the diffusion of P from the substrate. In the cross section image as shown in Figure 6.6c, P rich metallization is surrounded by some P rich Si matrix, which disappears a few microns below the emitter surface.

In accordance with the SEM results as described in [117], due to the disintegration of the SiN_X layer in the overfired cell #T2, a diffusion cloud developed that extends over several microns below the metallization at an area that has been assigned to the emitter. It develops B rich regions and P rich regions (see Figure 6.6), which give rise to the enhanced series and contact resistance and areas of B-O defect complexes. The orange region in the Si map correlates to this diffusion cloud which results from a 3-dimensional diffusion process. In this diffusion cloud a relatively homogenous level of P doping is seen.
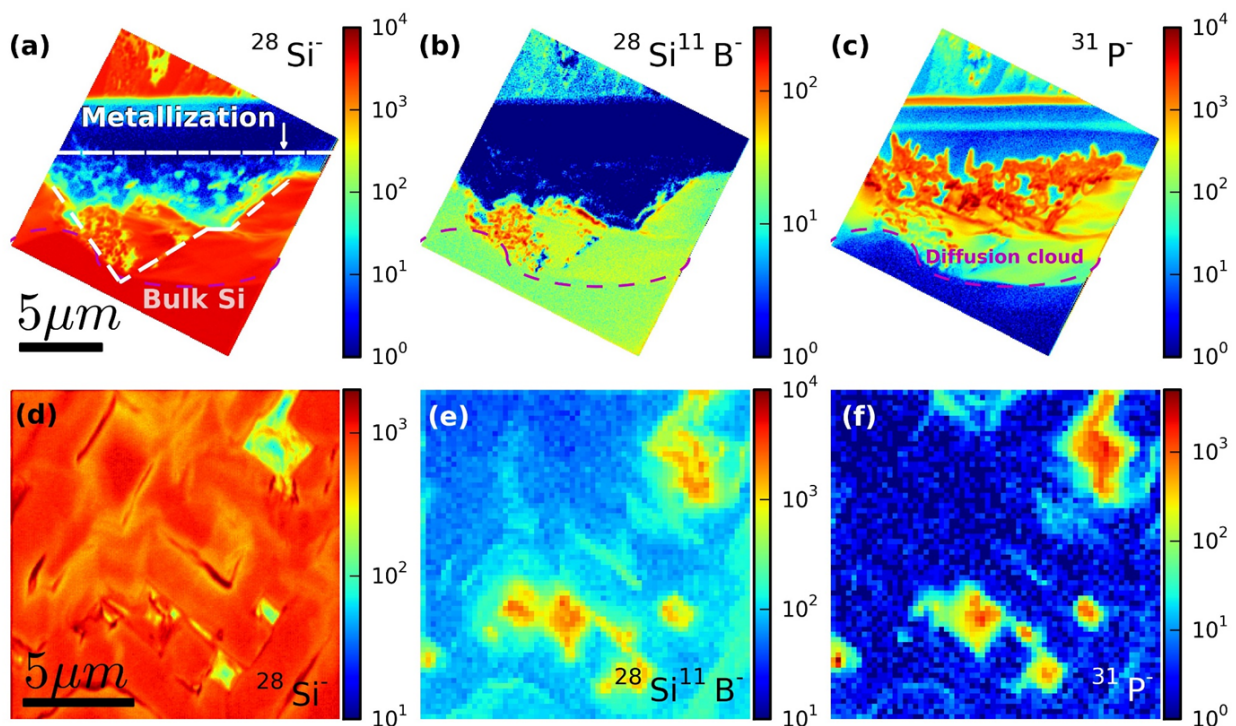
Figure 6.6: Si, B (detected as SiB^- secondary ions) and P maps of the overfired cell #T2 in cross-section (a−c) and in plan-view (area 2) (d−f): In comparison to cell #T1 images in (see Figure 6.6c,d), the emitter structures of the overfired cells are completely lost as seen here in the P maps. Note, (e−f) maps have been binned 4x4. All images are in log color scale.

The fall off of the P doping and with it the emitter structure appears in the P map (Figure 6.7b). In the Si map the same interface (Figure 6.7a) is found between the orange region and the red region. This is seen in the line scan of Figure 6.7d. Line profiles for the three species were obtained along the arrow indicated in the SE image (see Figure 6.7c–d). The P counts (100 counts, Figure 6.7d) below the metallization is constant for around 2 μm from the emitter surface, and it falls to a few counts (1–2 counts) below that, while B counts remain constant throughout the substrate. In the overfired cell the disintegration of the SiN_X layer identified in the SEM [117] correlated with the disintegrated emitter structure (P) analysed by NanoSIMS.

6.3 Conclusions

In summary, we have demonstrated the power of the correlative approach combining electron microscopy and NanoSIMS for high-resolution and high-sensitivity characterization and to understand the observed electrical properties in optimally fired and overfired monocrystalline Si solar cells. In comparison to conventional analytical tools such as EDX, the high sensitivity of NanoSIMS, even in the imaging mode, enables direct imaging of dopant distributions across the metallization interface. With this unique capability, we have shown that the local opening of the diffusion barrier (SiN_X) layer was observed only in cell #T1 thereby spatially confining B and preserved the P doped emitter structure.

However, in the overfired cell the diffusion barrier (SiN_X) layer was completely disintegrated leading to barrier-free diffusion of B rich pockets (extending over several μm) into the substrate. Due to the complete disintegration of the emitter structure below the metallization, a diffusion cloud is found yielding a diffuse interface. With such structures an increased contact resistance could be correlated.
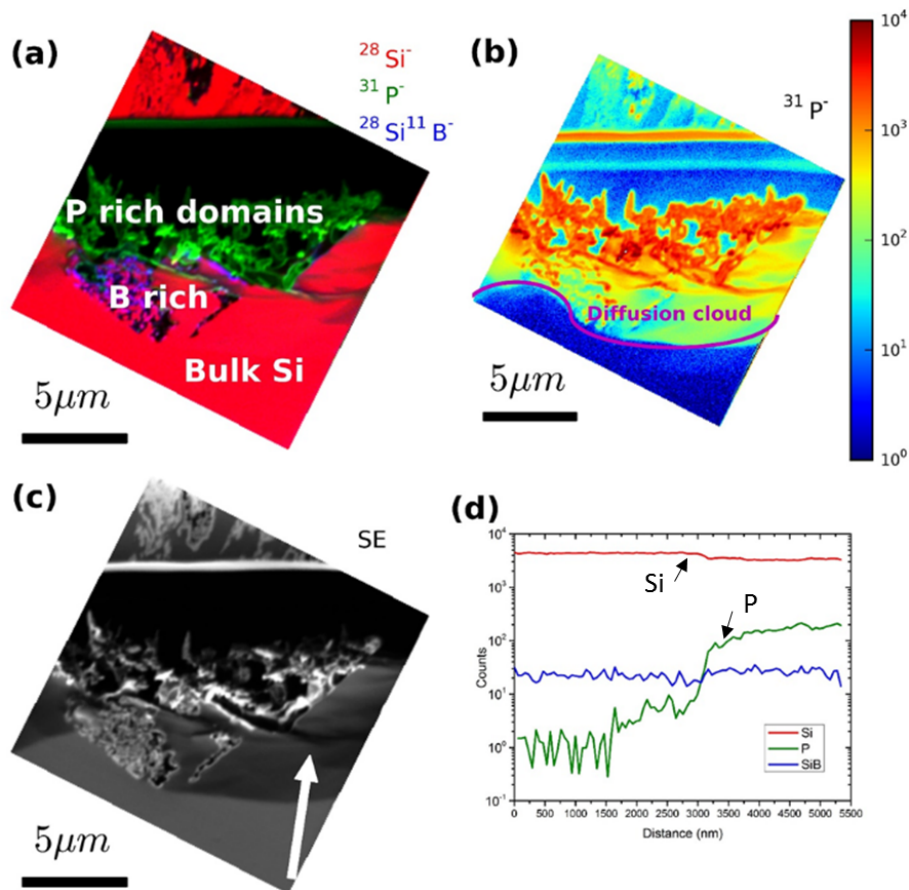
Figure 6.7: Details of the overfired cell #T2 in cross-section (a) RGB overlay of Si, P and B (detected as SiB⁻ secondary ions) maps in red, green and blue respectively in linear scale (b) as-acquired (no binning) P map in the log color scale, (c) secondary electron image of the cross section and (d) line profiles along the arrow indicated in the secondary electron image. Note, the P concentration profile fall off at the edge of the green to blue transition seen in (b) over two orders of magnitude. This transition is also seen in the Si line scan, while B intensity remains constant.

Appendix A

Microstructure analysis of cell #1 by TEM

The microstructure features of the Si/metallization interface of cell #1 contacted with paste FSP1 are shown in Figure A1 a−b. The Si texture (pyramidal shape) can be clearly identified in the image. The microstructure features showed a glass layer typically 200 nm thick and including nano-Ag colloids. The nano-Ag colloid size was measured between 5 nm and 220 nm. Additionally, some Zn_2SiO_4 rich phases were observed in the glass layer with sizes between 300−500 (Figure A1). The corresponding dark-field image of the glass layer revealed small density of nano-Ag colloids. The bigger Ag colloid are crystalline in nature, while the nature of smaller Ag colloids is not clear.
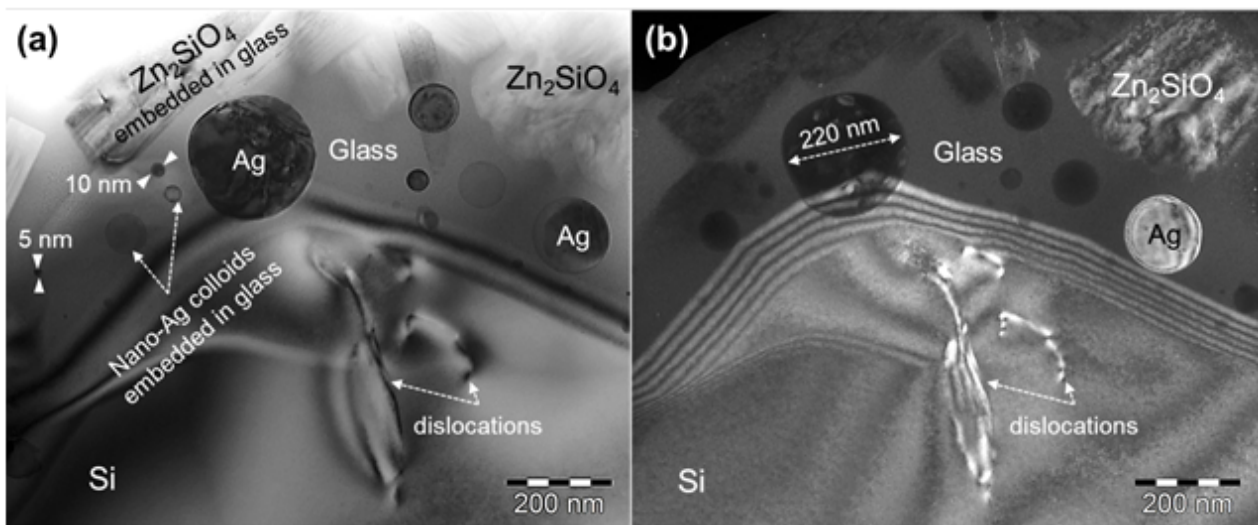
Figure A1: High-magnification (a) bright-field and (b) dark-field images of the Si/metallization interface. Direct (Si-Ag) and indirect (Si-glass-Ag) contacts can be seen along with the nano-Ag colloids of sizes 5−220 nm and Zn rich phase of sizes 300−500 nm embedded in the glass layer.

Phase identification of cell #1, #2, #3 by TEM-EDX spectroscopy

Depending on the paste composition, Si/metallization interface yielded different phases that were documented by EDX spectroscopy in the TEM. For cell #1 a number of phases were identified at the Si/metallization interface and are shown in Figure A2. These phase are: (i) Si emitter, (ii) the glass layer, (iii) presence of the SiN_X layer and finally (iv) Zn rich phases. These observed phases were first mapped by EF-TEM imaging and then quantitatively analysed by TEM-EDX spectroscopy. A nitrogen (N) peak could be detected at the Si/glass interface and can be seen in the Figure A2a. The presence of passivation layer (SiN_X), Si emitter, Ag colloids and Zn rich oxide phases can be seen in the spectra. For Zn rich phases (see Figure A2c), a fairly large Zn peak was detected in the glass layer of cell #1. In Figure A3 and A4 similar investigations of cell #2 and #3 are shown.

In agreement with the cell #1 results, cells #2 and #3 also showed the Si emitter, SiNX layer, Ag colloids and the glass layer. The major differences between the cell #1 and cells #2 and #3 are: the chemical composition of the glass layer is significantly different especially for the mole fractions of Al and Zn. For cell #1, a large Zn mole fractions and almost no Al was detected in the glass layer whereas such elements were present (1-2 at.%) in the glass layer of cells #2 and #3.
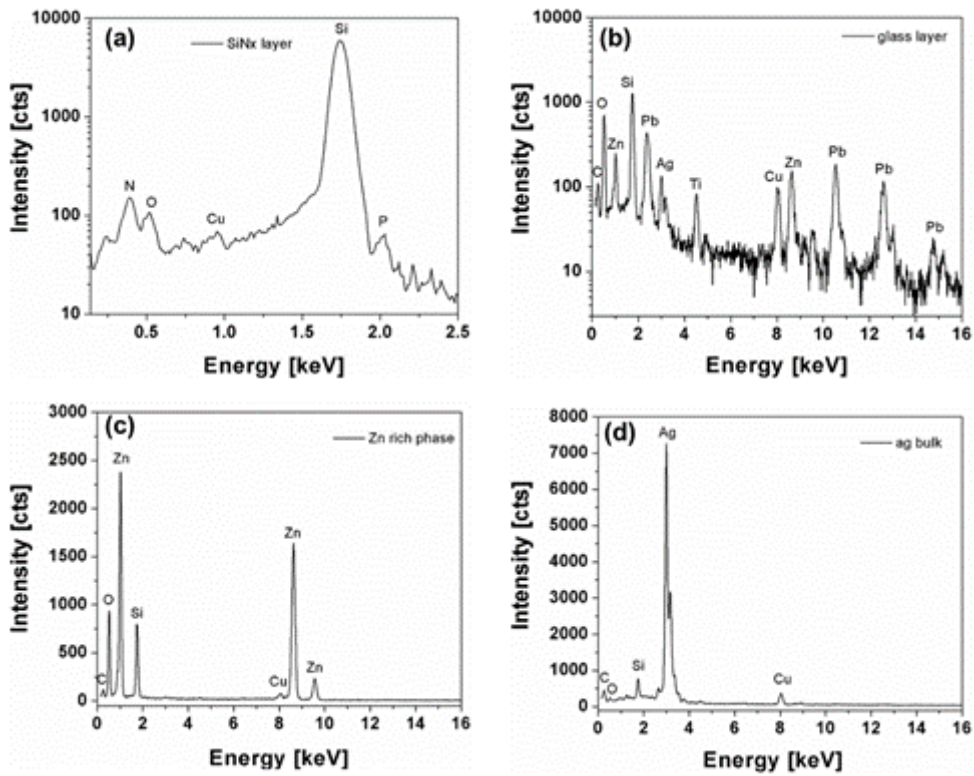
Figure A2: Point TEM-EDX spectra of the different phases obtained at the Si/metallization interface of cell #1 contacted with paste FSP1: (a) SiN_X phase plotted in a logarithmic scale, (b) glass phase, (c) Zn rich oxide phase and (d) Ag bulk of the metallization.
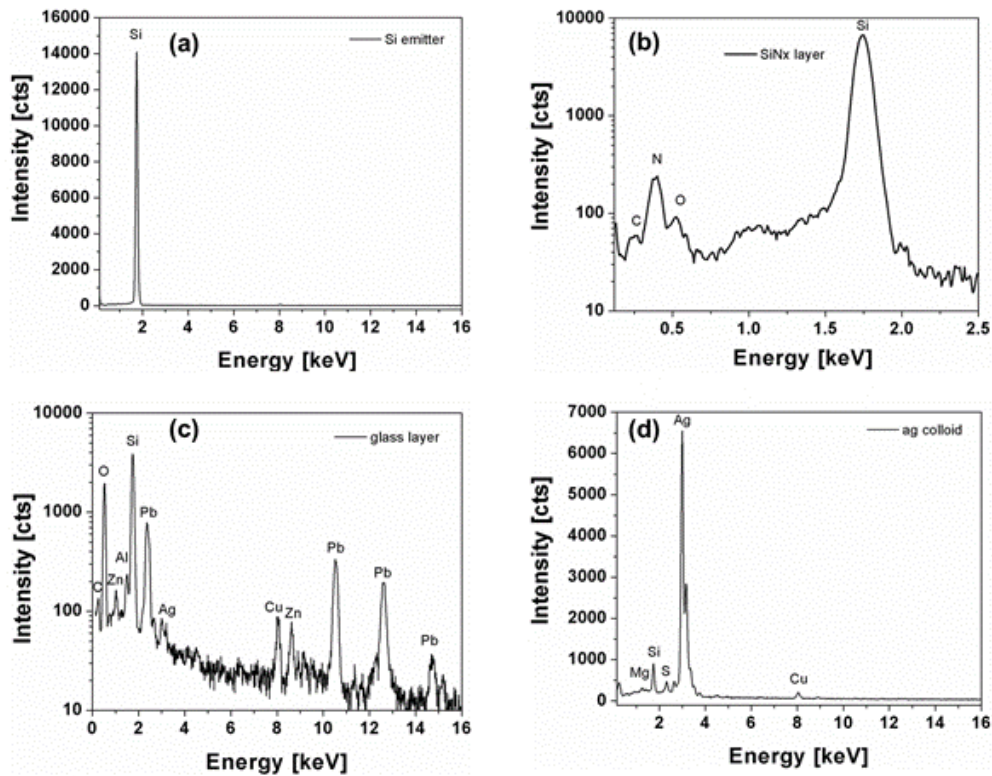
Figure A3: Point EDX spectra of different phases obtained on cell #2 contacted with paste FSP2: (a) Si emitter, (b) SiN_X layer as shown in logarithmic scale, (c) the glass phase and (d) nano-Ag colloid.
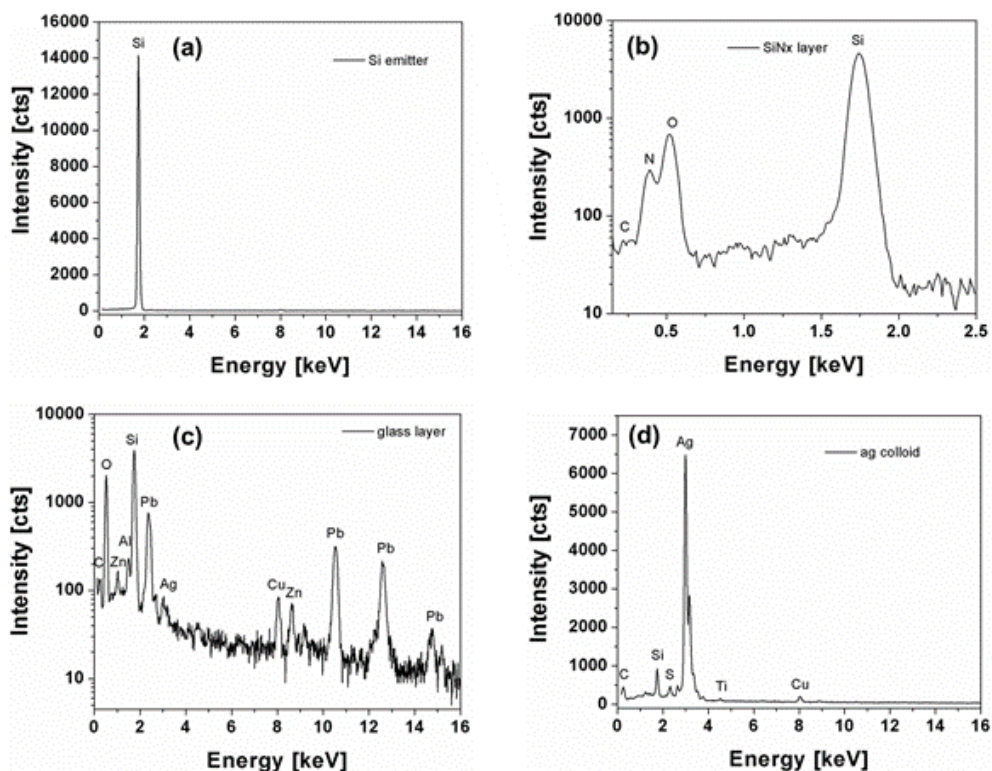
Figure A4: Point EDX spectra of different phases obtained on cell #3 contacted with paste AgAl: (a) Si emitter, (b) SiN_X layer as shown in logarithmic scale, (c) the glass layer and (d) nano-Ag colloid.

B and P peak analysis by SEM and TEM-EDX spectroscopy

Detailed investigation of the dopants/additives such as P, B in the glass layer by SEM and TEM-EDX was carried out and is shown in Figure A5. Depending on the paste composition, B and P could be measured in the glass layer. For cell #1, B as a lighter element can be detected and measured quantitatively by EDX but not quantified. The comparison of B-K peak of cell #1 by (a) SEM-EDX and (b) TEM-EDX spectroscopy is shown. Note that a small shoulder at 0.183 keV could be identified as a B-K peak and can be seen more clearly in the TEM-EDX spectra (see Figure A5b). B mole fractions were below the detection limit of EDX for cells #2 and #3. P mole fractions could be detected in the glass layer of cell #2, not in the glass layer of cell #1, and #3. For cell #2 a small P peak (see Figure A5 c−d) was observed in the spectra and yielded P mole fractions of 0.81 at.% in the glass layer. For cells #1 and #3, P peak was below the detection limit of EDX. In agreement with the SEM results both P and B could not be detected in the glass layer of cell #3. Note that Ti mole fraction was not detected in the glass layer by SEM-EDX analysis. With TEM-EDX we succeeded with the quantification of the Ti mole fractions in the glass layer. For cell #1, Ti mole fraction of 2.8 at.% was detected whereas for cells #2 and #3 Ti mole fractions were fairly small <0.5 at.%.

A quantitative correlation diagram between Pb mole fractions and Si is plotted in Figure A6. These measurements were carried out bb EDX in the TEM. From the graphs (Figure A6 a−c) a negative correlation was observed for all cells #1, #2 and #3, respectively. This shows that Pb and Si are negatively correlated: higher Pb mole fractions result in a smaller Si mole fractions and therefore, Pb substitute Si and vice versa. Similar correlation was found for Zn and Si and more important for the

combination of Zn+Pb versus Si (see Figure A6 d−f). These measurements also indicate that higher mole fractions of Pb and Zn replace Si and vice versa.
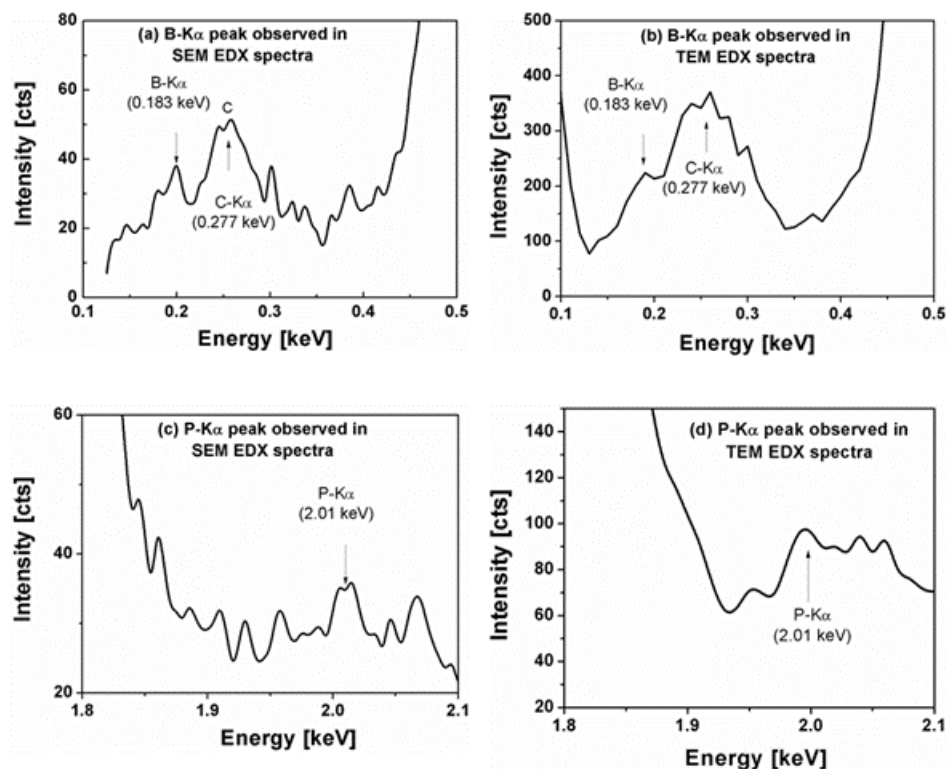
Figure A5: Point EDX spectra of the glass layer of cell #1 acquired in (a) SEM and (b) TEM. Both spectra show a small shoulder on the left side of the $C − K_\alpha$ peak was observed and assigned to a $B − K_\alpha$ peak, (c-d) show the P peak observed in the glass layer of cell #2.
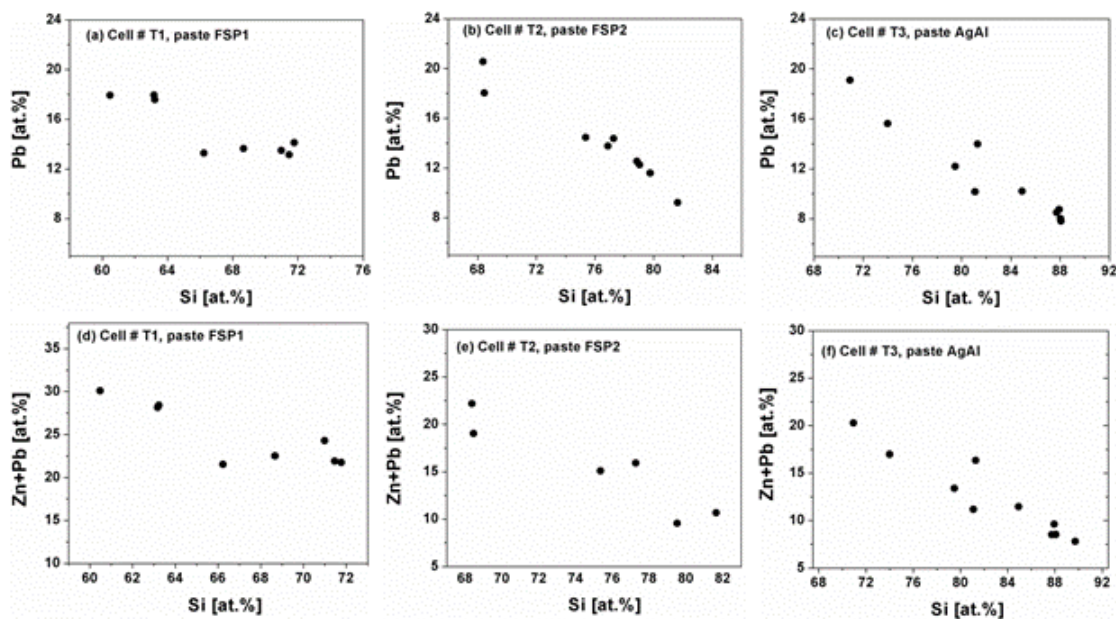
Figure A6: Pb versus Si correlation diagrams obtained on (a) cell #1, (b) cell #2 and, (c) cell #3, respectively. For cell #2 and #3 clearly a negative correlation is observed, however, for cell #1 data points are scattered but negatively correlated. (d-f) show the Zn+Pb versus Si correlation diagrams of all cells.

Appendix B

NanoSIMS ion maps for solar cells

While secondary electron images are standard experimental results in the investigation of solar cells ion maps are not and they are difficult to read and understand. First we would like to give an explanation how to read such maps which yield maps of ions containing dopant elements like the P and B. Secondary electron images can be acquired both in the SEM and NanoSIMS. NanoSIMS yields ion maps that directly represents the chemical information relevant for devices.

How to read ion maps of solar cell devices acquired by NanoSIMS

The Si ion map (Figure B1a) should be looked at first, followed by the P map (Figure B1b) that contains the dopant information, followed by superimposed RGB images for which the Si, P and SiB ion maps are used (see Figure B1c). To relate the NanoSIMS maps to device relevant regions the following assignment should be considered (see Figure B1b): (i) the metallization labeled as (1) in the P ion map image, (ii) a bright yellow line (homogenous layer) which contains the heavily doped P layer of the emitter region is labeled as (2) in the image. Apart from that line (2) a second line is seen which is partly yellow in the P map (inhomogenous layer) and is labeled as (4) in Figure B1c. It contains segments of high (green in Figure B1c) and low mole fractions (grey in Figure B1c) of P in the emitter. (iii) the remaining emitter region (with less mole fraction in P) is indicated as (3)
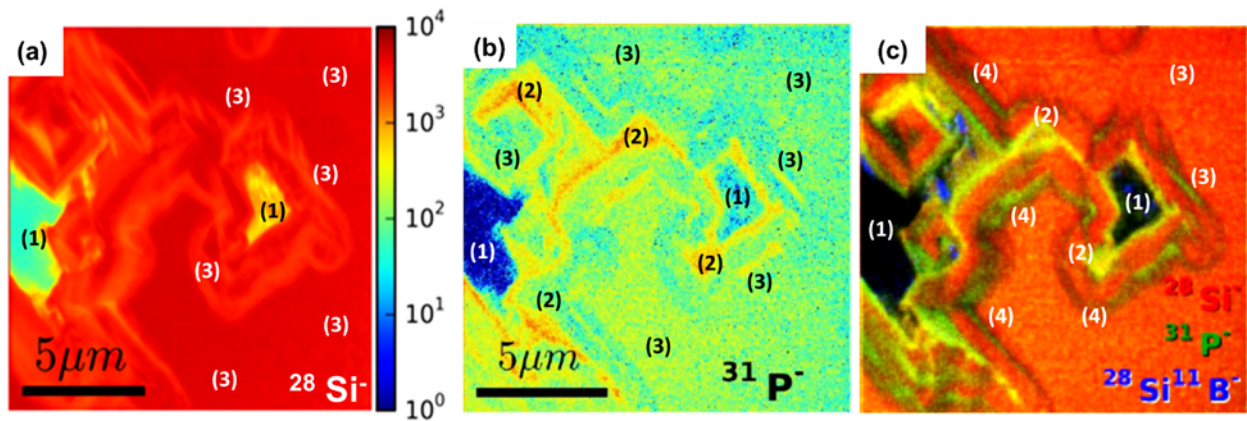
Figure B1: Cell #T1, NanoSIMS results (a) Si map, (b) P map and (c) RGB overlay ion map image of Si, P, and SiB. For interpretation of the NanoSIMS results we start with P map image (see Figure B1b) (1) Metallization (2) highly doped emitter (homogenous layer) only seen in P map not in Si map, (3) the emitter region, and (4) similar to (2), however, an inhomogenous layer (Figure B1c) with varying P concentration, varies from green (high P), to grey (low P). Note: (2) is easily visible in P map, (4) is imaged (Figure B1c) in the superimposed map (Si, P, SiB)

Bibliography

[1] The national aeronautics and space administration (nasa), vital signs of the planet: carbon dioxide, . URL `https://climate.nasa.gov/vital-signs/carbon-dioxide/`.

[2] The national aeronautics and space administration (nasa), vital signs of the planet: global temperature, . URL `https://climate.nasa.gov/vital-signs/global-temperature/`.

[3] The national aeronautics and space administration (nasa), vital signs of the planet: sea level, . URL `https://climate.nasa.gov/vital-signs/sea-level/`.

[4] A Jäger-Waldau. Pv status report 2012,, 2017. URL `doi:10.2790/682995`.

[5] International technology roadmap for photovoltaic results 2016, itrpv eight edition, 2017. URL `http://www.itrpv.net/Reports/Downloads/`.

[6] Enrique Cabrera Campos. *Screen Printed Silver Contacting Interface in Industrial Crystalline Silicon Solar Cells*. PhD thesis, 2013.

[7] Adolf Goetzberger, Joachim Knobloch, and Bernhard Voss. *Crystalline silicon solar cells*. Wiley Online Library, 1998.

[8] Ankit Khanna. *Advanced metallisation methods for monocrystalline silicon wafer solar cells*. PhD thesis, National University of Singapore, 2015.

[9] Matthias Hörteis. *Fine-line printed contacts on crystalline silicon solar cells*. PhD thesis, Fraunhofer Institut für Solare Energiesysteme Freiburg, 2009.

[10] Damian Pysch, Ansgar Mette, and Stefan W Glunz. A review and comparison of different methods to determine the series resistance of solar cells. *Solar Energy Materials and Solar Cells*, 91(18):1698–1706, 2007.

[11] Antonio Luque and Steven Hegedus. *Handbook of photovoltaic science and engineering*. John Wiley & Sons, 2011.

[12] Simon M Sze and Kwok K Ng. *Physics of semiconductor devices*. John wiley & sons, 2006.

[13] Donald Neamen. *Semiconductor physics and devices*. McGraw-Hill, Inc., 2002.

[14] John Bardeen. Surface states and rectification at a metal semi-conductor contact. *Physical Review*, 71(10): 717, 1947.

[15] RT Tung. Schottky barrier height—do we really understand what we measure? *Journal of Vacuum Science & Technology B: Microelectronics and Nanometer Structures Processing, Measurement, and Phenomena*, 11(4): 1546–1552, 1993.

[16] Dieter K Schroder and Daniel L Meier. Solar cell contact resistance—a review. *IEEE Transactions on electron devices*, 31(5):637–647, 1984.

[17] AM Cowley and SM Sze. Surface states and barrier height of metal-semiconductor systems. *Journal of Applied Physics*, 36(10):3212–3220, 1965.

[18] K Varahramyan and EJ Verret. A model for specific contact resistance applicable for titanium silicide-silicon contacts. *Solid-State Electronics*, 39(11):1601–1607, 1996.

[19] Dieter K Schroder. *Semiconductor material and device characterization*. John Wiley & Sons, 2006.

[20] RT Tung. The physics and chemistry of the schottky barrier height. *Applied Physics Reviews*, 1(1):011304, 2014.

[21] AYC Yu. Electron tunneling and contact resistance of metal-silicon contact barriers. *Solid-State Electronics*, 13(2):239–247, 1970.

[22] Gunnar Schubert. *Thick film metallisation of crystalline silicon solar cells: Mechanisms, models and applications*. PhD thesis, Universität Konstanz.

[23] Gunnar Schubert, Frank Huster, and Peter Fath. Physical understanding of printed thick-film front contacts of crystalline si solar cells—review of existing models and recent developments. *Solar energy materials and solar cells*, 90(18):3399–3406, 2006.

[24] C Ballif, DM Huljić, G Willeke, and A Hessler-Wyser. Silver thick-film contacts on highly doped n-type silicon emitters: structural and electronic properties of the interface. *Applied physics letters*, 82(12): 1878–1880, 2003.

[25] ZG Li, L Liang, and LK Cheng. Electron microscopy study of front-side ag contact in crystalline si solar cells. 105.

[26] Praveen Kumar, Michael Pfeffer, Benjamin Willsch, and Oliver Eibl. Contact formation of front side metallization in p-type, single crystalline si solar cells: Microstructure, temperature dependent series resistance and percolation model. *Solar Energy Materials and Solar Cells*, 145:358–367, 2016.

[27] Michael Pfeffer, Praveen Kumar, and Oliver Eibl. High-efficiency crystalline-si solar cells with screen-printed front-side metallization: A percolation model to explain the current path. *Journal of Electronic Materials*, 45(11):5764–5772, 2016.

[28] Peter J Goodhew, John Humphreys, and Richard Beanland. *Electron microscopy and analysis*. CRC Press, 2000.

[29] Ludwig Reimer. *Scanning electron microscopy: physics of image formation and microanalysis*. IOP Publishing, 2000.

[30] Balaji I Birajdar. *Correlation of superconducting properties and microstructure in MgB 2 using SEM, EPMA and TEM*. PhD thesis, University of Tuebingen, 2008.

[31] Nicola Peranio. *Structural, chemical, and thermoelectric properties of Bi2Te3 Peltier materials: bulk, thin films, and superlattices*. PhD thesis, University of Tuebingen, 2008.

[32] Zainul Aabdin. *Structural characterization and structure-property correlation of nanostructured superconducting coated conductors and thermoelectric materials*. PhD thesis, University of Tuebingen, 2013.

[33] Transmission Electron Microscope - LEO 912 Omega manual. URL `https://mywebspace.wisc.edu/jatikals/web/MSColdwebsite/manuals/LEO912/english/complete/MAN912E.PDF`.

[34] G. Benner and W. Probst. Köhler illumination in the TEM: fundamentals and advantages. *Journal of Microscopy*, 174(3):133–142, 1994.

[35] Wolfgang Probst, Gerd Benner, Johannes Bihr, and Eugen Weimer. An "omega" energy filtering tem—principles and applications. *Advanced Materials*, 5(4):297–300, 1993.

[36] N Peranio and O Eibl. Quantitative edx microanalysis of bi2te3 in the tem. *physica status solidi (a)*, 204 (10):3243–3255, 2007.

[37] iTEM manual. URL `http://www.soft-imaging.net/en/eu/eng/2343_5832.htm`.

[38] INCA manual. URL `http://www.cnst.nist.gov/nanofab/pdf/INCA_Manual.pdf`.

[39] Werner Grogger, Maria Varela, Roger Ristau, Bernhard Schaffer, Ferdinand Hofer, and Kannan M Krishnan. Energy-filtering transmission electron microscopy on the nanometer length scale. *Journal of electron spectroscopy and related phenomena*, 143(2):139–147, 2005.

[40] JM Zuo, J Pacaud, R Hoier, and JCH Spence. Experimental measurement of electron diffuse scattering in magnetite using energy-filter and imaging plates. *Micron*, 31(5):527–532, 2000.

[41] R. F. Egerton. *Electron Energy-Loss Spectroscopy in the Electron Microscope*. Springer, 1996. ISBN 9780306452239.

[42] DB Williams and CB Carter. Transmission electron microscopy: a textbook for materials science, 2009.

[43] SS Ruvimov and K Scheerschmidt. Burgers vector determination in tem by using the dislocation parity analysis. *physica status solidi (a)*, 141(2):269–284, 1994.

[44] R. F. Egerton. Electron energy-loss spectroscopy in the TEM. *Reports on Progress in Physics*, 72(1):016502, January 2009.

[45] TM Chou and M Libera. Mean free paths for inelastic electron scattering in silicon and poly (styrene) nanospheres. *Ultramicroscopy*, 94(1):31–35, 2003.

[46] Rolf Erni. *Aberration-corrected imaging in transmission electron microscopy: An introduction*. World Scientific, 2010.

[47] David A Muller. Structure and bonding at the atomic scale by scanning transmission electron microscopy. *Nature materials*, 8(4):263–270, 2009.

[48] BD Forbes, AJ D'Alfonso, REA Williams, R Srinivasan, HL Fraser, DW McComb, B Freitag, DO Klenov, and LJ Allen. Contribution of thermally scattered electrons to atomic resolution elemental maps. *Physical Review B*, 86(2):024108, 2012.

[49] OL Krivanek, TC Lovejoy, and N Dellby. Aberration-corrected stem for atomic-resolution imaging and analysis. *Journal of microscopy*, 259(3):165–172, 2015.

[50] PE Batson, Niklas Dellby, and OL Krivanek. Sub-ångstrom resolution using aberration corrected electron optics. *Nature*, 418(6898):617–620, 2002.

[51] PE Batson. Simultaneous stem imaging and electron energy-loss spectroscopy with atomic-column sensitivity. *Nature*, 366(6457):727–728, 1993.

[52] PM Voyles, DA Muller, JL Grazul, PH Citrin, and H-JL Gossmann. Atomic-scale imaging of individual dopant atoms and clusters in highly n-type bulk si. *Nature*, 416(6883):826–829, 2002.

[53] AJ d'Alfonso, B Freitag, D Klenov, and LJ Allen. Atomic-resolution chemical mapping using energy-dispersive x-ray spectroscopy. *Physical Review B*, 81(10):100101, 2010.

[54] SJ Pennycook and LA Boatner. Chemically sensitive structure-imaging with a scanning transmission electron microscope. *Nature*, 336(6199):565–567, 1988.

[55] Victor D Scott and Glyn Love. *Quantitative electron-probe microanalysis*. E. Horwood. Halsted Press, 1983.

[56] David B Williams, C Barry Carter, and P Veyssiere. *Transmission electron microscopy: a textbook for materials science*, volume 10. Springer, 1998.

[57] Praveen Kumar, Michael Pfeffer, Nicola Peranio, Oliver Eibl, Svenja Bäßler, Heiko Reith, and Kornelius Nielsch. Ternary, single-crystalline bi 2 (te, se) 3 nanowires grown by electrodeposition. *Acta Materialia*, 125:238–245, 2017.

[58] Praveen Kumar, Michael Pfeffer, Eberhard Schweda, Oliver Eibl, Jijun Qiu, and Zhisheng Shi. Pbse mid-ir photoconductive thin films (part i): Phase analysis of the functional layer. *Journal of Alloys and Compounds*, 724:316–326, 2017.

[59] Rene Hoenig, Michael Duerrschnabel, Willem van Mierlo, Zainul Aabdin, Joerg Bernhard, Johannes Biskupek, Oliver Eibl, Ute Kaiser, Juergen Wilde, Florian Clement, et al. The nature of screen printed front side silver contacts-results of the project mikrosol. *Energy Procedia*, 43:27–36, 2013.

[60] P Kumar, B Willsch, M Dürrschnabel, Z Aabdin, R Hoenig, N Peranio, F Clement, D Biro, and O Eibl. Combined microstructural and electrical characterization of metallization layers in industrial solar cells. *Energy Procedia*, 67:31–42, 2015.

[61] Benjamin Willsch. The investigation of the series and contact resistance of industrial silicon solar cells in the temperature range of 80 k to 300 k, 2015.

[62] B Willsch, P Kumar, Z Aabdin, N Peranio, and O Eibl. Series and contact resistance measurements between 80k and room temperature for industrial solar cells. *Energy Procedia*, 67:49–63, 2015.

[63] Benjamin Willsch, Praveen Kumar, and Oliver Eibl. Front side metallization of n-and p-type, high-efficiency, single-crystalline si solar cells: Assessing the temperature-dependent series resistance. *Journal of Electronic Materials*, 45(6), 2016.

[64] Matthias Hörteis, Tobias Gutberlet, Armin Reller, and Stefan W Glunz. High-temperature contact formation on n-type silicon: basic reactions and contact model for seed-layer contacts. *Advanced functional materials*, 20(3):476–484, 2010.

[65] Ansgar Mette et al. *New concepts for front side metallization of industrial silicon solar cells*. PhD thesis, Fraunhofer-Institut für Solare Energiesysteme Freiburg, 2007.

[66] Raymond T Tung. Recent advances in schottky barrier concepts. *Materials Science and Engineering: R: Reports*, 35(1):1–138, 2001.

[67] Stefan Kontermann, Gerhard Willeke, and Jan Bauer. Electronic properties of nanoscale silver crystals at the interface of silver thick film contacts on n-type silicon. *Applied Physics Letters*, 97(19):191910, 2010.

[68] D Pysch, A Mette, A Filipovic, and SW Glunz. Comprehensive analysis of advanced solar cell contacts consisting of printed fine-line seed layers thickened by silver plating. *Progress in Photovoltaics: Research and Applications*, 17(2):101–114, 2009.

[69] C Khadilkar, S Sridharan, Dave Gnizak, T Pham, S Kim, and A Shaikh. Effect of glass chemistry and silicon orientation on the front contact microstructure formation in a silicon solar cell. *Proc. 20th EC PVSEC*, 2005.

[70] ZG Li, L Liang, AS Ionkin, BM Fish, ME Lewittes, LK Cheng, and KR Mikeska. Microstructural comparison of silicon solar cells' front-side ag contact and the evolution of current conduction mechanisms. *Journal of applied Physics*, 110(7):074304, 2011.

[71] Ching-Hsi Lin, Song-Yeu Tsai, Shih-Peng Hsu, and Ming-Hsun Hsieh. Investigation of ag-bulk/glassy-phase/si heterostructures of printed ag contacts on crystalline si solar cells. *Solar Energy Materials and Solar Cells*, 92(9):1011–1015, 2008.

[72] Stefan Kontermann, Alexander Ruf, Ralf Preu, and Gerhard Willeke. Simulating the interface morphology of silver thick film contacts on n-type si-(100) and si-(111). *Applied Physics Letters*, 101(12):121907, 2012.

[73] Enrique Cabrera, Sara Olibet, Joachim Glatz-Reichenbach, Radovan Kopecek, Daniel Reinke, and Gunnar Schubert. Experimental evidence of direct contact formation for the current transport in silver thick film metallized silicon emitters. *Journal of Applied Physics*, 110(11):114511, 2011.

[74] Hayoung Park, Joon Sung Lee, Soonwoo Kwon, Sewang Yoon, and Donghwan Kim. Effect of surface morphology on screen printed solar cells. *Current Applied Physics*, 10(1):113–118, 2010.

[75] Brad M Boyerinas, Joshua M Balsam, Hugh A Bruck, and Alexander L Roytburd. Effect of oxygen environment on formation of modulated ag nanostructures along the interface of a ag-si heterostructure. *Journal of Applied Physics*, 113(18):184302, 2013.

[76] Kyoung-Kook Hong, Sung-Bin Cho, Jae Sung You, Ji-Weon Jeong, Seung-Mook Bea, and Joo-Youl Huh. Mechanism for the formation of ag crystallites in the ag thick-film contacts of crystalline si solar cells. *Solar Energy Materials and Solar Cells*, 93(6):898–904, 2009.

[77] Sung-Bin Cho, Hee-Soo Kim, and Joo-Youl Huh. Mechanism underlying the beneficial effect of forming gas annealing on screen-printed ag contacts of crystalline si solar cells. *Acta Materialia*, 70:1–7, 2014.

[78] Mohamed M Hilali, Srinivasan Sridharan, Chandra Khadilkar, Aziz Shaikh, Ajeet Rohatgi, and Steve Kim. Effect of glass frit chemistry on the physical and electrical properties of thick-film ag contacts for silicon solar cells. *Journal of electronic materials*, 35(11):2041–2047, 2006.

[79] Mohamed M Hilali, Ajeet Rohatgi, and Sally Asher. Development of screen-printed silicon solar cells with high fill factors on 100/spl omega//sq emitters. *IEEE transactions on electron devices*, 51(6):948–955, 2004.

[80] Mohamed M Hilali, Mowafak M Al-Jassim, Bobby To, Helio Moutinho, Ajeet Rohatgi, and Sally Asher. Understanding the formation and temperature dependence of thick-film ag contacts on high-sheet-resistance si emitters for solar cells. *Journal of the Electrochemical Society*, 152(10):G742–G749, 2005.

[81] Gary C Cheek, ROBERT P Mertens, ROGER Van Overstraeten, and LOUIS Frisson. Thick-film metallization for solar cell applications. *IEEE Transactions on Electron Devices*, 31(5):602–609, 1984.

[82] R Hoenig, A Kalio, J Sigwarth, F Clement, M Glatthaar, J Wilde, and D Biro. Impact of screen printing silver paste components on the space charge region recombination losses of industrial silicon solar cells. *Solar Energy Materials and Solar Cells*, 106:7–10, 2012.

[83] Stefan Kontermann, Ralf Preu, and Gerhard Willeke. Calculating the specific contact resistance from the nanostructure at the interface of silver thick film contacts on n-type silicon. *Applied Physics Letters*, 99 (11):111905, 2011.

[84] Abasifreke Ebong, Dana Hankey, and Le Yang. Developing the next generation low-cost inks for high efficiency multi crystalline silicon solar cells. In *High Capacity Optical Networks and Enabling Technologies (HONET-CNS), 2013 10th International Conference on*, pages 66–71. IEEE, 2013.

[85] Praveen Kumar, Michael Pfeffer, Benjamin Willsch, Oliver Eibl, Lejo J Koduvelikulathu, Valentin D Mihailetchi, and Radovan Kopecek. N-type single-crystalline si solar cells: Front side metallization for solar cells reaching 20% efficiency. *Solar Energy Materials and Solar Cells*, 157:200–208, 2016.

[86] JE Cotter, JH Guo, PJ Cousins, MD Abbott, FW Chen, and KC Fisher. P-type versus n-type silicon wafers: prospects for high-efficiency commercial silicon solar cells. *IEEE Transactions on Electron Devices*, 53(8): 1893–1901, 2006.

[87] Daniel Macdonald and LJ Geerligs. Recombination activity of interstitial iron and other transition metal point defects in p-and n-type crystalline silicon. *Applied Physics Letters*, 85(18):4061–4063, 2004.

[88] A ur Rehman and Soo Hong Lee. Advancements in n-type base crystalline silicon solar cells and their emergence in the photovoltaic industry. *The Scientific World Journal*, 2013, 2013.

[89] R Kopecek, T Buck, J Libal, R Petres, I Röver, K Wambach, R Kinderman, LJ Geerligs, and P Fath. Large area n-type multicrystalline silicon solar cells with b-emitter: efficiencies exceeding 14%. *Proc. 15th IPSEC, Shanghai*, pages 883–4, 2005.

[90] R Lago, L Pérez, H Kerp, I Freire, I Hoces, N Azkona, F Recart, and JC Jimeno. Screen printing metallization of boron emitters. *Progress in Photovoltaics: Research and Applications*, 18(1):20–27, 2010.

[91] Susanne Fritz, Markus König, Stefanie Riegel, Axel Herguth, Matthias Hörteis, and Giso Hahn. Formation of ag/al screen-printing contacts on b emitters. *IEEE Journal of Photovoltaics*, 5(1):145–151, 2015.

[92] Susanne Fritz, Stefanie Riegel, Sebastian Gloger, Dietmar Kohler, Markus König, Matthias Hörtheis, and Giso Hahn. Influence of emitter properties on contact formation to p+ silicon. *Energy Procedia*, 38:720–724, 2013.

[93] Friedemann D Heinz, Matthias Breitwieser, Paul Gundel, Markus König, Matthias Hörteis, Wilhelm Warta, and Martin C Schubert. Microscopic origin of the aluminium assisted spiking effects in n-type silicon solar cells. *Solar Energy Materials and Solar Cells*, 131:105–109, 2014.

[94] Alexander Edler, Valentin Mihailetchi, Radovan Kopecek, Rudolf Harney, Tim Böscke, Daniel Stichtenoth, Jan Lossen, Karsten Meyer, Ronald Hellriegel, Tilo Aichele, et al. Improving screen printed metallization for large area industrial solar cells based on n-type material. *Energy Procedia*, 8:493–497, 2011.

[95] Stefanie Riegel, Florian Mutter, Thomas Lauermann, Barbara Terheiden, and Giso Hahn. Review on screen printed metallization on p-type silicon. *Energy Procedia*, 21:14–23, 2012.

[96] Elmar Lohmüller, Sabrina Werner, Rene Hoenig, Johannes Greulich, and Florian Clement. Impact of boron doping profiles on the specific contact resistance of screen printed ag–al contacts on silicon. *Solar Energy Materials and Solar Cells*, 142:2–11, 2015.

[97] Alexander Edler, Valentin D Mihailetchi, Lejo J Koduvelikulathu, Corrado Comparotto, Radovan Kopecek, and Rudolf Harney. Metallization–induced recombination losses of bifacial silicon solar cells. *Progress in Photovoltaics: Research and Applications*, 23(5):620–627, 2015.

[98] Valentin D Mihailetchi, Johann Jourdan, Alexander Edler, Radovan Kopecek, Rudolf Harney, Daniel Stichtenoth, Jan Lossen, Tim S Böscke, and Hans-Joachim Krokoszinski. Screen printed n-type silicon solar cells for industrial application. In *Proceedings of the 25th European Photovoltaic Solar Energy Conference and Exhibition*, pages 6–10, 2010.

[99] Helge Hannebauer, Thorsten Dullweber, Tom Falcon, and Rolf Brendel. Fineline printing options for high efficiencies and low ag paste consumption. *Energy Procedia*, 38:725–731, 2013.

[100] Josh Engelhardt, Alexander Frey, Susanne Fritz, Gabriel Micard, Stefanie Riegel, Giso Hahn, and Barbara Terheiden. Contact formation on boron doped silicon substrates from passivating pecv-deposited dielectric doping layers with anti-reflective properties by screen-printing ag pastes for high-efficiency n-type silicon solar cells. In *31st European Photovoltaic Solar Energy Conference and Exhibition*, pages 351–354, 2015.

[101] Susanne Fritz, Josh Engelhardt, Stefanie Ebert, and Giso Hahn. Contacting boron emitters on n-type silicon solar cells with aluminium-free silver screen-printing pastes. *physica status solidi (RRL)-Rapid Research Letters*, 10(4):305–309, 2016.

[102] AG Aberle, SR Wenham, and MA Green. A new method for accurate measurements of the lumped series resistance of solar cells. In *Photovoltaic Specialists Conference, 1993., Conference Record of the Twenty Third IEEE*, pages 133–139. IEEE, 1993.

[103] Ernest Bassous. Fabrication of novel three-dimensional microstructures by the anisotropic etching of (100) and (110) silicon. *IEEE Trans. Electron Devices*, 25(10):1178–1185, 1978.

[104] F Scott Johnson, Donald S Miles, Douglas T Grider, and JJ Wortman. Selective chemical etching of polycrystalline sige alloys with respect to si and sio2. *Journal of Electronic Materials*, 21(8):805–810, 1992.

[105] Zhipeng Huang, Nadine Geyer, Peter Werner, Johannes De Boor, and Ulrich Gösele. Metal-assisted chemical etching of silicon: a review. *Advanced materials*, 23(2):285–308, 2011.

[106] Shahram Seyedmohammadi, Ed Graddy, and Aziz Shaikh. Screen printable ag-al metal pastes for p+ silicon application in solar cells. In *Photovoltaic Specialists Conference (PVSC), 2010 35th IEEE*, pages 003600–003603. IEEE, 2010.

[107] Harald Kerp, Steve Kim, Rosa Lago, Frederico Recart, Iratxe Freire, Lourdes Pérez, Knuth Albertsen, Juan Carlos Jiméno, and Aziz Shaikh. Development of screen printable contacts for p+ emitters in bifacial solar cells. In *Proc. 21st Eur. Photovoltaic Sol. Energy Conf*, pages 892–894, 2006.

[108] Liang Liang, Zhigang Li, Lap Kin Cheng, Norihiko Takeda, RJS Young, and Alan Carroll. Current conduction mechanism of front-side contact of n-type crystalline si solar cells with ag/al pastes. *IEEE Journal of Photovoltaics*, 4(2):549–553, 2014.

[109] L Liang, ZG Li, LK Cheng, N Takeda, and AF Carroll. Microstructural characterization and current conduction mechanisms of front-side contact of n-type crystalline si solar cells with ag/al pastes. *Journal of Applied Physics*, 117(21):215102, 2015.

[110] Praveen Kumar, Zainul Aabdin, Michael Pfeffer, and Oliver Eibl. High-efficiency, single-crystalline, p- and n-type si solar cells: Microstructure and chemical analysis of the glass layer. *Solar Energy Materials and Solar Cells*, accepted, 2018. doi: 10.1016/j.solmat.2018.01.001.

[111] Hee-Soo Kim, Sung-Bin Cho, Heesan Kim, Donghwan Kim, Miki Dovrat, Guy Eytan, and Joo-Youl Huh. Electrochemical nature of contact firing reactions for screen-printed silicon solar cells: origin of "gray finger" phenomenon. *Progress in Photovoltaics: Research and Applications*, 24(9):1237–1250, 2016.

[112] T Nakajima, A Kawakami, and A Tada. Ohmic contact of conductive silver paste to silicon solar cells. *The International journal for hybrid microelectronics*, 6:580–8, 1983.

[113] PDC King and Tim D Veal. Conductivity in transparent oxide semiconductors. *Journal of Physics: Condensed Matter*, 23(33):334214, 2011.

[114] Yaping Zhang, Yunxia Yang, Jianhua Zheng, Guorong Chen, Chen Cheng, James CM Hwang, Boon S Ooi, Andriy Kovalskiy, and Himanshu Jain. Effect of the interface glass on electrical performance of screen printed ag thick-film contacts of si solar cells. *Thin Solid Films*, 518(24):e111–e113, 2010.

[115] Alex S Ionkin, Brian M Fish, Zhigang Rick Li, Mark Lewittes, Paul D Soper, John G Pepin, and Alan F Carroll. Screen-printable silver pastes with metallic nano-zinc and nano-zinc alloys for crystalline silicon photovoltaic cells. *ACS applied materials & interfaces*, 3(2):606–611, 2011.

[116] Alan Frederick Carroll and Kenneth Warren Hang. Conductive compositions and processes for use in the manufacture of semiconductor devices, October 14 2008. US Patent 7,435,361.

[117] Praveen Kumar, Michael Pfeffer, Benjamin Willsch, Oliver Eibl, Lluís Yedra, Santhana Eswara, Jean-Nicolas Audinot, and Tom Wirtz. Direct imaging of dopant distributions across the si-metallization interfaces in solar cells: Correlative nano-analytics by electron microscopy and nanosims. *Solar Energy Materials and Solar Cells*, 160:398–409, 2017.

[118] AA Istratov, H Hieslmair, and ER Weber. Iron contamination in silicon technology. *Applied Physics A*, 70 (5):489–534, 2000.

[119] Jörg Palm, Volker Probst, and Franz H Karg. Second generation cis solar modules. *Solar Energy*, 77(6): 757–765, 2004.

[120] V Probst, W Stetter, W Riedl, H Vogt, M Wendl, H Calwer, S Zweigart, K-D Ufert, B Freienstein, H Cerva, et al. Rapid cis-process for high efficiency pv-modules: development towards large area processing. *Thin Solid Films*, 387(1):262–267, 2001.

[121] V Probst, F Karg, J Rimmasch, W Riedl, W Stetter, H Harms, and O Eibl. Advanced stacked elemental layer process for cu (inga) se 2 thin film photovoltaic devices. *MRS Online Proceedings Library Archive*, 426, 1996.

[122] L Sangely, B Boyer, E De Chambost, N Valle, JN Audinot, T Ireland, M Wiedenbeck, J Aléon, H Jungnickel, JP Barnes, et al. New developments in mass spectrometry. *Secondary ion mass spectrometry*, 3: 439–499, 2015.

[123] FA Stevie, CB Vartuli, LA Giannuzzi, TL Shofner, SR Brown, B Rossie, F Hillion, RH Mills, M Antonell, RB Irwin, et al. Application of focused ion beam lift-out specimen preparation to tem, sem, stem, aes and sims analysis. *Surface and interface analysis*, 31(5):345–351, 2001.

[124] F Siegelin, A Dubotzky, B Danzfuss, and S Shomann. Dopant analysis on advanced cmos technologies. In *Proceedings from the 34th International Symposium for testing and failure analysis*, 2008.

[125] Carsten W Mueller, Peter K Weber, Matt R Kilburn, Carmen Hoeschen, Markus Kleber, and Jennifer Pett-Ridge. Advances in the analysis of biogeochemical interfaces: Nanosims to investigate soil microenvironments. *Adv. Agron*, 121(1), 2013.

List of Tables

List of Figures

List of Acronyms and Symbols

SEM:	Scanning Electron Microscopy
TEM:	Transmission Electron Microscopy
XRD:	X-ray Diffraction
STEM:	Scanning Transmission Electron Microscopy
EF-TEM:	Energy-Filtered Transmission Electron Microscopy
SAED:	Selected Area Electron Diffraction
HRTEM:	High-Resolution Transmission Electron Microscopy
HRSEM:	High-Resolution Scanning Electron Microscopy
EELS:	Electron Energy Loss Spectroscopy
ESI:	Electron Spectroscopic Imaging
SE:	Scanning Electron
BSE:	Back-Scattered Electron
LM:	Light Microscopy
BF:	Bright-field
BF:	Dark-field
EDX:	Energy-Dispersive X-ray Microanalysis
PV:	Photovoltaic
PERT:	Passivated Emitter Rear Totally Diffused
TLM	Transmission Line Method
TE:	Thermionic Emission
FE:	Field Emission
TFE:	Thermionic Field Emission
SRH:	Schockley-Read Hall
SBH:	Schottky Barrier Height
FSP:	Front Side Paste
Si:	Silicon
c-Si:	Crystalline Silicon
FZ-Si:	Floatzone Silicon
Cz-Si:	Czochralski Silicon
BSF:	Back Surface Field
AM 1.5:	Air Mass 1.5
FGA	Forming Gas Annealing
a, b,c :	Lattice Parameters
d_{hkl} :	Inter-planar spacing for (h k l) planes
η :	Efficiency
FF:	Fill Factor
R_S:	Series Resistance

R_P:	Parallel Resistance
ρ_C:	Contact Resistance
N_D:	Concentration of donor atoms
J_{O1}:	Dark saturation current density of base and emitter
J_{O2}:	Dark saturation current density of the space charge region
n_1, n_2:	Ideality factor of the first and second diode
J_{SC}:	Short circuit current density
J_{ph}:	Photocurrent density
I_O:	Dark saturation current density
V_{OC}:	Open circuit voltage
φ_M:	Metal work function potential
φ_S:	Semiconductor work function potential
χ_S.	Electron affinity
φ_{Bn}:	Potential barrier between the metal and n-type semiconductor
SiN_x:	Passivation layer
K_B:	Boltzmann constant
q:	Elementary charge
h:	Plank constant

Acknowledgments

Eidesstattliche Versicherung

Ich erkläre hiermit, dass ich die zur Promotion eingereichte Arbeit mit dem Titel "**Structure-property Correlation of Front Side Metallization Contacts for High-efficiency, Single-crystalline Si Solar Cells**" selbständig verfasst, nur die angegebenen Quellen und Hilfsmittel benutzt und wörtlich oder inhaltlich ubernommene Stellen als solche gekennzeichnet habe. Ich versichere an Eides statt, dass diese Angaben wahr sind und dass ich nichts verschwiegen habe. Mir ist bekannt, dass die falsche Abgabe einer Versicherung an Eides statt mit Freiheitsstrafen bis zu drei Jahren oder mit Geldstrafe bestraft wird.

Weiterhin erkläre ich, dass bisher kein Promotionsversuch unternommen wurde.

Tübingen, den ＿＿＿＿＿＿＿ ＿＿＿＿＿＿＿＿＿＿＿＿＿＿

Declaration

I hereby declare that I have produced the work entitled "**Structure-property Correlation of Front Side Metallization Contacts for High-efficiency, Single-crystalline Si Solar Cells**", submitted for the award of a doctrate, on my own and without any external help. I have only used the sources and materials cited in the work, and that all citations, whether word for word or paraphrased are given as such. I declare that I followed the guidelines set by the University of Tübingen. I declare that these statements are true and that I am concealing nothing. I understand that any false statements can be punished with a jail term of up to three years or a financial penalty.

Tübingen _____ _____

Scientific contributions

Publications during Ph. D. thesis

Peer-reviewed journal papers

1. **P. Kumar**, M. Pfeffer, B. Willsch, O. Eibl, "Contact Formation of Front Side Metallization in p-type, Single Crystalline Si Solar Cells: microstructure, temperature dependent series resistance and percolation model," **Sol. Energy Mater. Sol. Cells**, 145, (2016) pp. 358–367. doi:10.1016/j.solmat.2015.10.042

2. **P. Kumar**, M. Pfeffer, B. Willsch, O. Eibl, V.D. Mihailetchi, L.J. Koduvelikulathu, R. Kopecek, "N-type single-crystalline Si solar cells: front side metallization for solar cells reaching 20 % efficiency," **Sol. Energy Mater. Sol. Cells**, 157, (2016) pp. 200–208. doi:10.1016/j.solmat.2016.05.027

3. **P. Kumar**, M. Pfeffer, B. Willsch, O. Eibl, L .Yedra, S. Eswara, J-. N. Audinot, T. Wirtz, "Direct imaging of dopant distributions across the Si-metallization interfaces in solar cells: Correlative nano-analytics by electron microscopy and NanoSIMS," **Sol. Energy Mater. Sol. Cells**, 160, (2017) pp. 398–409. doi:10.1016/j.solmat.2016.11.004

4. **P. Kumar**, M. Pfeffer, N. Peranio, O. Eibl, S. Bäßler, H. Reith, K. Nielsch, Ternary, single-crystalline Bi2 (Te, Se)3 nanowires grown by electrodeposition," **Acta Mater.**, 125, (2017) pp. 238–245. doi:10.1016/j.actamat.2016.11.057

5. G. Rogl, A. Grytsiv, P. Heinrich, E. Bauer, **P. Kumar**, N. Peranio, O. Eibl, J. Horky, M. Zehetbauer, P. Rogl, "New bulk p-type skutterudites $DD_{0.7}Fe_{2.7}Co_{1.3}Sb_{12-x}X_x$ (X = Ge, Sn) reaching ZT > 1.3," **Acta Mater.**, 91, (2015) pp. 227–238. doi:10.1016/j.actamat.2015.03.008

6. M. Pfeffer, **P. Kumar**, O. Eibl, "High efficiency, crystalline Si solar cells with screen printed front side metallization: a percolation model for explaining the current path," **J. Electron. Mater.**, 45, (2016), pp. 5764–5772. doi:10.1007/s11664-016-4818-5

7. B. Willsch, **P. Kumar**, O. Eibl, "Front side metallization of n- and p-type, high-efficiency, single-crystalline Si solar cells: assessing the temperature dependent series resistance," **J. Electron. Mater.**, 45, (2016) pp. 2656–2661. doi:10.1007/s11664-016-4459-8

8. **P. Kumar**, M. Pfeffer, E. Schweda, O. Eibl, J. Qiu, Z. Shi, "PbSe mid-IR photoconductive thin films (part-I): phase analysis of the functional layer," **J. Alloys and Compd.**, 724, (2017) pp. 316–326. doi:10.1016/j.jallcom.2017.06.330

9. **P. Kumar**, Z. Aabdin, M. Pfeffer, O. Eibl, "High-efficiency, single-crystalline, p- and n-type Si solar cells: microstructure and chemical analysis of the glass layer," **Sol. Energy Mater. Sol. Cells**, 178C, (2018) pp. 52–64. doi: 10.1016/j.solmat.2018.01.001.

10. **P. Kumar**, M. Pfeffer,C. Berthold, O. Eibl, "PbSe mid-IR photoconductive thin films (part-II): Structural analysis of the functional layer,"**J. Alloys and Compd.**, 725, (2018) pp. 1654–1661. doi:10.1016/j.jallcom.2017.11.252

Peer-reviewed conference papers

1. **P. Kumar**, B. Willsch, M. Dürrschnabel, Z. Aabdin, R. Hoenig, N. Peranio, F. Clement, D. Biro, O.Eibl, "Combined Microstructural and Electrical Characterization of Metallization Layers in Industrial Solar Cells," **Energy Procedia.**, 67, (2015) pp. 31–42. doi:10.1016/j.egypro.2015.03.285

2. B. Willsch, **P. Kumar**, Z. Aabdin, N. Peranio, O. Eibl, "Series and Contact Resistance Measurements between 80K and Room Temperature for Industrial Solar Cells," **Energy Procedia.**, 67 (2015) 49–63. doi:/10.1016/j.egypro.2015.03.287

3. **P. Kumar**, M. Pfeffer, O. Eibl, "Front side metallization of p- and n-type Si solar cells: microstructure of the glass layer," **EUPVSEC Proceedings**, September 2017 pp. 923–927. doi:/10.4229/EUPVSEC20172017-2CV.2.64

4. **P. Kumar**, M. Pfeffer, B. Willsch, O. Eibl, L .Yedra, S. Eswara, J-. N. Audinot, T. Wirtz, "Screen printed mono-crystalline Si solar cells: assessing the microstructure and dopant concentration at the front side metallization interface by electron microscopy and NanoSIMS," **EUPVSEC Proceedings**, September 2017 pp. 907–910. doi:/10.4229/EUPVSEC20172017-2CV.2.55

5. M. Pfeffer, **P. Kumar**, M. Zehender, B. Willsch O. Eibl, "Front side metallization of p and n-type Si solar cells: a percolation model for explaining the current path," **EUPVSEC Proceedings**, September 2017 pp. 247–250. doi:/10.4229/EUPVSEC20172017-2AO.4.4

Curriculum Vitae

Personal data

Name	Mr. Praveen Kumar
Date and place of birth	02, Feburary, 1987, Gouripur (Baghpat), U.P, (India)
Nationality	Indian
Email	praveen87.iitd@gmail.com

School

Higher primary schooling	
(1997-2002, CBSE board, Delhi)	D.A.V Public School Baghpat
Secondary schooling	
(2002-2004, U. P board, Allahabad)	D.A.V Inter College Tatiri, Baghpat

University

Bachelor of Science (B.Sc.)	
(2004-2008, PCM)	M. M. College Khekra (C. C. S. University Meerut, India)
Master of Science (M.Sc.)	
(2008-2010, Physics)	D. N. College Meerut (C. C. S. University Meerut, India)
Master of Technology (M.Tech.)	
(2011-2013, Solid state materials)	Indian Institute of Technology Delhi (IITD), India.

Doctor of Natural Sciences (Dr. rer. nat.)

Ph. D. thesis	
(November, 2013- March, 2018)	Institute of Applied Physics, University of Tübingen
Thesis supervisor	(Prof. Dr. Oliver Eibl)

Tübingen _____